Molecular Dynamics Simulations of Dry Sliding Asperities to Study Friction and Frictional Energy Dissipation

by

Bhavin Narottam Vadgama

A dissertation submitted to the Graduate Faculty of
Auburn University
in partial fulfillment of the
requirements for the Degree of
Doctor of Philosophy

Auburn, Alabama
May 04, 2014

Keywords: Sliding Friction, Nano-scale, Molecular Dynamics

Approved by

Daniel K. Harris, Chair, Associate Professor of Mechanical Engineering
Robert L. Jackson, Associate Professor of Mechanical Engineering
Virginia Davis, Associate Professor of Chemical Engineering
Amnon J. Meir, Professor of Mathematics

Abstract

Fundamental friction characteristics such as the friction coefficient, wear, adhesion, and dissipation of energy require an accurate understanding of how the surfaces in contact interact on nano or atomic scale. At nano scales since the ratio of surface area to volume is very high, quantum mechanics rather than classical laws for the bulk govern properties and process. Most of the known properties of materials are obtained from the bulk and hence cannot be used for analysis of nano components. Therefore, one of the biggest challenges in the miniaturization of systems is overcoming the tribological problems. With the rapid development in surface examining technologies like AFM, SFA and others as well as development of MEMS and NEMS devices, a better understanding of the atomistic mechanisms of sliding friction is essential in order to realize the true potential of such devices.

Friction between sliding surfaces is almost always associated with the release of thermal energy and the dissipation of this thermal energy is critical for friction since most of the surface phenomena depend on the temperature. The energy dissipation in MEMS/NEMS devices is complicated as it involves different mechanisms such as non-equilibrium phonon and electron-hole creation, bond breaking and electron emission, defect formation and structural transformation, and wear. Quantitative data for the energy dissipation channels like elastic and plastic deformation are crucial for understanding the mechanics of deformation.

Molecular modeling and simulation is a cost effective alternative to physical experiments for developing better insight on properties and phenomena at nano-scales. In

this work, molecular dynamics simulations are used to study friction and energy dissipation in dry sliding friction of two hemispherical copper asperities. LAMMPS, which is a classical molecular dynamics code developed by Sandia National Labs, is used to perform all the simulations. The effect of interference, relative sliding velocity, asperity size, lattice orientation, and temperature control on friction and energy dissipation is investigated. The atomistic mechanisms of friction are studied and a novel method of energy dissipation analysis is presented. The results are analyzed and compared to similar work in nano tribology whenever possible and the key developments are presented.

Acknowledgements

I would like to acknowledge the High Performance Computing Cluster administered through the Engineering Network Services at Auburn University for providing the computing power required to run most of the simulations for this research. I would like to specifically thank James Clark and Abdullah-Al-Owahid for set-up as well as troubleshooting of parallel processing.

I would like to thank Steve Plimpton of Sandia National Laboratories and Robert S. Hoy of the Department of Mechanical Engineering and Material Science at Yale University for their valuable suggestions on some details of the simulations.

Most importantly, I would like to thank my advisors, Dr. Daniel K. Harris and Dr. Robert L. Jackson for their valuable guidance and suggestions throughout this research. This work would not have been possible without their immense support, faith and availability for consultation.

Table of Contents

List of Tables

List of Figures

List of Symbols

A	- Constant
B	- Constant
E	- Total energy
E_k	- Kinetic energy
E_p	- Potential energy
$E_{p,therm}$	- Thermal potential energy
$E_{p,def}$	- Deformation potential energy
E_{bond}	- Energy due to bonded interaction
E_{angle}	- Energy due to bond angle
E_{coul}	- Energy due to coulombic interaction
E_{LJ}	- Energy due to Lennar-Jones potential
E_{tor}	- Energy due to torsion
F	- Force
F_n	- Average normal force
F_t	- Average tangential force
G	- Atom embedding energy
H	- Hamiltonian
N	- Number of atoms/particles
P	- Pressure
R	- Asperity radius
T	- Absolute temperature

V - Volume

W - Frictional work

X - Scale factor

Z - Partition function

a - Acceleration

b,b_0 - Bond length, equilibrium bond length

f_n - Normal force

f_t - Tangential/Friction force

k_B - Boltzmann constant

k_b, k_ϕ - Force constants for bond length and bond angle

m - Mass

p - Momentum

p^N - Momentum vectors of atoms

q - Charge

r - Position

r_c - Cut-off radius

r^N - Position vectors of atoms

r_{ij} - Distance between i^{th} and j^{th} atom/particle

t - Time

Δt - Time-step

u - Interaction potential function

v - Velocity

n - Periodicity of angle

β - Phase angle

δ - Interference between asperities

ϵ - Depth of interaction potential function

θ - Lattice orientation

κ - Dielectric constant

μ - Friction coefficient

μ_{eff} - Effective friction coefficient

ρ - Density

ρ_e - Electron density

σ - Distance between atoms at which interaction potential function is zero

τ - Torsional force constant

ϕ,ϕ_0 - Bond angle, equilibrium bond angle

ψ - Wave Function

Chapter 1

Introduction

1.1 Background

Tribology, the science of interacting surfaces in relative motion, is one of the oldest and undeniably a very important subject. It includes all the aspects of friction, adhesion, wear and lubrication [1]. The friction force resists the relative tangential motion of bodies in contact. This friction force is the key to some of the functions, which we take for granted for example walking or holding a cup of coffee or stopping a car. Several of our daily tasks would have been impossible to perform in the absence of friction. Adhesion is the tendency of two surfaces to stick to each other due to the surface energies of the individual surfaces and the van der Waals forces. Adhesion is responsible for the sticking of two flat glass surfaces with each other or the gecko on a wall. However, more often than not, friction or adhesion is not desirable. Work is needed to overcome frictional resistance or to separate adhered surfaces, which ultimately results in wear or waste heat.

Improving the tribological properties of the surface materials by researching better or novel materials, coatings or by employing effective lubrication could reduce the unwanted effects of friction. An estimated 6% of the GDP or more than 700 billion dollars worth of resources are spent in the USA to overcome friction and wear [2]. Even small improvements in the science or technology that reduces friction can have huge economic benefits. Understanding the physics of friction is therefore of fundamental importance. This is more so when tribological contacts have approached the atomic level. With the rapid development in surface examining technologies like Atomic Force Microscopy

(AFM), Surface Force Apparatus (SFA), and others as well as the development of Micro Electro-Mechanical System (MEMS) and Nano Electro-Mechanical System (NEMS) devices, a better understanding of the atomistic mechanisms of sliding friction is essential. The phenomena occurring at the nano-scale are complex and difficult to predict since the tribological properties of sliding contacts are greatly affected by the deformation of the contacts [3]. When surfaces in contact slide across each other only a small number of microscopic peaks or asperities truly come in contact. Therefore, the true area of contact is much smaller than the nominal contact area depending on the normal load and material properties. Continuum models provide a macroscopic understanding of the deformation of such contact asperities. However, at the nano or atomic scales the phenomena is dominated by surface mechanics. Below a certain scale the dependence of fundamental friction characteristics such as the friction coefficient, wear, adhesion, and dissipation of frictional heat upon factors such as inter-atomic forces, surface topography and the composition of materials increases [4] and therefore requires an accurate understanding of how the surfaces in contact interact on the nano or atomic scale.

1.2 Nano Tribology

One of the biggest challenges in the miniaturization of systems is overcoming the tribological problems. As the system components approach nano-scale, the ratio of the number of surface atoms to the bulk atoms becomes overwhelming. This results in an increase in the effect of the surface forces, which depend on the surface area, like friction and adhesion as opposed to the bulk forces. The components in MEMS or NEMS devices are built or assembled to very tight tolerances and the separation between the individual components is on the nano-scale. Any contact might trigger adhesion that can hinder the operation or even fail the device. Furthermore, most of the fabrication methods for such devices are planar, that is, the components are typically flat. Therefore, the sliding

interactions are mostly between sidewalls. This leads to a greater impact of the surface forces, which are generally neglected at the macro-scale [5].

MEMS/NEMS devices are fabricated to a high level of surface accuracy; yet, surface roughness is present at every scale. The surface roughness consists of peaks, or asperities, as referred to in tribology, and valleys of different heights. These asperities experience high molecular adhesive forces and contact pressures during sliding interactions, which result in extensive plastic deformation and/or wear [6]. For example, in a MEMS drive train the asperities on the sidewalls of the micro gears rub against each other causing wear and the resulting debris interfere in the rotation of the gears [5]. Since conventional lubricants are optimized for the micro- or macro-scale, they cannot be used effectively at the nano-scale and therefore, novel coatings are being developed that can reduce friction and resist wear [7]. A commercially successful and a widely known application of coatings that can reduce sliding friction at such a scale is the disk drive for data storage. The recording head slider flies over the magnetic disk's surface at high speeds (~10 m/s) with a required clearance in the nano-scale and any contact with the disk can be detrimental to the operation. Hard wear resistant coatings along with special solid lubricant has ensured the proper functioning of the disk drive and have led to a 10^5 time increase in the areal storage density [6].

Figure 1.1 shows a MEMS torque convertor consisting of multi-level rotating gears, which is driven by a micro-engine and is used to actuate an out-of-plane mirror. Here, premature failure was experienced as a result of fatigue from constant rubbing between the gear walls [8]. Besides friction and the resulting wear, adhesion is the other major tribological problem at micro- or nano-scale. Due to the increased surface energy at the nano-scale, the geometries that are in close proximity are greatly affected by surface forces such as electrostatic, chemical, capillary, and van der Waals [9]. During the fabrication of MEMS devices, adhesion is encountered when sacrificial layers are dissolved in a liquid etchant to obtain a freestanding beam or cantilever.

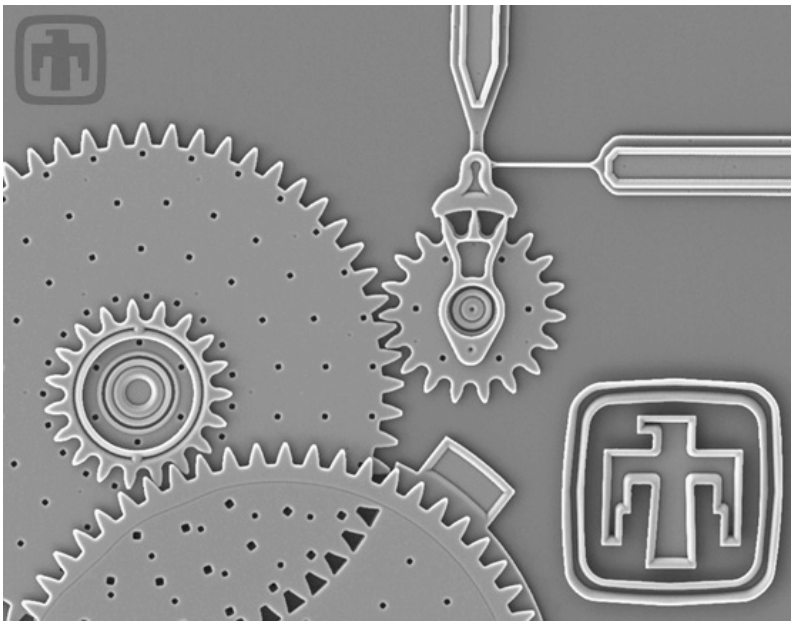

Figure 1.1: MEMS torque convertor with multi-level rotating gears [8]. Image courtesy of Sandia National Laboratories, SUMMiT(TM) Technologies, www.mems.sandia.gov

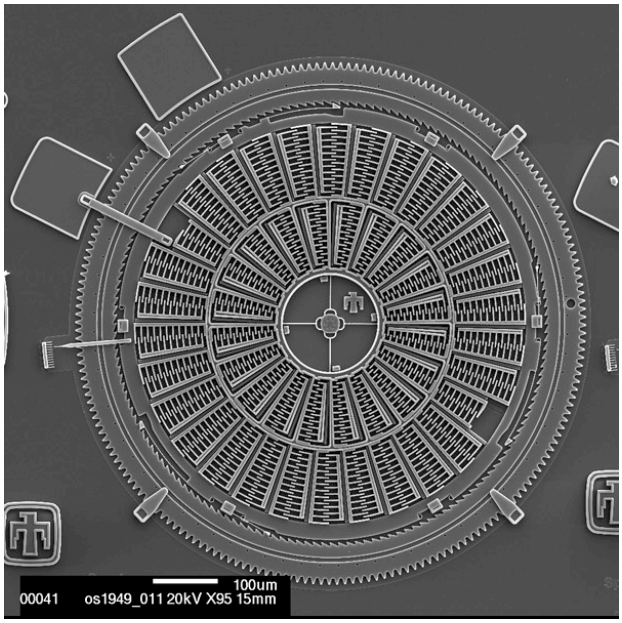

Figure 1.2: Torsional Ratcheting Actuator. Image courtesy of Sandia National Laboratories, SUMMiT(TM) Technologies, www.mems.sandia.gov

These beams adhere to the base due to the capillary forces of the etchant and remain adhered even after the etchant has dried if the beams do not generate enough restoring force. Some of the structures of devices like the accelerometer, or the torsional actuator (as show in Figure 1.2) have a thin cross section and can easily adhere to each other by cold junction formation due to high surface energy. This is also the case with the micro-gear torque converter mentioned above. Over time the sidewalls of the gears adhere together by chemical bonds preventing them to rotate when actuated [10].

MEMS/NEMS devices show promising capabilities in current and future technological advancement. However, some of these tribological challenges must be overcome to realize the true potential of such devices. Friction and adhesion at the nano-scale are different from the macro-scale due to the higher surface area to volume ratio that is believed to be the reason for the scale-effect in tribology. In order to design and fabricate better, long-lasting and efficient nano-scale devices, a better understanding of friction and adhesion is needed, specifically as to the origin of these phenomena at the atomic level. In addition to friction and adhesion, the energy dissipation in MEMS/NEMS devices is also complicated. It involves different mechanisms such as non-equilibrium phonon and electron-hole creation, bond breaking and electron emission, defect formation and structural transformation, and wear [11]. As friction increases, so does the local temperature, which in turn increases adhesion [12]. Quantitative data for the energy dissipation channels like elastic and plastic deformation are crucial for understanding the mechanics of deformation. Current availability of such information about the energy dissipation is limited and poses important challenges in ensuring both energy efficient fabrication or machining as well as functioning of MEMS/NEMS devices.

Computer simulation, specifically molecular dynamics (MD), has become quite popular among researchers with much work being done in micro and nano tribology. The study of sliding friction using MD can mainly be divided into three types based on the

geometries of the sliding surfaces: 1) flat surface against flat surface, 2) asperity against flat surface, and 3) asperity against asperity.

1.2.1 Flat Surface - Flat Surface Interaction

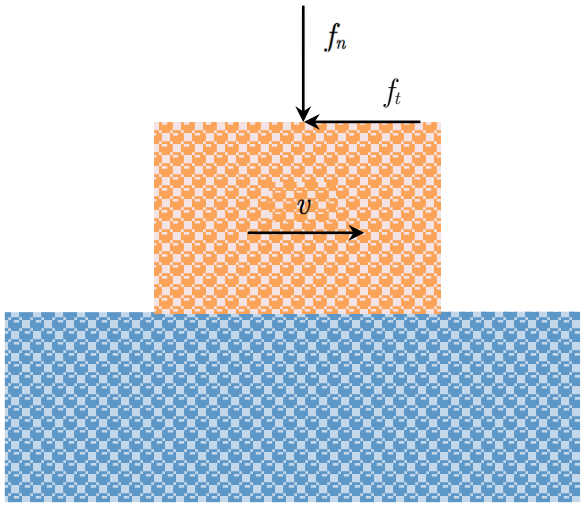

Figure 1.3: Flat surface – flat surface interaction

As shown in Figure 1.3, in this configuration two atomically flat surface slide across each other with a certain sliding velocity and under a given normal load. The surfaces start sliding and continuously remain in contact for the entire duration of the simulation. Harrison et al. [13] conducted MD simulations of (111) diamond surfaces, with and without chemisorbed alkyl groups, in sliding contact. They found that the friction coefficient increased with the normal load but this increment flattened out beyond a certain value of normal load. At this loading, the surfaces were too close to each other, which generated strong repulsive force thereby decreasing the friction force. Also, energy dissipation was mainly in the form of heat caused by vibrational excitation of the interface hydrogen atoms.

For a tribo-pair of Cu (001) and diamond (111) surfaces, Shen and Sun [14] studied the effect of hydrogenation on atomic scale friction. They studied various crystallographic

orientations for both H-free as well as hydrogenated diamond surface under various load values and found that the directional dependency of the friction disappears in the presence of hydrogen atoms. In addition, the sliding interaction in the presence of hydrogen atoms was wear-less only below a certain value of pressure. For the case of H-free diamond surface the sliding interaction was always wear-less irrespective of the pressure value.

Leonardo da Vinci first observed that friction was proportional to load and Guillaume Amontons rediscovered this in 1699 [6]. This basic equation of friction was reviewed by Landman et al. [15] with the help of MD. They suggested that local energy dissipation is mechanical as well as thermodynamic like irreversible compression-expansion cycles of molecule in between asperities. Hayashi et al. [16] showed that for an isolated mesoscopic system, the rate of energy dissipation in atomic scale wear-less sliding is equal to the frictional power, due to the anharmonicity of the potential function. This energy dissipation is through the thermal distribution of phonons and is dependent on the sliding velocity. Therefore, by controlling the sliding velocity and thereby the phonon density of states, the frictional characteristics of artificial materials for MEMS could be improved. The energy dissipation attributed to phonons in this case is due to the fact that here friction is purely interfacial and wear-less.

Li et al. [17] used the embedded atom method (EAM) potential to simulate Ni and Al for all possible slider-substrate tribo-system combinations using MD. They found that with one of the surfaces being pure Al, elastic (sound) waves, originated from the contact region, propagated the substrates and resulted in the oscillation of the potential energy. However, for all the simulation, they found that the plastic deformation, and not the phonons, was the major contributor to the energy dissipation mechanism during friction. Significant heat buildup was also seen at the interface when plastic deformation was high.

Jeng et al. [18] performed MD simulations on a (111) plane face-centered-cubic (fcc) lattice in hard-to-soft and soft-to-soft sliding systems simulating abrasive and non-abrasive sliding conditions. For both the sliding systems, they found that the friction force

under the repulsive force field was larger than that under the attractive force field. As a result, greater deformation and wear were seen under the repulsive force.

Kartikeyan et al. [19] studied the effect of sliding velocity and crystal orientation along with the presence of dislocations and interfaces in the MD simulations of the Fe-Cu tribo-pair. They found that Cu deformed plastically more than Fe, and the deformation increased with the sliding velocity as a result of temperature rise. Both the metal atoms mixed into each other even though their solubility is low under equilibrium conditions. Lin et al. [20] obtained similar results and observed that the friction force increased with and up to a sliding velocity of 300 m/s. Beyond this value of the sliding velocity, the friction force decreased since the increase in the interface temperature was sufficient to soften the material. Interfacial adhesion was responsible for plastic deformation as it causes lattice strains, which eventually lead to plasticity. The crystal lattice orientation affected the extent and mode of deformation and the presence of dislocations as well as internal interfaces made deformation easier. Yeo and Jang [21] have studied the effect of the sliding velocity on the change in the crystal structure of Al. They found that depending on the sliding velocity the fcc structure of Al goes from 100% fcc to amorphous to 25% fcc. This was found to greatly affect the friction characteristics for the corresponding values the sliding velocity.

Spijker et al. [22] numerically investigated the effects of surface roughness, lattice orientation, temperature, and adhesion on the friction characteristics of an Al-Al tribo-pair. They found that the surface roughness and the lattice orientation influence friction the most in cases with limited adhesion. They controlled the adhesion by altering the Lennard-Jones (LJ) potential used for their simulations. The surface roughness decreased with sliding and in the absence of which the lattice alignment was believed dictate friction. Also, when the adhesion was high, the temperature increase caused the friction to decrease perhaps suggesting the softening of the metal.

Simulating sliding systems with dimensions more than a few hundred nm would be extremely difficult since the computational time required is directly proportional to the number of atoms or particles in the system. In order to understand the scale effect of the frictional characteristics and to bridge the gap between atomistic and continuum models, Anciaux and Molinari [23] used a novel multi-scale coupling technique to simulate sliding contact between rough surfaces. They used the finite element method (FEM) to account for larger realistic sample sizes and a MD package for atomic scales. Their measurements of frictional forces showed differences between their models, but these differences reduced with increasing pressure suggesting the averaging effect of thermal softening. However, they found that the kinetic energy time evolution did not match within the models.

1.2.2 Asperity – Flat Surface Interaction

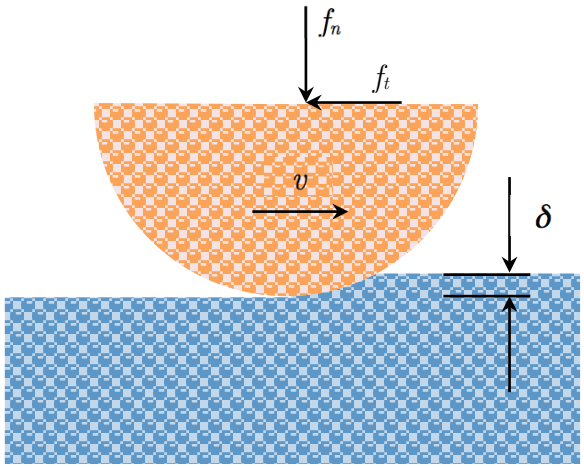

Figure 1.4: Asperity – flat surface interaction

In this configuration (Figure 1.4) an asperity slides over a flat surface with a certain sliding velocity and interference under a given normal load. The asperity could be of various sizes and shapes (spherical, hemi-spherical, prismatic, cylindrical, etc.). The

asperity generally starts sliding with the specified interference like the previous case and continuously remains in contact for the entire duration of the simulation.

Investigation of such a case of single asperity sliding over a flat surface using MD has been carried out by several research groups [4,24,25,26,27]. Zhang and Tanaka [28] did one of the earliest studies where they performed MD simulations of a diamond tip sliding over a flat copper surface. They found that four distinct deformation regimes existed and defined them as no-wear, adhering, ploughing and cutting of the surface. These were governed by indentation depth, sliding speed, asperity geometry and surface conditions. Interestingly, except in the cutting regime, the friction force did not follow the simple proportional friction law (i.e. Amonton's) observed at the macro-scale. Another important finding was that the no-wear regime was controllable which means wear-less frictional surfaces could be developed for suited applications. In a subsequent study of theirs [29] they performed simulations on a three-body contact sliding case consisting of a diamond tip sliding and rolling simultaneously on a flat Si surface to mimic foreign particles. A fifth condensing regime was reported in addition to the four mentioned above where the tip created a sliding mark on the surface without wear.

Around the same time, Sorensen et al. [30] performed a detailed study of the sliding interaction between a prismatic Cu tip on a Cu substrate. They studied the effects of load, contact area, sliding velocity, and lattice orientation combinations. Atomic-scale stick and slip was observed for all of the cases simulated but was lower for highly non-matching lattice configurations. This observation was extended to kinetic friction, which originated from the stick cycle.

In many cases, it is more important to understand what happens when two surfaces are brought in contact with each other which usually precedes the beginning of any sliding. This knowledge would be fundamental in understanding contact formation, contact resistance, material behavior, friction, and wear which usually appears after the surfaces come in contact [27]. Song et al. performed MD simulation of single asperity

contact and deformation on a flat surface over a complete loading and unloading cycle. Saw-tooth features were observed in the force-displacement relation in both the cycles. The dimensions of the asperity changed at every force drop, which resulted from plastic deformation during the loading cycle. During unloading, an extended elastic deformation is followed by plastic deformation, which coincided with maximum tensile force suggesting adhesion [27,31]. Additionally, stacking faults were created and destroyed which were different for both the cycles. In another work, [32] the authors simulated the same setup with repetitive loading and unloading cycles and observed that the initial fcc structure changed to hcp and back to fcc as a result of stacking fault accumulation.

The stick-slip phenomenon in the atomistic sliding of surfaces was investigated by Cho et al. [3] using MD simulation. A copper surface was scratched using a nickel tip at different indentation depths, speeds, and temperatures. According to the authors, the stick and slip occurs due to nucleation and propagation of dislocations respectively in the substrate. It was dependent on the depth of indentation and was strongly affected by the speed and temperature. In a similar study, Smith et al. [33] performed simulation of a pyramidal diamond tip ploughing through a crystalline Ag to investigate stick-slip and wear. They proposed that the dislocation propagates from the tip and intersects the surface in slip planes as the scratching takes place. In agreement to the findings of Cho et al. [3] the exact mechanism of stick-slip and friction were found to be highly dependent on the sliding depth, speed and temperature.

Yoon et al. [34] studied the effect of contact area on friction at nano and micro scales. They used glass balls of various radii on the top of an AFM tip to slide across a silicon wafer surface (uncoated and coated). They found the friction force to be directly proportional to normal load and the contact area. The coefficient of friction was smaller for case of a diamond-like-carbon (DLC) coated surface due to its lower adhesion owing to lower interfacial energy. At the nano scale, the friction is a strong function of the adhesive properties of the surfaces [34]. This adhesion, which arises from interfacial forces such as

capillary, electrostatic, and van der Waals forces [35], is of great concern in the development of MEMS and NEMS devices. Komanduri et al. [36] performed simulations of indentation and scratching on single-crystal aluminum in different orientations to study the anisotropy in hardness and the coefficient of friction. The anisotropy depended on the orientation, indentation direction, as well as on the plane of indentation. Their calculated hardness values were an order of magnitude higher than engineering values at the macroscopic level.

In order for MEMS or NEMS devices to function in accordance with their design, they have to be manufactured or machined to a great degree of accuracy. This means that the components they are made up of have to be even more geometrically and dimensionally precise and also possess low surface roughness. Prior understanding of the physics of nano machining would provide deeper insight on the overall manufacturing process reducing rejections and therefore costs. Ultra precision machining has been one the major areas of research interest in recent years [37,38,39,40,41,42,43]. Maekawa and Itoh [39] simulated the nano-scale machining of copper with a diamond-like tool with a 3 nm edge radius using MD. They observed a similarity of the chip formation as compared to macro machining. A growth in the chip thickness and cutting length lead to an increase in the average cutting forces as well as the system temperature.

Lin et al. [38] studied the nano scale grinding featuring energy dissipation, forces, stress states and grinding temperature. They found the grinding force to be fluctuating due to the generation of dislocation slip and plastic deformation, which is similar to the findings of other works mentioned earlier. Temperature of the crystal structure increased as a result of dislocation and increase of the kinetic energy of atoms. In an analysis of super high-speed nano grinding of aluminum [41] Shimizu et al. have shown that the work-affected layer as well as the plastic deformation of the surface is reduced when grinding speed is above the material static propagation speed of a plastic wave. Nano

machining and nano lithography using the AFM tool tip for cutting material has also drawn some attention [42,43].

Besides the analysis of simple friction systems, MD is being used in several novel areas of nano scale applications. A nano gear train used in MEMS was modeled using MD to analyze its meshing friction characteristics [44]. This study was based on modeling a pair of meshing nano-teeth. It was found that the frictional characteristics were similar but the frictional force was a steeper function of the contact area as compared to normal macro-gear meshing. This can be easily attributed to the nano scale effect with higher surface energies. In another work, C60 molecules deposited over a graphite surface to act as nano-bearings to reduce sliding friction were simulated to verify the rolling stick-slip phenomena proposed by other theoretical works [45].

Ciraci and Buldum [11] studied interaction energy and forces in the dry sliding of a single metal Ni asperity on an incommensurate substrate. They also presented a phononic model of energy dissipation from asperity to the substrate. In a similar work, a novel method of the calculation of heat dissipation during sliding between Ni and Al was presented using MD by [17]. They showed that the frictional heat and the temperature increase were due to plastic deformation near the contact. The stick-slip phenomenon in friction has been studied [33] to reveal that dislocations in fcc Ag can be linked to stick events with the emission in the substrate region near a pyramidal diamond tip which is pulled across the substrate surface. In another study [37] the wear of a diamond tool in nano-metric cutting of a single crystal silicon plate was modeled using MD and was demonstrated that thermo-chemical wear is the basic wear mechanism.

1.2.3 Asperity – Asperity Interaction

In this configuration (Figure 1.5) an asperity slides past another stationary asperity with a certain sliding velocity and interference under a given normal load, which

fluctuates as the sliding progresses. The asperity could be of various sizes and shapes (spherical, hemi-spherical, prismatic, cylindrical, etc.). The interaction generally starts once the asperities come in contact however, the contact terminates once the sliding asperity has passed the stationary asperity and comes out of contact with it (which can be extended due to adhesion. The frictional characteristics and the energy dissipation are measured over only this contact region.

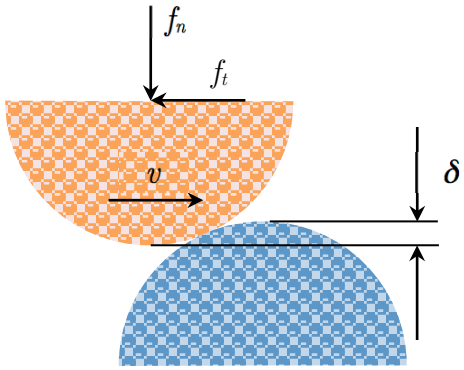

Figure 1.5: Asperity – asperity interaction

In one of the initial works on asperity-asperity interaction, Abraham et al. [46] studied the fragmentation dynamics in asperity collision using MD. The asperities were wedge shaped with a height and base equal to ~133A and the sliding velocity varied from 1/100 to 1/10 the speed of sound of the material. They used LJ and EAM potentials to simulate ductility and brittleness of the material. They found that the fragmentation of the asperities including lattice deformation, plastic flow and fracture were greatly influenced by the impact velocity during sliding.

As mentioned earlier, the scale effect in friction has been generally accepted which emphasizes that the mechanics governing friction at the macro-scale needs to be scaled up to be applied at the nano-scale. To verify this, Stone et al. [47] presented a comprehensive analysis of frictional effects on the inter-particle behavior of two spherical nickel

nanoparticles using MD. They performed simulations for uniaxial compression on single crystal nickel nanoparticles of varying size, interacting at various contact angles and crystal orientations to study the parametric effect on the deformation mechanism. They modified the Amontons–Coulomb friction law to include a length scale parameter to account for the effects of adhesion in nano-scale friction. Here, since the relative motion of the particles was uniaxial, friction was not present when the contact angle was 0°. For all other contact angles, the friction coefficient was measured to be significantly lower than the macro-scale values. Similarly, in order to study the effects that create nonconformities between atomistic behavior and continuum theory, Luan and Robbins [48] performed simulations of a rigid spherical tip contacting an elastic substrate. They quantified the effect of tip geometry on the contact mechanics for both non-adhesive and adhesive contacts. The deviation between atomistic behavior and continuum theory increased as the tip geometry changed from an idealized continuous spherical tip to an amorphous or stepped tip surface. However, other papers have shown that continuum mechanics can still on average effectively model nano-scale contacts.

Although not at the nano-scale, asperity – asperity interaction at micro-scale has been studied using FEM. Faulkner and Arnell [49] developed a new FEM model to simulate the sliding interaction between 3D elasto-plastic, hemispherical asperities of 10 μm in radius. They studied the effect of interference and adhesion on the frictional characteristics and find that the normal force remains relatively unchanged with adhesion, however the friction force was higher in the presence of adhesion. Also, the friction coefficient was lower for spherical asperities as opposed to cylindrical asperities. This has been attributed to the lateral flow of the displaced material around the sides of the spherical asperities. Dawkins and Neu [50] on the other hand, simulated the sliding of cylindrical asperities using FEM to investigate the effect of the lattice orientation. They used 5 mm radius single crystal Cu asperities to study energy dissipation and coefficient of friction.

Jackson et al. [51] performed a joint analysis using a semi-analytical model and FEM of sliding interaction between spherical asperities. They characterized the component of friction arising from the elasto-plastic deformation (without adhesive contribution) during sliding of asperities and found that the amount of energy lost between the asperities increased with the plastic deformation of the asperities. The plastic deformation increased with interference and normal load. In a similar study, Boucly et al. [52] modeled an elastic-plastic rolling/sliding contact between two spherical asperities. They found that due the plasticity of the asperities, the normal and tangential loads were asymmetric during the transient contact.

1.3 Motivation and Current Work

The main motivation for undertaking this friction study at the nano-scale is to better understand the governing mechanisms that generate and affect friction with the ultimate goal of being able to predict and therefore control friction in various tribological applications. Friction is a multi-scale phenomenon with different dominant mechanisms at every scale. As mentioned before, when two surfaces come into contact, it is only a few asperities from both surfaces that come in contact and start interacting. The atoms on these asperities are initially at equilibrium where the attractive and repulsive forces are balanced. Once they come into contact, these forces are no longer balanced and depending on the nature of their interaction, the atoms may or may not get displaced from their position before the interaction. If the atoms only move a distance, which is smaller than the bond length under the influence of attractive or repulsive forces during their interaction, then a restoring force will move them back to their original position. Otherwise, the atoms are displaced to new positions. This phenomenon is the basis of adhesion, plastic deformation, wear, as well as energy dissipation. It collectively generates

the normal and the tangential forces experienced during sliding interactions and therefore govern friction.

The major difference between friction mechanisms at the nano- and the macro-scales is that at the nano-scale surface forces dominate the interaction while at the macro-scale bulk forces dominate the interaction [53]. At the macro-scale, several asperity pairs of various sizes, shapes, and lattice orientations are interacting with each other simultaneously. The friction values are therefore, in a broad sense, a statistical average of all these interactions. A single asperity – asperity interaction can therefore be considered as the fundamental unit to study friction. Nonetheless, extending the results of a single asperity pair interaction to a macro surface might not be as straightforward. For example, the instantaneous forces on an individual asperity will be different from the average instantaneous forces on the entire sliding surface. Therefore, the instantaneous local tribological parameters may not average out over the entire surface. However (as proposed by Landman et al. [54]), when these parameters are time-averaged for a certain minimum number of individual asperities, they will be the same for all other groups with the same minimum number of asperities over the entire surface. Similarly, for a minimum number of such groups, their space-averaged instantaneous values will also be the same as those of the entire surface.

The biggest challenge here would be to determine these minimum values, above which the friction results of a single asperity pair interaction would converge to that of bulk material. In order to do so, the first step would be to understand the parameters such as the contact area (or indirectly the number of interacting atoms and therefore), asperity size, sliding velocity, sliding temperature, and lattice orientation on which the friction mechanisms depend in an asperity pair interaction. Additionally, the energy dissipation mechanism is also dependent on these interactions. Therefore, to get real insights into the atomistic origins of friction and frictional energy dissipation, it is important to study the interactions at the atomic or nano-scale. Although studies have

been done at the micro-scale, surprisingly, an asperity pair interaction has not been widely studied at the nano-scale in comparison to the other geometrical combinations discussed in the previous section. Unlike the other two combinations, an asperity – asperity interaction occurs over a short period of time and therefore the dynamics of the interaction are very different.

The current work is aimed at analyzing this configuration to better understand the frictional interaction as well as to identify and quantify the channels of energy dissipation. MD simulations of two, 3D, hemispherical asperities in sliding contact are performed. The effect of interference, asperity size, sliding velocity, lattice orientation, and temperature control on the interaction mechanisms, specifically friction, deformation, and energy dissipation are investigated. This would essentially provide a qualitative as well as quantitative understanding of the extent of influence each of these individual parameters have on the sliding interaction at the nano-scale and thus set the fundamental platform to be able to extend these results to macro-scale.

Chapter 2 discusses the role of molecular modeling in studying atomic-scale phenomena and describes various molecular modeling methods available. It explains the advantages and disadvantages of these methods and justifies the selection of Molecular Dynamics to study friction in the current work. The fundamental principle of MD is explained and the workings are explained in detail. The MD code used in the current work is discussed and the workings of the code are explained. The simulations performed to benchmark the code have been explained and the results are discussed.

Chapter 3 explains briefly the finite difference method used as well as the algorithm employed to integrate the equations of motions by the MD code. The importance of the time-step size for the simulations is explained and the selection criteria are described. The simulations performed to determine an appropriate time-step size are explained and the results are discussed. The equations used by the MD code to calculate various thermodynamic properties are listed.

Chapter 4 details the frictional analysis part of the study. The simulation model setup and parameters are listed and the simulation methodology is explained. The simulation results are discussed for frictional analysis. The mechanics of asperity-asperity interactions are analyzed and the effects of interference, asperity radius, sliding velocity, time-step size, lattice orientation, and temperature control on the frictional characteristics are discussed.

Chapter 5 details the energy analysis part of the study. The frictional work and the channels of energy dissipation are defined and discussed. The simulation parameters are listed and the simulation methodology is explained. The simulation results are discussed for energy dissipation analysis and the frictional work and the energy dissipation are quantified. The effects of interference, asperity radius, sliding velocity, time-step size, lattice orientation, and temperature control on the energy dissipation mechanism are discussed.

Chapter 6 contains the concluding remarks, the intellectual contribution, and the scope for future work is discussed.

Chapter 2

Molecular Modeling

2.1 Introduction

As technology advances, products and processes have been shrinking: from macro to micro and now to the nano scale as a result of continuous advancement in science and technology. Since the smallest building blocks of any material are atoms, the ultimate result of this miniaturization would be the ability to create or manufacture materials or products by assembling them atom by atom. With the advent of advanced micro-fabrication techniques such as oxidation and micro etching it is now possible to manufacture micro technological devices like MEMS. Such devices have transformed today's technology and have led to the development of systems such as accelerometers, pressure sensors, print heads, comb drives, relays, pumps, switches, etc. and have replaced conventional systems with bulky components. Similarly, at the nano scale, emerging processes like photolithography, self-assembly and other synthesis processes are making it possible to print nano silicon chips, create nano coatings, synthesize nano tubes etc. However, in order to produce such structures and devices with better control it is necessary to study phenomena and properties at the atomic or molecular levels.

Micro or nano devices are comprised of nano-scale components with at least one dimension less than 100 nm. Since, at these scales the ratio of surface area to volume is very high, quantum mechanics rather than classical laws for the bulk govern properties and mechanisms. Known electronic, optical, magnetic or mechanical properties of materials are obtained from the bulk and hence cannot be used for analysis of the nano

components – at least not in the conventional way. For example, macroscopic systems are well defined and are stable up to their melting point, however, at nano scales this is greatly influenced by the number of molecules/atoms as well as the shape of the device [55] since the surface forces become more important than the body forces at this scale. This greatly affects the phenomenon of adhesion. The energy levels are more similar to that found in individual atoms which affect the conductivity. Friction is more important at small scales because the adhesion is larger. The hardness and material strength at small scales are larger which actually reduces the real area of contact and reduces friction. Also, surfaces in MEMS and NEMS are often very clean which can result in very high adhesion and friction. Therefore it is important to study and understand these effects at nano scales.

2.2 Molecular Modeling and Simulation

The field of nano science and technology, or nano engineering as it is called, is still at an elementary stage and there is a lot more yet to be studied and researched. The better insight we develop on the properties and phenomena at nano scales, the better we will be able to synthesize, design or manufacture nano particles, structures or devices. Until then, it is needless to say that the cost associated with the actual building of such system, let alone experimenting with them, would be steep. Therefore, computational nano engineering or to be accurate, molecular modeling and simulation is an obvious choice for investigation, especially with the availability of today's computing resources.

"Molecular modeling is the science and art of studying molecular structure and function through model building and computation." [56]. In order to study a many-body system computationally, a suitable molecular model of the system is constructed and computer simulations are carried out using numerical solution techniques to calculate molecular trajectories [57]. These trajectories are then analyzed to determine the

properties of the system. The type of numerical solution technique used to determine these trajectories generally categorizes the methods of simulation, and the ones widely used are as follows:

2.2.1 Quantum Mechanical Methods

The basic ab initio or quantum mechanical (QM) methods solve the approximated or simplified Schrodinger's equation for a many-particle system where particles are treated as wave functions. The equations describe the spatial probability distributions corresponding to the energy states and are solved to obtain saddle points or minima on the potential energy surface.

The Schrodinger wave equation describing the motions of electrons and nuclei in a molecular system is

$$H\psi = E\psi \tag{2.1}$$

Here the Hamiltonian, H is the sum of the kinetic and potential energy of the system

$$H = E_k + E_p \tag{2.2}$$

and for a system of N particles of masses m_i in the absence of external potentials

$$H = \sum_{i=1}^{n} -\frac{h^2}{2m_i}\nabla_i^2 + \sum_{\substack{i,k=1 \\ i\neq k}}^{N} u_{ik}(r_i, r_k) \tag{2.3}$$

Here $u_{ik}(r_i, r_k)$ is the interaction potential originating from the electrostatic interactions among all the particles. For a 3D system the wave function ψ depends on the 3N coordinates of all the particles and therefore even for a relatively small number of particles, it is extremely difficult to solve the equations without simplifications or approximations.

Atomic and molecular systems consist of essentially electrons and nuclei where the latter differ greatly in their mass. This causes the electrons and the nuclei to have very different dynamics and therefore can be treated independently. The Born-Oppenheimer (BO) approximation is based on this: The electrons are considered as independent variables of H assuming fixed positions of the nuclei and this yields electronic energy levels of a molecule as a function of the positions of atoms. Then the quantum mechanical behavior of the nuclei is analyzed using ground state energy levels of the electrons [56]. This approximation simplifies the wave equation to a manageable form, yet an accurate analytic solution is not feasible except for very small systems and therefore must be solved using numerical methods.

Ab initio or non-empirical and semi-empirical methods based on BO approximations have been developed using different features which further reduce the high dimensionality of the Schrodinger equation. However, each of these methods has their own complexities, which have to be simplified or approximated to reduce the computational burden, and thus the quality of the results is greatly dependent on such approximations. Such methods explain all quantum effects on the basis of fundamental physical principles like electronic and nuclear structures and do not require any a priori knowledge of interacting potentials. The accuracy with which calculations match experimental data or a theoretical prediction is the biggest advantage offered by QM. The major drawback of such methods is that the time required for calculations increases exponentially with the number of atoms or particles. Also, these methods do not account for dynamics and hence properties like temperature cannot be determined [55].

2.2.2 Molecular Mechanics

Molecular Mechanics (MM) is based on classical mechanics where atoms in the molecules are treated as particles with mass, which interact in a force field. The force field

functionals are obtained from quantum mechanical calculations. The bonds between the atoms are treated as springs and spring deformation is used to characterize bond stretching, bending and torsion. To mimic non-bonded atoms van der Waals and electrostatic interactions are used. Again, the aim is to find saddle points or minima on the potential energy surface using an appropriate mathematical algorithm.

The potential energy is typically the sum of all the energies associated with bonded and non-bonded interactions as mentioned above. A typical functional form of the potential energy function is [56]

$$E = E_{bond} + E_{angle} + E_{tor} + E_{LJ} + E_{coul} \tag{2.4}$$

$$E_{bond} = \sum_{bonds} \frac{1}{2} k_b (b - b_0)^2 \tag{2.5}$$

$$E_{angle} = \sum_{angles} \frac{1}{2} k_\phi (\phi - \phi_0)^2 \tag{2.6}$$

$$E_{tor} = \sum_{tor} \frac{1}{2} \tau_n [1 \pm \cos(n\alpha - \beta)] \tag{2.7}$$

$$E_{LJ} = \sum_{ijpairs} \frac{A_{ij}}{r_{ij}^{12}} - \frac{B_{ij}}{r_{ij}^{6}} \tag{2.8}$$

$$E_{coul} = \frac{1}{4\pi\kappa_0\kappa} \sum_{ijpairs} \frac{q_i q_j}{r_{ij}} \tag{2.9}$$

Here n is the periodicity of the angle α.

Unlike ab initio methods, the computational time is much less and systems with a large number of particles can be solved. MM has been successfully applied to systems that

are close to equilibrium. Appropriate interaction potential have to be selected depending on the kind of bond and therefore, the success of molecular mechanics depends very much on the effective formulation of the potential energy function and the use of a suitable algorithm to find the minima.

2.2.3 Monte Carlo

Monte Carlo (MC) is a numerical technique developed to evaluate multidimensional integrals of statistical-mechanical ensemble averages or thermal averages. In particular, this technique is used to simulate systems with fixed N number of particles in a fixed volume V, at absolute temperature T. For such a system, the partition function is of the form

$$Z = \exp \int \left[-\frac{1}{k_B T} u(r^N) \right] dr^N \tag{2.10}$$

Then the thermal average of property A is given by

$$\langle A \rangle = \frac{1}{Z} \int \exp \left[-\frac{1}{k_B T} u(r^N) \right] A(r^N) dr^N \tag{2.11}$$

This integral cannot be solved analytically except in a few exceptional cases [58] and thus a numerical technique has to be used. For a $3D$ system, this integral is $3N$ fold and using a numerical quadrature scheme would involve calculating the integrand at m^{3N} points for m grid points. Even for very small numbers of m and N, this value is extremely large [58]. MC however calculates such properties by accumulating the integrand at randomly generated values of the particle positions r^N distributed uniformly over the available interval. As the number of these random values tends to infinity this procedure yields a correct solution. However, in the case of the above integral, the Boltzmann factor causes the possible configurations to make non-uniform contributions and thus an importance-sampling scheme was devised in the Metropolis method.

MC methods are used for numerical integration, global optimization, queuing theory, structural mechanics, and solution of large systems of linear, partial differential or integral equations due to its simplicity, efficiency, and theoretical grounding. MC can sample the phase space of the system from a chosen statistical ensemble and is appropriate for calculating thermodynamic quantities or performing simulated annealing calculations. It is also usually easy to code in a high-level language as well as implement for systems without a proper intermolecular force law from the potential function [57]. However, it cannot be used to study time-dependent properties and is applicable only for configurations near equilibrium.

2.2.4 Molecular Dynamics

MD simulation is the simulation of motion molecules/atoms in a given system to determine the positions, forces and velocities of each molecule/atom at every state or time step. As a result, MD calculations are like computer experiments since the total system information is available at every step.

Intermolecular potential energy binds molecules in any system defined by the intermolecular potential function and MD simulation uses this definition to determine how the particles will interact with each other. The non-bonded interactions are usually defined by pair potentials, in which the total potential energy of a system is taken to be the sum of energy contributions from pairs of atoms. This pair potential is given by,

$$U(r_1, ..., r_N) = \frac{1}{2} \sum_{\substack{i,j=1 \\ i \neq j}}^{N} u_{ij} \tag{2.12}$$

Position vectors, r^N are obtained by solving Newton's equations of motion [55] as follows:

$$\frac{dv_i(t)}{dt} = a_i(t) \tag{2.13}$$

$$\therefore v_i(t) = a_i(t)t + v_{i0} \tag{2.14}$$

$$\frac{dr_i(t)}{dt} = v_i(t) \tag{2.15}$$

$$\therefore r_i(t) = v_i(t)t + r_{i0} = a_i(t)t^2 + v_{i0}t + r_{i0} \tag{2.16}$$

$$a_i(t) = \frac{F_i(t)}{m} = -\frac{1}{m}\frac{\partial U(r^N(t))}{\partial r_i} \tag{2.17}$$

Thus, the initial values of positions and velocities are set to calculate forces from the above equations numerically and the new position and velocities are obtained. Again the forces are computed to solve the equations of motions and this continues iteratively [55]. Once all the trajectories are obtained they can be analyzed to calculate other static and dynamic properties.

Properties like temperature can be determined without any additional parameters since the total information of the system (trajectories, energies, etc.) is available for each time step of the evolution. This convenience is not available in MC where temperature is included as an external parameter or in QM where temperature is simply not defined. MD evaluates heat capacities, compressibilities, and interfacial properties more efficiently than MC. MD also provides transport properties, which generally cannot be obtained using MC. MM and MD both are based on classical mechanics and have some fundamental similarities. Both the methods are computationally fast as well as can handle large systems of particles or atoms as compared to QM. Both the methods use interaction potentials usually obtained by QM calculations and their usability depends on the accuracy and validity of these interacting potentials. Quantum effects cannot be explained by either of the methods. However, the most important factor which differentiates MD from the rest of the methods of molecular modeling is its ability to capture the dynamics of the system and thereby the ease of calculation of related non-equilibrium properties.

2.3 Molecular Dynamics using LAMMPS

Developed at Sandia National Laboratories primarily by Steve Plimpton, Paul Crozier and Aidan Thompson, LAMMPS (Large-scale Atomic/Molecular Massively Parallel Simulator) is an open-source code designed to run classical MD simulation on parallel computers [59]. It can model liquid, solid or gaseous states of atomic, molecular, polymeric, metallic, biological, granular and coarse-grained systems using a wide range of force fields and boundary conditions. Initially written in FORTRAN, the current version is a rewrite in C++ and designed to be easily modified by the user to include new force fields, atom types, boundary conditions or diagnostics.

LAMMPS can run on a single processor or in parallel and therefore can run multiple simulations simultaneously (in parallel) from a single input script. The input script contains syntax for defining and using variables and formulas as well as for looping over runs and breaking out of loops [59]. It also consists of commands to define and create geometry, atom types, boundary conditions, force fields, simulation control parameters, and output directives. Thermodynamic information as well as customizable text files of required data is given as output at the end of the simulations. This data can further be used to visualize the simulations through appropriate tools or can be converted to several other popular formats to be used by other software for different analyses. LAMMPS provides a significant amount of flexibility to handle a wide range of molecular modeling problems and is most suitable for metallic systems. Thus, it was selected as the MD code of choice for the present work.

2.3.1 Input

LAMMPS starts the simulation run by reading the commands from an input script, which is essentially a text file. It reads the file one line at a time and executes the commands and takes some action accordingly. Therefore, positional order as well as the

hierarchy of commands is important. The structure of a typical LAMMPS input script has four parts [59] that are each described next:

2.3.2 Initialization

In this part of the script, parameters that need to be defined before creating any atoms or geometries are defined. These include the units, dimension (2D or 3D), boundary, and atom style (e.g. atomic, bond, charge, granular, molecular etc.). For the sake of simplifying the calculations, most of the MD programs use a system of units where dimensional quantities are made unit-less. This is especially advantageous for systems consisting of just one type of atoms where its mass becomes the fundamental unit. As a result, their momenta and velocities become numerically identical. If the parameters σ and ϵ of simple pair potentials like LJ are set to unity, then they do not appear explicitly in the simulation, thus saving a lot of calculation time [60]. Therefore, LAMMPS provides an option to run simulations in several systems of units.

MD simulations are usually performed on smaller systems containing at the most a few thousand atoms limited mostly by computational power. At this size the surface effects are dominating over the bulk due to the higher ratio of surface atoms to total atoms. These surface effects are actually important when simulating systems or studying phenomena at nano-scales. In such cases, the use of a non-periodic boundary is appropriate where atoms are lost if they cross the simulation boundary. On the other hand, when simulating a system as bulk or a part of it, such surface effects are not of interest and can be removed using periodic boundary conditions. In periodic boundary conditions, an atom exiting from one boundary re-enters from the opposite boundary with the same velocity vector. This guarantees the constancy of energy, number of atoms and volume [55]. LAMMPS provides both of these boundary conditions. Additionally, for the

non-periodic type, the shrink-wrapping option is available where the atoms, no matter how far they move, are encompassed within the simulation box.

2.3.3 Atom Definition

Atoms and geometries are created in this part of the script. A lattice command specifies the lattice structure along with the lattice constant for real units or the reduced density for LJ units. The lattice is a set of points in space specified by a unit cell and the number of basis atoms which is then replicated in all dimensions [59]. Atoms can then be created on the lattice positions using the *create atoms* command. The geometric extents of the atoms are determined by the *region* command that creates the simulation box using a basic specific shape (block, cone, cylinder etc.). Including or excluding different shapes using further parameters of the *region* command in conjunction with a *group* command can create complicated geometries. Masses of all types of atoms used in the simulation are specified by the mass command in this part of the script.

2.3.4 Settings

After defining the prerequisites and creating atoms and geometries, settings that govern the simulation are specified. The most important of the settings is specifying the force field used to compute the interactions between pairs of atoms or the potential function between pairs of bonded atoms. LAMMPS supports a large number of commonly used force fields including Buckingham, embedded atom method (EAM), alloy EAM, AI-REBO potential, AMBER, CHARMM, COMPASS, Lennard-Jones (LJ), Morse, Tersoff, TIP3P, and many more.

The initial velocities of the atoms need to be set here since the positions are already defined by the lattice command. Specifying the initial temperature of the simulation does this and the velocities are generated using this temperature by the *velocity* command.

This velocity can be set, scaled or time ramped as needed throughout the simulation. Control operations such as updating atom positions and velocities, controlling temperature (by velocity scaling or a Berendsen thermostat) and/or pressure (by a Nose/Hoover or a Berendsen barostat), applying forces, adding or removing heat etc. are achieved using the *fix* command. Positions and velocities are updated by performing constant NVE, NPT, and NVT time integration. Properties such as energy, pressure, temperature, stress, heat flux etc. can be calculated at any time for a group of atoms while kinetic energy, potential energy, stress, and damage can be obtained for individual atoms as well.

2.3.5 Run

The size of the time-step for the simulation must be specified before the simulation run can execute. The default value of the time-step is $0.005t^*$ for LJ units and 1 fs for *real* units. The simulation is run using the *run* command that is specified in the final part of the file. The number of time-steps for which the simulation will run is taken as an argument by this command. By default, LAMMPS uses velocity-Verlet algorithm to integrate the equations. The following finite difference equations based on Taylor's series expansion are used to integrate the equations of motion:

$$r(t+\Delta t) = r(t) + \Delta t v(t) + \frac{1}{2}\Delta t^2 a(t) \tag{2.18}$$

$$a(t+\Delta t) = -\frac{1}{m}\frac{\partial U(r^N(t+\Delta t))}{\partial r} \tag{2.19}$$

$$v(t+\Delta t) = v(t) + \frac{1}{2}\Delta t\left[a(t+\Delta t) + a(t)\right] \tag{2.20}$$

Velocity-Verlet is a stable, convenient and simple derivative of the original Verlet algorithm [61] that store positions, velocities and accelerations all at the same time, t. It is $\mathcal{O}(\Delta t^3)$ accurate for position as well as velocity and therefore minimizes round-off errors [57].

2.3.6 Output

Simulation output is provided in three different ways in LAMMPS: screen output with a corresponding *log* file, a *dump data* file, and if specified, a *restart* file. In the screen output, it prints the computational requirements and statistics, initial and final thermodynamic state of the system, and the total run time for the simulation. Additionally, thermodynamic information is printed at a specified time-step interval during the run.

The *dump* file can be customized and formatted to obtain preferred data such as coordinates, forces, velocities, etc. of atoms at desired time-step interval. The *xmovie* tool visualization tool provided in the LAMMPS package also uses this file, which is an X-based visualization package that animates the simulation and displays 2D projections of the domain.

The *restart* file writes out the instantaneous state of the simulation at user defined time intervals. This is particularly useful if the simulation needs to continue with precise atom trajectories from a previous run. Along with trajectories, it also stores all the information specified in the initialization and atom definition parts of the input script while the settings need to be provided again [59].

2.4 Benchmarking LAMMPS

In order to gain some confidence in the simulation procedure and the results obtained using LAMMPS, it was benchmarked to compare the findings to the work done by

Baidakov et al. [62] and subsequently to Kolafa and Nezbeda [63]. Baidakov et al. [62] on performed MD simulations on a Lennard-Jones (LJ) fluid with parameters corresponding to argon to calculate the pressure, internal energy and isochoric heat capacity for a range of temperatures and densities. Their simulation consisted of 208 data points over stable states as well as homogeneous meta-stable states of supersaturated vapor, superheated and super-cooled liquid. They compared their results with the highly accurate and widely used analytic and theoretical equation of state (EOS) proposed by Kolafa and Nezbeda for the LJ fluid. This equation is based on perturbed hard-sphere EOS with one or more theoretical terms and an empirical correction term.

In the current benchmarking, LAMMPS is used to perform MD simulation on LJ argon using a geometric model equivalent to Baidakov et al. Identical boundary conditions, number of atoms, and other LJ parameters were used, however, 30 data points were covered out of the 208 to compare the results of pressure and internal energy in the first set of simulations. In the second set, 41 data points were included but the internal energy was not compared. Furthermore, the pressure results were compared with those obtained from the EOS given by Kolafa and Nezbeda in the second set. Fewer data points were selected without prejudice in order to limit the amount of computational time and to avoid duplicating their entire work.

2.4.1 MD Simulation

Lennard-Jones potential, proposed by John Lennard-Jones in 1924, is used to describe the interactions between atoms in this MD simulation. It is by far the most popular potential model used in MD and approximates the interactions in inert gases reasonably well. The general form of this potential is given by

$$u(r) = \frac{A}{r^n} - \frac{B}{r^m} \tag{2.21}$$

The form of LJ potential most commonly used has $n = 12$ and $m = 6$ and is given by

$$u(r) = 4\epsilon \left[\left(\frac{\sigma}{r}\right)^{12} - \left(\frac{\sigma}{r}\right)^{6} \right] \tag{2.22}$$

This potential has its minimum equal to $-\epsilon$ at $r = 2^{\frac{1}{6}}\sigma$. The first term in the expression describes short-range repulsion while the second term describes attraction. For this set of simulations and onwards, the form of LJ potential used by LAMMPS is

$$u(r) = \begin{cases} 4\epsilon \left[\left(\frac{\sigma}{r}\right)^{12} - \left(\frac{\sigma}{r}\right)^{6} \right], & r \leq r_c \\ 0, & r > r_c \end{cases} \tag{2.23}$$

The cutoff radius r_c is used to limit the number of computations and the simulation time. The parameters ϵ, σ, and r_c are known as LJ parameters, which need to be specified as arguments for the potential function in LAMMPS.

2.4.2 Thermodynamic Quantities and Reduction of Units

For the sake of simplicity and convenience, as a standard practice in MD, all the quantities in the simulations and calculations are made unit-less. The values of ϵ,σ along with atomic mass, m and Boltzmann constant, k_B are used as reduction units for all the quantities. The masses, distances, energies etc. specified in the input are multiples of these fundamental values. The relevant quantities are defined as follows [59] [64]:

$$Distance, x^* = \frac{x}{\sigma} \tag{2.24}$$

$$Time, t^* = t \left(\frac{\epsilon}{m\sigma^2}\right)^{\frac{1}{2}} \tag{2.25}$$

$$Velocity, v^* = \frac{vt}{\sigma} \tag{2.26}$$

$$Energy, E^* = \frac{E}{\epsilon} \tag{2.27}$$

$$Force, F^* = \frac{F\sigma}{\epsilon} \tag{2.28}$$

$$Temperature, T^* = \frac{Tk_B}{\epsilon} \tag{2.29}$$

$$Pressure, P^* = \frac{P\sigma^3}{\epsilon} \tag{2.30}$$

$$Density, \rho^* = \frac{\rho\sigma^3}{m} \tag{2.31}$$

Thus, for a specific material, the values of m, ϵ, and σ should be used to convert the results from a unit-less LJ simulation into real quantities. In the present case for argon, $m = 6.64\times10^{-26}$ kg, $\epsilon = 1.65\times10^{-21}$ J, and $\sigma = 3.405\times10^{-10}$ m [55].

2.4.3 Model

A system with dimension 8×8×8 units was constructed in LAMMPS. Since the lattice structure of argon is fcc with 4 basis atoms (Figure 2.1), a system with a volume of 512 units would translate to 2048 atoms. Periodic boundary conditions were used in all three dimensions so that the atoms interact across the boundary to simulate bulk. Atoms therefore can exit one end and re-enter from the other end with the same trajectory.

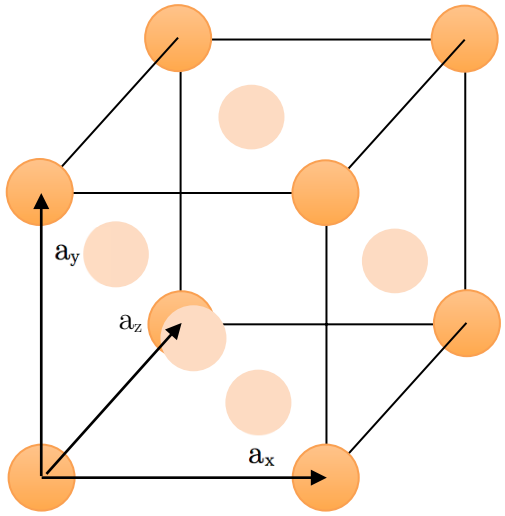

Figure 2.1: Face-Centered Cubic Structure

2.4.4 Simulation Inputs and Variables

Baidakov et al. had simulated the argon system by varying temperature and density to calculate other thermodynamic properties. Thus, these two are the most important variables for the simulation input. Specified density is achieved in LAMMPS by scaling the volume and therefore the dimensions of the system by a scale factor, which is given by

$$X = \left(\frac{\rho_{cell}}{\rho^*} \right)^{\frac{1}{d}} \tag{2.32}$$

$$\rho_{cell} = \frac{N}{V_{cell}} \tag{2.33}$$

Here ρ_{cell} is the unit cell density, ρ^* is the specified density, d is the dimensionality of the system, N is the number of basis atoms, and V_{cell} is the unit cell volume. The specified temperature of the system is maintained in LAMMPS by scaling the velocities of the

atoms at every certain number of time-steps during the simulation. This is given by the following equation:

$$T(t) = \frac{2m_i}{3Nk_B} \sum_{i=1}^{N} v_i^2(t) \tag{2.34}$$

Thermodynamic properties for $\rho^* < 0.001 - 1.2$ and $T^* = 0.35 - 2.0$ have been calculated in [62]. The cutoff radius for the potential was taken as $r_c^* = 6.78$ for $\rho^* < 0.82$ and half the system side for higher densities with $r_{c,min}^* = 5.975$. These values were matched in current simulations.

2.4.5 Calculations

MD calculated thermodynamic pressure and potential energy of the system using the following general equations

$$P = \frac{Nk_BT}{V} + \frac{1}{3V} \sum_i \sum_{<j} r_{ij} \frac{du(r_{ij})}{dr_{ij}} \tag{2.35}$$

$$E_p = \frac{1}{N} \sum_i \sum_{<j} u(r_{ij}) \frac{du(r_{ij})}{dr_{ij}} \tag{2.36}$$

Here the first term in the pressure equation is the ideal-gas contribution and the second term is of inter-atomic forces for a pair-wise additive potential [57]. The internal energy is just the average of the pair potential.

Specific unit-less forms of the above equations used by Baidakov et al. are

$$P^* = \frac{\rho^*}{3} \left(2e_k^* - \underbrace{\frac{1}{N} \sum_{i=1}^{N-1} \sum_{j=2}^{N} r_{ij}^* \frac{du(r_{ij}^*)}{dr_{ij}^*}}_{j>i, \quad r_{ij}^* \leq r_c^*} \right) - \frac{16\pi\rho^{*2}}{3r_c^{*3}} \tag{2.37}$$

$$E_p^* = \underbrace{\frac{1}{N}\sum_{i=1}^{N-1}\sum_{j=2}^{N} r_{ij}^* \frac{du(r_{ij}^*)}{dr_{ij}^*}}_{j>i,\quad r_{ij}^* \le r_c^*} - \frac{8\pi\rho^{*2}}{3r_c^{*3}} \tag{2.38}$$

Here, $e_k^* = (\frac{1}{2N})\sum_{i=1}^{N} v_i^{*2}$ is the kinetic energy per atom. The second terms in above equations are corrections introduced to include long-range interactions.

The analytic equations, which were used to compare the pressure results of the current simulations as well as the results of Baidakov et al., are as follows [63]:

$$\frac{P}{\rho T} = z_{HS} + \rho(1 - 2\gamma\rho^2)exp(-\gamma\rho^2)\Delta B_2(T) + \sum_{ij} jC_{ij}T_2^{i-1}\rho^j \tag{2.39}$$

where,

$$z_{HS} = \frac{1 + \eta + \eta^2 - \frac{2}{3}\eta^3(1+\eta)}{(1-\eta)^3} \tag{2.40}$$

$$\eta = \frac{\pi}{6}\rho d(T)^3 \tag{2.41}$$

$$d(T), \Delta B_2(T) = \sum_i C_i T_2^i + C_{ln} lnT \tag{2.42}$$

C_i and C_{ij} are coefficients provided in Table 2.1 and Table 2.2 and $\gamma = 1.92907278$.

Table 2.1: Coefficients for $d(T)$ and $\Delta B_2(T)$

$\boldsymbol{d}$		$\boldsymbol{\Delta B_2(T)}$	
i	C_i	i	C_i
-2	0.01111752	-7	-0.58544980
-1	-0.07638390	-6	0.43102052
0	1.08014225	-5	0.87361369
1	0.00069313	-4	-4.13750000
ln	-0.06392100	-3	2.90616279
		-2	-7.02181960
		0	0.02459877

Table 2.2: Coefficients for PVE EOS

$\boldsymbol{i}$	$\boldsymbol{j}$	$\boldsymbol{C_{ij}}$	$\boldsymbol{i}$	$\boldsymbol{j}$	$\boldsymbol{C_{ij}}$
0	2	2.01546797	-2	2	29.34470520
0	3	-28.17881600	-2	3	-112.35357000
0	4	28.28313850	-2	4	170.64909000
0	5	-10.42402900	-2	5	-123.06669000
-1	2	-19.58371700	-2	6	34.42288970
-1	3	75.62340290	-4	2	-13.37032000
-1	4	-120.70587000	-4	3	65.38059570
-1	5	93.92740330	-4	4	-115.09233000
-1	6	-27.37737400	-4	5	88.91973080
-2	2	29.34470520	-4	6	-25.62099900

2.4.6 Results and Discussion

All the calculations are made in the NVE ensemble for a volume V, internal energy E and N number of atoms or particles. The size of time-steps used was $\Delta t^* = 0.004637$ which corresponds to ~10 fs for the LJ parameters of argon. This was the same value used by [62]. According to the authors, this size of time-step ensured the conservation of energy at all temperatures and densities. Average values of pressure and internal energy were obtained over 20,000 time-steps. The authors, however, have averaged the same over $(0.1 - 1.0) \times 10^6$ time-steps. In the present set of simulations higher time-step runs were performed on some of the data points to compare the difference in the averages obtained. Significant improvement was not seen at 5×10^5 time-steps, which required about 18 hours for the run, and hence all of the runs on remaining data points were averaged over 2×10^4 time-steps.

Table 2.3 shows the results of simulation 1 where P^* and E_p^* are compared with the results of [62]. It can be seen that pressure at most of the data points with lower density values show a good agreement with [62]. At higher densities the discrepancies in values are large. A similar trend was observed for internal energy values, which are in good agreement except for very low and very high-density values. Simulation 2 results are shown in Table 2.5. In this case, only P^* values are considered but are additionally compared to the analytic EOS by Kolafa and Nezbeda [63]. Again, large discrepancies are observed at points, which are closer to the points with similar discrepancies in simulation 1.

The simulation data points are plotted on the $T^* - \rho^*$ phase diagram (Figure 2.2) adopted from [62].

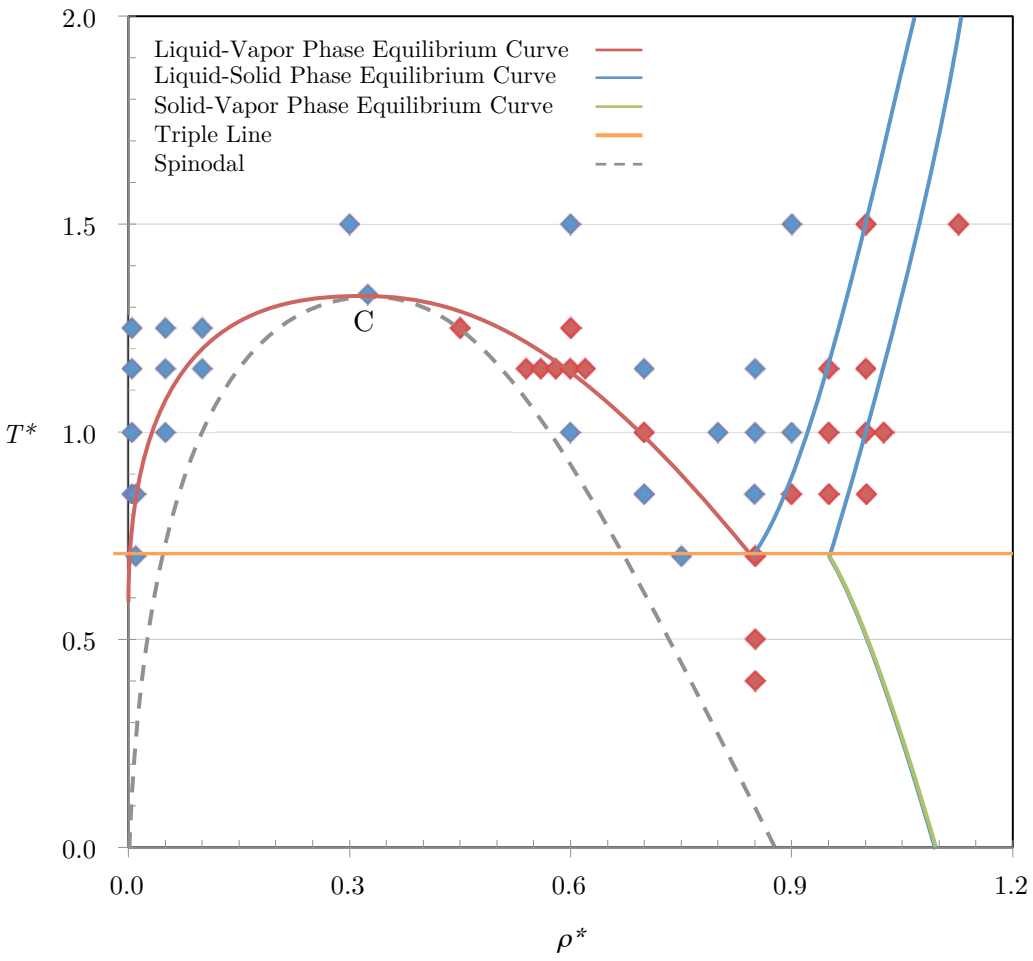

Figure 2.2: Phase diagram of LJ fluid [62]

The authors used local equations of state for gas liquid and crystal phases for this phase diagram which are given by

$$p^* = \sum_{j=0}^{n} \sum_{i=0}^{m} a_{ij} \rho^{*j} T^{*i} \tag{2.43}$$

Here, the coefficients, a_{ij} and the exponents, n and m, were determined by regression analysis and their values could be found elsewhere [62]. In Figure 2.2, blue and red data points represent agreement and disagreement in the results respectively. It can be seen that all the red points are on or very close to the phase change lines on the diagram.

Although not as large, similar disagreements have been observed [62] when comparing their results to the EOS. According to the authors as the phase change lines are approached, the intensity of density and energy fluctuations and the correlation length increase giving rise to instabilities. These, in turn, generate the disagreements in the data as mentioned earlier. At this point, it must also be noted that the analytic EOS [63] is reliably applicable to the temperature interval from $T^* = 0.68 - 10$. Hence, it should not be entirely unexpected that some of the largest errors are seen below $T^* = 0.7$ in this work as well as for [62]. For the remaining data points (blue), a good agreement with the results of [62] and [63] is seen with error below 1%.

LJ fluids are some of the simplest models of liquids yet are a benchmark in studying thermodynamic and kinetic properties through molecular modeling. LAMMPS is used here as a molecular dynamics package to simulate LJ argon and thereby calculate its pressure and internal energy. EOS for LJ fluid, which were developed analytically and using results of several computer experiments, along with a similar MD work were used to learn and validate LAMMPS.

Table 2.3: Simulation 1 Pressure Results

ρ^*	T^*	V^*	P^*			
			LAMMPS	**LAMMPS Corrected**	**Paper** [62]	ΔP^* %
0.85	0.4	2409.42	-3.5783297	-3.6171713	-2.052	76.28
0.85	0.5	2409.42	-2.8269407	-2.8657823	-1.283	123.37
0.01	0.7	204800	0.0063645	0.00635913	0.0063	0.94
0.75	0.7	2730.667	-0.8533896	-0.8836297	-0.8742	1.08
0.85	0.7	2409.42	0.06787979	0.02903816	0.1089	73.34

ρ^*	T^*	V^*	P^*			
			LAMMPS	**LAMMPS Corrected**	**Paper** [62]	ΔP^* %
0.005	0.85	409600	0.00411592	0.00411458	0.0040998	0.36
0.01	0.85	204800	0.00793997	0.0079346	0.007901	0.43
0.7	0.85	2925.71	-0.4593475	-0.4856899	-0.4864	0.15
0.85	0.85	2409.42	1.10414471	1.06530309	1.0571	0.78
0.005	1	409600	0.00488871	0.00488737	0.0048681	0.40
0.05	1	40960	0.03730626	0.03717186	0.0369	0.74
0.6	1	3413.33	-0.2449998	-0.2643534	-0.258	2.46
0.7	1	2925.71	0.03080046	0.00445804	0.0158	71.78
0.85	1	2409.42	1.98714124	1.94829962	1.9443	0.21
1	1	2048	3.70821716	3.65445713	7.5326	51.48
0.005	1.15	409600	0.005648	0.00564666	0.0060375	6.47
0.05	1.15	40960	0.04631628	0.04618188	0.04597	0.46
0.1	1.15	20480	0.07149877	0.07096117	0.0705	0.65
0.6	1.15	3413.33	0.06117382	0.04182021	0.0439	4.74
0.7	1.15	2925.71	0.52955025	0.50320784	0.5057	0.49
0.85	1.15	2409.42	2.81878048	2.77993886	2.783	0.11
1	1.15	2048	4.85583105	4.80207102	8.8174	45.54
0.005	1.25	409600	0.00614196	0.00614062	0.0061384	0.04
0.05	1.25	40960	0.05204664	0.05191224	0.05178	0.26
0.1	1.25	20480	0.08504561	0.08450801	0.08413	0.45
0.45	1.25	4551.11	0.08187444	0.07098804	0.0737	3.68

ρ^*	T^*	V^*	P^*			
			LAMMPS	**LAMMPS Corrected**	**Paper** [62]	ΔP^* %
0.6	1.25	3413.33	0.26809649	0.24874287	0.2523	1.41

Table 2.4: Simulation 1 Internal Energy Results

ρ^*	T^*	V^*	**U***	**ρ***	**T***	**V***
			LAMMPS	*LAMMPS Corrected*	*Paper* [62]	ΔU*%
0.85	0.4	2409.42	-6.7481059	-6.7709539	-6.522	3.82
0.85	0.5	2409.42	-6.6277041	-6.6505521	-6.388	4.11
0.01	0.7	204800	-0.1113784	-0.1116472	-0.127	12.09
0.75	0.7	2730.667	-5.4482582	-5.4684183	-5.4674	0.02
0.85	0.7	2409.42	-6.1355784	-6.1584264	-6.1438	0.24
0.005	0.85	409600	-0.0441586	-0.044293	-0.052	14.82
0.01	0.85	204800	-0.0928407	-0.0931095	-0.105	11.32
0.7	0.85	2925.71	-4.978783	-4.997599	-4.997	0.01
0.85	0.85	2409.42	-5.9510445	-5.9738925	-5.976	0.04
0.005	1	409600	-0.041084	-0.0412184	-0.046	10.39
0.05	1	40960	-0.470963	-0.472307	-0.48	1.60
0.6	1	3413.33	-4.2097949	-4.2259229	-4.236	0.24
0.7	1	2925.71	-4.8720824	-4.8908985	-4.891	0.00
0.85	1	2409.42	-5.7951054	-5.8179534	-5.8179	0.00
1	1	2048	-7.0308361	-7.0577161	-6.345	11.23

ρ^*	T^*	V^*	U^*	ρ^*	T^*	V^*
			LAMMPS	*LAMMPS Corrected*	*Paper* [62]	$\Delta U^*\%$
0.005	1.15	409600	-0.0401964	-0.0403308	-0.043	6.21
0.05	1.15	40960	-0.4233646	-0.4247086	-0.431	1.46
0.1	1.15	20480	-0.8660551	-0.8687431	-0.874	0.60
0.6	1.15	3413.33	-4.1170899	-4.1332179	-4.134	0.02
0.7	1.15	2925.71	-4.7734048	-4.7922208	-4.7918	0.01
0.85	1.15	2409.42	-5.6459612	-5.6688092	-5.668	0.01
1	1.15	2048	-6.8426366	-6.8695166	-6.127	12.12
0.005	1.25	409600	-0.0396069	-0.0397413	-0.041	3.07
0.05	1.25	40960	-0.4074324	-0.4087764	-0.41	0.30
0.1	1.25	20480	-0.8086863	-0.8113743	-0.817	0.69
0.45	1.25	4551.11	-3.1403556	-3.1524516	-3.155	0.08
0.6	1.25	3413.33	-4.0648208	-4.0809488	-4.08	0.02

Table 2.5: Simulation 2 Results

ρ^*	T^*	V^*	P^*				ΔP^* %	
			LAMMPS	**LAMMPS Corrected**	**Paper** [62]	**EOS** [63]	**LAMMPS -EOS**	**Paper-EOS**
0.85	0.4	2409.42	-3.5783297	-3.6171713	-2.052	-1.77679	103.58	15.49
0.85	0.5	2409.42	-2.8269407	-2.8657823	-1.283	-1.20314	138.19	6.64
0.01	0.7	204800	0.0063645	0.00635913	0.0063	0.00630	0.94	0.00
0.75	0.7	2730.667	-0.8533896	-0.8836297	-0.8742	-0.86862	1.73	0.64

ρ^*	T^*	V^*	P^*				ΔP^* %	
			LAMMPS	**LAMMPS Corrected**	**Paper** [62]	**EOS** [63]	**LAMMPS -EOS**	**Paper-EOS**
0.85	0.7	2409.42	0.06787979	0.02903817	0.1089	0.11663	75.10	6.63
0.005	0.85	409600	0.00411592	0.00411458	0.0040998	0.00410	0.36	0.00
0.01	0.85	204800	0.00793997	0.0079346	0.007901	0.00790	0.46	0.03
0.7	0.85	2925.71	-0.4593475	-0.4856899	-0.4864	-0.48145	0.88	1.03
0.85	0.85	2409.42	1.10414471	1.06530309	1.0571	1.06361	0.16	0.61
0.9	0.85	2275.55	1.29445412	1.2509085	2.2305	2.24861	44.37	0.81
0.95	0.85	2155.79	0.96030594	0.91178751	3.8959	3.88109	76.51	0.38
1	0.85	2048	2.54658411	2.49282408	6.179	6.00773	58.51	2.85
0.005	1	409600	0.00488871	0.00488737	0.0048681	0.00487	0.42	0.02
0.05	1	40960	0.03730626	0.03717186	0.0369	0.03695	0.61	0.12
0.6	1	3413.33	-0.2449998	-0.2643534	-0.258	-0.26039	1.52	0.92
0.7	1	2925.71	0.03080046	0.00445804	0.0158	0.01777	74.92	11.11
0.85	1	2409.42	1.98714124	1.94829962	1.9443	1.95454	0.32	0.52
0.9	1	2275.55	3.30307509	3.25952947	3.2679	3.28981	0.92	0.67
0.95	1	2155.79	2.10194922	2.05343079	5.0888	5.09576	59.70	0.14
1	1	2048	3.70821716	3.65445713	7.5326	7.44448	50.91	1.18
1.025	1	1998.05	4.81980207	4.76332044	9.029	8.84509	46.15	2.08
0.005	1.15	409600	0.005648	0.00564666	0.0060375	0.00563	0.28	7.22
0.05	1.15	40960	0.04631628	0.04618188	0.04597	0.04592	0.58	0.11
0.1	1.15	20480	0.07149877	0.07096117	0.0705	0.07090	0.08	0.57
0.54	1.15	3792.6	-0.0209953	-0.0366717	-0.031	-0.03169	15.73	2.17

ρ^*	T^*	V^*	P^*				ΔP^* %	
			LAMMPS	**LAMMPS Corrected**	**Paper** [62]	**EOS** [63]	**LAMMPS -EOS**	**Paper-EOS**
0.56	1.15	3657.14	-0.0043973	-0.0212565	-0.0172	-0.01496	42.11	14.99
0.58	1.15	3531.03	0.01570569	-0.0023792	0.007	0.01124	121.17	37.71
0.6	1.15	3413.33	0.06117382	0.04182021	0.0439	0.04903	14.70	10.45
0.62	1.15	3303.23	0.11459825	0.09393289	0.0954	0.10080	6.81	5.36
0.7	1.15	2925.71	0.52955025	0.50320784	0.5057	0.50553	0.46	0.03
0.85	1.15	2409.42	2.81878048	2.77993886	2.783	2.79645	0.59	0.48
0.95	1.15	2155.79	3.33495819	3.28643976	6.2195	6.23599	47.30	0.26
1	1.15	2048	4.85583105	4.80207102	8.8174	8.77728	45.29	0.46
0.005	1.25	409600	0.00614196	0.00614062	0.0061384	0.00614	0.03	0.01
0.05	1.25	40960	0.05204664	0.05191224	0.05178	0.05175	0.31	0.06
0.1	1.25	20480	0.08504561	0.08450801	0.08413	0.08416	0.41	0.03
0.45	1.25	4551.11	0.08187444	0.07098804	0.0737	0.06884	3.12	7.06
0.6	1.25	3413.33	0.26809649	0.24874287	0.2523	0.25625	2.93	1.54
0.3	1.5	6826.67	0.23147907	0.22664067	0.2262	0.22488	0.78	0.59
0.6	1.5	3413.33	0.78380691	0.7644533	0.7675	0.76936	0.64	0.24
0.9	1.5	2275.55	6.4138259	6.37028027	6.3617	6.38458	0.22	0.36
1	1.5	2048	7.68530801	7.63154798	11.6027	11.60679	34.25	0.04
1.125	1.5	1820.44	15.8147464	15.7467064	22.741	22.61349	30.37	0.56

Chapter 3

Interatomic Potential, Integration Algorithm and Time-step

In molecular dynamics (MD), the interactions between the particles of a system are governed by the potential energy function. The potential energy of the system, which is a function of the relative positions of each particle, constantly varies since each particle is interacting with all of its neighbors simultaneously. The determination of positions and velocities of the atoms or particles in a phase space therefore is not straightforward and requires solving the equations of motion presented in an earlier section. Due to the large number of particles in the system such as the one studied in this work, any analytical solution will be impossible for such a complex system. Hench, this is achieved by integrating the equations of motions to obtain an approximate solution using numerical methods, particularly, the finite difference methods.

3.1 Interatomic Potential: Embedded Atom Method

Recalling, the equations of motions, which need to be solved to obtain the trajectories are

$$\frac{dr_i}{dt} = v_i \tag{3.1}$$

$$\frac{d^2r_i}{dt^2} = a_i \tag{3.2}$$

$$F_i = m_i a_i = -\frac{\partial U(r_i)}{\partial r_i} \tag{3.3}$$

The interatomic potential energy function, U, describes the dependence of the potential energy of a system on the coordinates of the atoms and therefore, defines the interactions of the atoms in the system. A simplest form of the potential energy function can be written as

$$U(r_1, ..., r_N) = \frac{1}{2} \sum_{\substack{i,j=1 \\ i \neq j}}^{N} u_{ij} \tag{3.4}$$

In this, the total potential energy of a system is taken to be the sum of energy contributions from pairs of atoms and therefore is called a pair potential (e.g. Lennard-Jones potential, Morse potential) [55]. Here, the three-body and many-body contributions of the interatomic interactions are neglected to simplify the simulations and expand the calculability of trajectories and therefore various properties. The pair-potentials allow fast computations of MD experiments with as many as 10^8 atoms [65]. However, to describe the interatomic interactions more accurately many-body contributions cannot be neglected. The pair-potentials effectively consider the various atomic bonds independent of each other, which is not the case in general and therefore the approximation is erroneous at times. In order to describe the elastic properties of a metal, pair-potentials need a volume-dependent energy term. However, at the atomic scale, the exact boundary of the volume at the surface is ambiguous and therefore surface effects cannot be modeled accurately using pair-potentials [66]. Additionally, in pair-potentials, the ratio of vacancy-formation energy to the cohesive energy is 1 however, for fcc metals this ratio is 0.35 [67].

The embedded-atom method (EAM) interatomic potential, proposed by Daw and Baskes [66], overcomes these shortfalls of pair-potentials. In the EAM, the total cohesive energy of a metallic system is expressed in terms of the electrostatic pair interactions plus an embedding energy, which is the energy required to embed an atom into the electron density created by the surrounding atoms. This is given by

$$U(r_i) = \sum_i G_i \left[\sum_{j \neq i} \rho_j(r_{ij}) \right] + \frac{1}{2} \sum_{i,j \neq i} u(r_{ij}) \tag{3.5}$$

Here, G_i is the energy required to embed atom i into electron density ρ_j created by the surrounding atoms and $u(r_{ij})$ is the electrostatic pair-potential between atoms i and j separated by distance r_{ij}. Thus, the EAM effectively includes the many-body contributions. In metals, the electron density at the surface is different from the bulk. In features or structures that are in the nano-scale, the surface interactions are more significant and therefore, the local electron density consideration is important to describe metallic nano-systems. The EAM allows the electron density to vary between surface and the bulk and as a result accurately describes bulk and defect properties (energy, structural, mechanical, and thermal properties) of metals (specially, fcc metals [68]) and metal alloys [69]. Therefore, the EAM was used in the current work to describe the metallic interactions of an asperity pair.

The G, ρ, and u functions in equation (3.5) are analytic expressions with coefficients that are fit to experimentally determined spline for U [69]. To obtain the force equation, the derivatives of equation (3.5) are taken analytically in LAMMPS and this force equation is given by

$$F_i = -\sum_{i,j \neq i} \left[G_i' \rho_{ij}' + G_j' \rho_{ji}' + u_{ij}' \right] r_{ij} \tag{3.6}$$

3.2 Integration Algorithm: Velocity-Verlet Method

The standard tools for solving initial-value problems such as equations (3.1) and (3.2) are the finite difference methods since it is the approximate solution that we are looking for in the absence of an exact analytical one. The fundamental idea of these

methods is that they replace differentials, such as dr and dt in the above equations with finite differences Δr and Δt.

$$\frac{r_i(t+\Delta t) - r_i(t)}{\Delta t} \cong v_i \tag{3.7}$$

$$\frac{v_i(t+\Delta t) - v_i(t)}{\Delta t} \cong a_i \tag{3.8}$$

Thus, the differential equations now become the finite-difference equations and the difference is taken over a small but finite time-step Δt. The basic concept is that for the given positions, velocities and accelerations of the particles we try to find or approximate the positions, velocities and accelerations after Δt, which is constant. The time-step size is usually selected so as to minimize the solution time without sacrificing the accuracy desired for a particular finite difference method.

The basic finite difference approximation for the velocity of a particle is given by equation (3.7), which arises from the calculus of finite differences. As $\Delta t \to 0$, the approximation keeps improving by the definition of a derivative, however, for any finite Δt, this will never be an exact solution. To understand how close the approximation is (and eventually develop a finite difference method) a Taylor's series expansion for the position of a particle from time t to $t+\Delta t$ is implemented.

$$r_i(t+\Delta t) = r_i(t) + \frac{dr_i(t)}{dt}\Delta t + \frac{1}{2}\frac{d^2 r_i(t)}{dt^2}\Delta t^2 + \mathcal{O}(\Delta t^3) \tag{3.9}$$

$$r_i(t+\Delta t) = r_i(t) + v_i(t)\Delta t + \frac{1}{2}a_i(t)\Delta t^2 + \mathcal{O}(\Delta t^3) \tag{3.10}$$

Similarly, for the velocity and the acceleration of a particle from time t to $t+\Delta t$ the Taylor's expansions are

$$v_i(t+\Delta t) = v_i(t) + a_i(t)\Delta t + \frac{1}{2}b_i(t)\Delta t^2 + \mathcal{O}(\Delta t^3) \tag{3.11}$$

$$a_i(t+\Delta t) = a_i(t) + b_i(t)\Delta t + \mathcal{O}(\Delta t^2) \tag{3.12}$$

Here b_i represents the third derivative of the position with respect to time. Multiplying both sides of equation (3.12) by $\Delta t/2$ and rearranging gives,

$$\frac{1}{2}b_i(t)\Delta t^2 = \frac{1}{2}\Delta t(a_i(t+\Delta t) - a_i(t)) + \mathcal{O}(\Delta t^3) \tag{3.13}$$

Substituting this in equation (3.11) gives,

$$v_i(t+\Delta t) = v_i(t) + \frac{1}{2}\Delta t(a_i(t+\Delta t) + a_i(t)) + \mathcal{O}(\Delta t^3) \tag{3.14}$$

Equations (3.10) and (3.14) constitutes the velocity-Verlet method used in an algorithm to obtain the trajectories. The algorithm implementation, with the trajectories at time t already known, is as follows:

1. Calculate $r_i(t+\Delta t) = r_i(t) + v_i(t)\Delta t + \frac{1}{2}a_i(t)\Delta t^2$ where $a_i(t) = F_i(t)/m_i$
2. Calculate $F_i(t+\Delta t)$ using equation (3.6)
3. Calculate $v_i(t+\Delta t) = v_i(t) + \frac{1}{2}\Delta t(a_i(t+\Delta t) + a_i(t))$ where $a_i(t+\Delta t) = F_i(t+\Delta t)/m_i$

Thus the new trajectories at time $t+\Delta t$ are now known and this loop can be executed till the desired time duration.

There are several finite difference methods available for use in MD simulations to integrate the equations of motion. However, many of them are interrelated or share the origin with minor variations [60]. The most time consuming step in the integration algorithm is the calculation of the forces on the particle and therefore a good choice of a

finite difference method cannot have multiple steps for this calculation [70]. Since the time required to compute the interactions is smaller compared to that required integrating the equations of motion, the algorithm speed is not very important. Nonetheless, the velocity-Verlet method is fast, efficient and is fairly simple and easy to program [58]. This method is $\mathcal{O}(\Delta t^3)$ accurate and therefore not one of most accurate methods available for solving the equations of motions. On the other hand, this is a time reversible method that has moderate short-term energy conservation but very good long-term energy conservation [71]. Neither a detailed discussion on the advantages or the disadvantages of this algorithm is provided here, nor an effort made to justify the selection of this algorithm since this was the only choice available with LAMMPS.

3.3 Time-step

A good MD simulation algorithm should be able to compute the trajectories as accurately as possible. Unfortunately there is no direct method to test the algorithm to verify the accuracy of the trajectories since an analytic solution to such complex systems is not possible. Therefore, there is no direct method to compare available simulation algorithms except to test on differential equations whose analytical solution is known. This would still be an approximate idea at best to prove the merit of any particular simulation algorithm for use with more challenging problems. Fortunately, we do not need the trajectories to be precise; the solution of the equation of motion should be able to give us states belonging to the statistical micro-canonical ensemble while conserving energy and momentum [60]. However, this does not mean we can meaningfully use highly inaccurate trajectories but that getting close to the true trajectories is good enough.

For given initial conditions, any two trajectories can diverge exponentially even if they were initially identical at the beginning. It would be unrealistic that any approximate method of solution like any finite difference method will provide exact

trajectories. This can be primarily attributed to any integration error caused by the accuracy of the finite difference method or the implementation of the simulation algorithm. The accuracy to which the finite difference method approximates the exact solution, which is given by the first nonzero term omitted from the Taylor series, is called the truncation error. For the velocity-Verlet method this error is $\mathcal{O}(\Delta t^3)$ and is the local truncation error as this is for a given time step. This local truncation error accumulates over every time step for the total simulation time which is known as the global truncation error and is $\mathcal{O}(\Delta t^2)$ for the velocity-Verlet method [57]. The integration error arising from the implementation of the simulation algorithm is the round-off error. This comprises of all the errors associated with the rounding of the calculations to a certain number of significant digits by the computational system. Again, the round-off error has the local and global parts with the same meaning as before.

Both, the truncation error and the round-off error are a function of the time step size, Δt. From the computational standpoint it is desirable to use a larger time step so as to complete a simulation in a reasonably acceptable amount of time considering the fact that some of the simulation runs performed in this work took several days to complete. However, larger time steps will result in less accurate computations of trajectories and degrade the energy conservation. To achieve the closest prediction to the true trajectories, the time step size should be as small as possible. This means there will be a larger number of time steps for a given simulation time which means a large number of calculations and therefore the accumulation of round-off errors could be significant. This opposing effect of the time step size on the truncation error and the round-off error makes it critical to select the time-step judiciously. Furthermore, stability of the simulation algorithm is also necessary so as to realize any useful results from an MD simulation. Depending on the simulation algorithm it is necessary to check how the errors propagate and whether there are amplified and become unstable. Again, most of the algorithms are only stable for a critical value of the time step size [57]. Therefore, the optimum value of the time step size

should be determined empirically so as to achieve good quality trajectories while consuming less computational time.

One of the most important aspects to be considered while selecting a time step size is the mean time between particle collisions or the frequency of motion of the particles. Logically, if the time step size is larger than the mean time of collisions or the period of the highest frequency motion of the particle, then the simulation will not capture the true dynamics of the system being studied [57,72]. The highest vibrational frequencies for bulk metallic systems are in the range 6 - 12 THz [72]. Therefore, the time period for this will be approximately in the range 0.08 - 0.16 ps. The time step size should be much smaller than this in order to follow the dynamics closely. One common practice is to select the time step size such that a minimum of 5 - 10 integration points per time period are performed which would give a range of 0.016 - 0.008 ps. In order to improve upon this estimation, an effective way would be to calculate the velocity autocorrelation function (VACF) for the given system. The VACF is a type of time correlation function that measures how the value of a dynamic quantity like the velocity of particles relates with itself at a shifted reference time. This is given by ([57]),

$$\psi(t) = \frac{1}{MN} \sum_{k}^{M} \sum_{i}^{N} v_i(t_k) v_i(t_k + t) \tag{3.15}$$

$$M = L - \frac{t}{\Delta t} \tag{3.16}$$

where L is the discrete times for which the velocities v_i are stored for N atoms, a time step of size Δt, reference time of t_k, and a delay time of t.

The VACF provides some important information about the dynamics of a system as to how strong or weak the interaction forces are between the particles as well as the mean time of collisions between the particles. For this, a simulation was run for a 5 nm radius hemispherical copper asperity consisting of 45163 atoms at 300 K using the EAM

potential on LAMMPS. The time step used was 0.002 ps and the simulation was run for 2000 time steps with velocities stored at every 10 time-steps for all the atoms. Using the above equation the VACF was calculated and is plotted in figure 1.

Figure 3.1 shows that the VACF oscillates strongly between positive and negative values suggesting that the atoms are vibrating and/or colliding and therefore reversing their velocities. These oscillations decay with time and become uncorrelated eventually. The first zero crossing of the VACF is however of prime significance. It gives an idea about the mean time period of the frequency motion or the collisions of the atoms and can be used to determine a suitable time step size for the simulation runs. Generally, 1%-10% of the first zero crossing of the VACF is considered as an optimum time step size to achieve reasonably accurate trajectories [59]. Figure 3.2 shows the VACF for all values of reference time where as Figure 3.2 shows the average value of the VACF over all the reference times. In this case the first zero crossing is at 0.1 ps and therefore the optimum range for the time step size is $\Delta t = 0.001 - 0.01$ ps. Therefore, a conservative choice of a time-step size of 0.002 ps was made, which is one of the most commonly, used time step size when simulating metallic nano-systems. Recently however, Villarreal et al. [72] have shown that it is possible to get good trajectories and therefore good energy conservation for metallic systems with a much larger time step size. They have also used LAMMPS with a modified version of the EAM potential to simulate pure metallic systems. According to them, for copper nano-systems, a time step size of up to 0.015 yields reasonably low energy drift thereby greatly reducing the total simulation time. However, this will not be implemented in the current work.

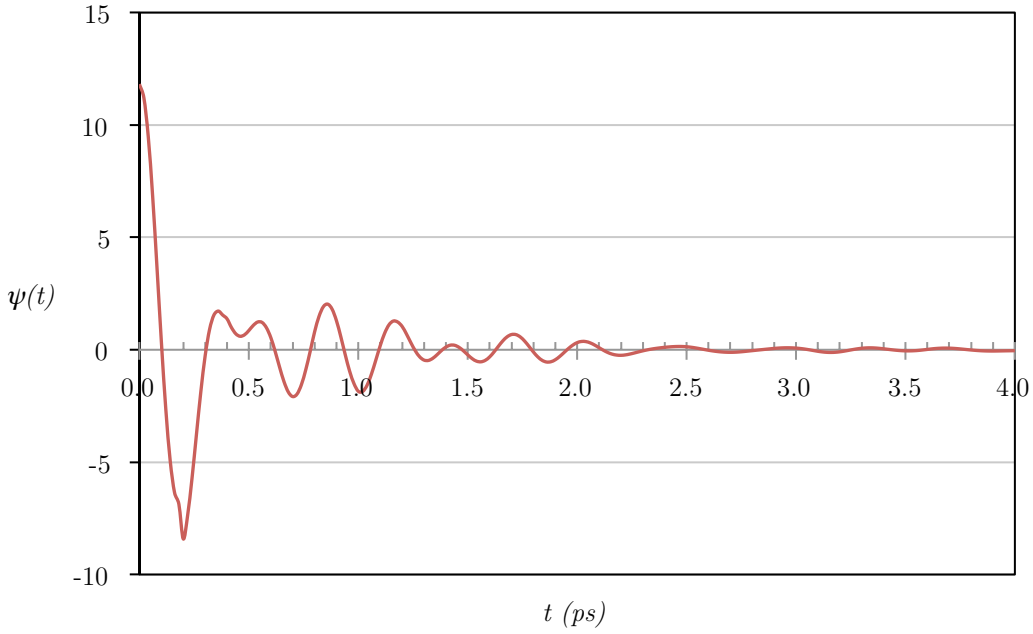

Figure 3.1: The velocity autocorrelation function for 5 nm size copper asperity at 300K with 45163 atoms and reference time $t_0 = 0$.

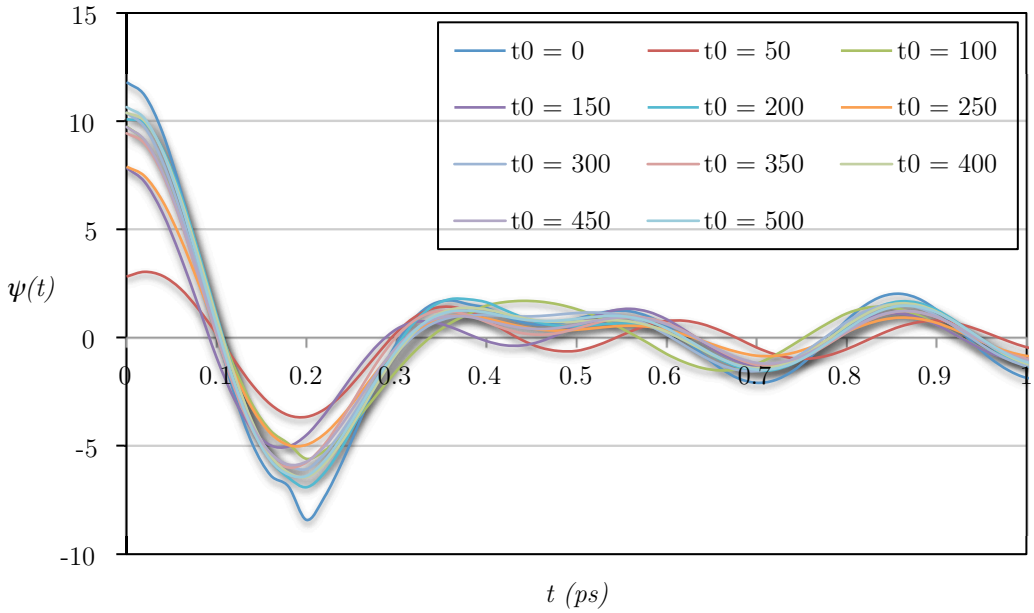

Figure 3.2: The velocity autocorrelation function for 5 nm size copper asperity at 300K with 45163 atoms for all reference times.

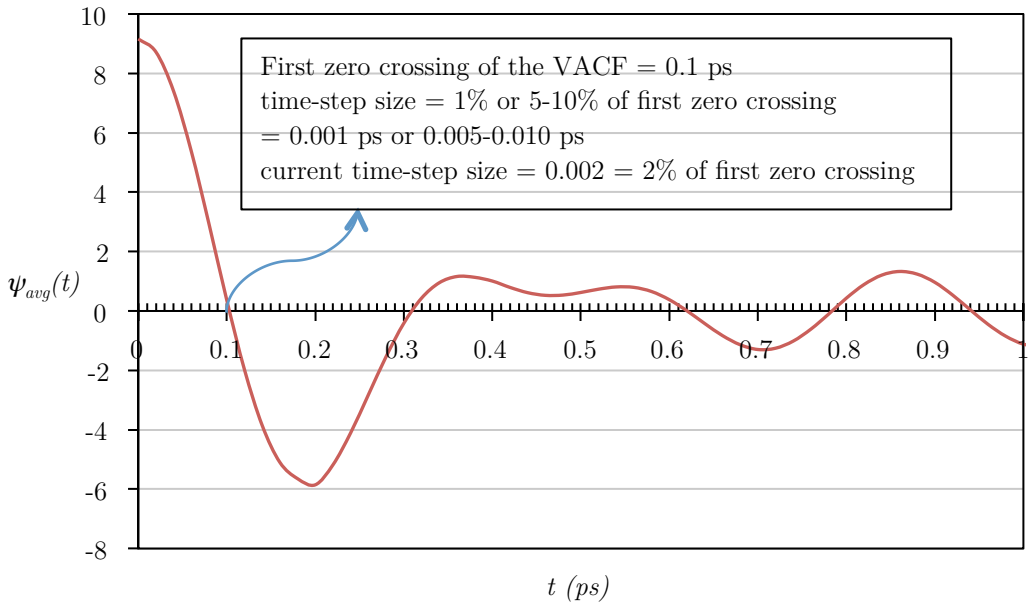

Figure 3.3: The average velocity autocorrelation function for 5 nm size copper asperity at 300 K with 45163 atoms.

3.4 Calculation of Static and Dynamic Properties

Once the trajectories of all the particles have been computed satisfactorily, macroscopic properties can be calculated. For an NVE ensemble, any macroscopic property A, can be defined as some function of the positions and the momenta of the particles in the system which is at equilibrium. For some finite duration of time t, this property can be averaged over time as [57]

$$\langle A \rangle = \frac{1}{M} \sum_{k=1}^{M} A\left(r^N(k\Delta t), p^N(k\Delta t)\right) \tag{3.17}$$

Here r^N and p^N are the positions and the momenta respectively of N particles taken over M discrete times with time-step, Δt.

Invoking the energy conservation, it can be written as

$$E = E_k(p^N) + E_p(r^N) = constant \tag{3.18}$$

Using equation (3.17) the average kinetic energy for particles of mass, m as well as the absolute temperature, T is

$$E_k = \frac{1}{2mM} \sum_{k=1}^{M} \sum_{i=1}^{N} p_i(k\Delta t) = \frac{3}{2} N k_B T \tag{3.19}$$

The average potential energy is given by the potential function, $u(r_{ij})$

$$E_p = \frac{1}{M} \sum_{k=1}^{M} \sum_{i,i<j} \sum_{j} u\left(|r_{ij}(k\Delta t)|\right) \tag{3.20}$$

The pressure of the system consists of an ideal-gas contribution and the potential function accounting for the inter-atomic forces and is given by

$$P = \frac{N k_B T}{V} + \frac{1}{3MV} \sum_{k=1}^{M} \sum_{i,i<j} \sum_{j} r_{ij}(k\Delta t) \frac{du\left(|r_{ij}(k\Delta t)|\right)}{dr_{ij}} \tag{3.21}$$

3.5 Summary

The positions and velocities of the atoms or particles in a phase space are determined by solving the equations of motion. In the absence of an analytical solution in a complex system with large number of particles, the equations of motions are integrated using finite difference methods to obtain an approximate solution. The finite difference method used as well as the algorithm employed by the MD code to compute the trajectories of the atoms have been described and discussed. In order to obtain trajectories as close to the true trajectories as possible and to keep the computational time small, the time-step has to be selected carefully. The importance of the time-step size for the simulations is explained and the selection criteria are described. The simulations performed to determine an appropriate time-step size are explained and the results are discussed. Finally, the equations used by the MD code to calculate various thermodynamic properties from the computed trajectories are listed.

Chapter 4

Sliding Friction on Copper Asperities: Frictional Analysis

4.1 Background

Understanding the physics of friction is of fundamental importance for a wide range of applications and even more so for small-scale applications. When surfaces in contact slide across each other, the manner in which the contacting asperities interact has a significant influence on the frictional characteristics of the sliding surfaces. Furthermore, the adhesion is directly proportional to the number of atomic or molecular bonds that are broken and formed at the interface of contacting surfaces during sliding [15]. Since the asperities or peaks on rough surfaces occur at multiple scales and may have contact areas with values scaling over many orders of magnitudes, their properties can vary significantly due to scale dependent mechanisms [73]. Therefore the behavior of asperities at the smaller scales may benefit from techniques such as molecular dynamics (MD) to characterize them. Blau [74] has shown that steady-state friction is highly scale dependent and therefore the friction mechanisms should be modeled considering the entire tribo-system rather than a discrete asperity system. Such an exercise to model the scale effects would be extremely productive if carried out using MD, provided the computational resources allow.

Nevertheless, an important aspect of the frictional sliding process between rough surfaces is the interaction between two separate asperities rather than a flat surface and another flat surface or an asperity and a flat surface. The current work studies two

separate spherical asperities, which has surprisingly only been studied a few times using molecular dynamics. In the most similar work, Zhong et al. [75] performed MD simulations of two asperities sliding into each other to study such asperity-asperity interaction. In their work, they modeled a sliding "hard" upper asperity deforming a fixed lower aluminum asperity, which is still very different from the two deformable copper asperities considered in the current work. They studied the effects of a wide range of conditions including sliding velocities, temperatures, and crystal orientations on the wear process. At the micro-scale, several continuum based semi-analytical as well as finite element based models have also been developed for friction between sliding asperities and cover both elastic as well as plastic deformations [51,49,52]. Therefore, in addition, it would be interesting and insightful to see if these models can be compared to MD simulations at the nano-scale. There have also been recent works that blend molecular dynamics and the finite element method, but the current work uses only the MD method [76].

The origin of friction is an extremely complex phenomenon and is an open and growing research field. The existing theories developed for the bulk are not always consistent with material behavior at the molecular scale. The relationship between experimentally measured values of friction to the material properties is still not clear which makes the prediction of friction challenging. The objective of this work is to numerically study the atomistic mechanism of friction and contact deformation using molecular dynamics simulations on the dry sliding contact of nano-scale asperities. The effects of interference δ, relative sliding velocity v, asperity size R, lattice orientation θ, and temperature control, on the friction characteristics are investigated quantitatively and qualitatively. All the simulations were carried out using the MD code LAMMPS [59].

The material selected for this work is copper, which has been increasingly used in nano-engineering where metallic properties are of importance. The higher electrical and thermal conductivity along with low friction makes copper suitable for use in applications

such as MEMS switches [77] or as an additive to enhance the "wear mending" property of a lubricant [78]. Luo et al. [79] fabricated the first thin film z-axis gyroscope with copper, which offered the possibility of designing larger and more complicated system owing to the higher density of copper. Copper thin films have been used as electrical connectors between discrete devices in integrated circuits or MEMS stress sensors [80,81]. The tribological properties of copper at micro/nano scale play an important role in the wire-bonding process used in the interconnection of semiconductors [82]. Besides its application in MEMS, copper is also the nano-material of choice to be incorporated in the friction material used in automotive brake pads for its ductility and high thermal conductivity [83]. Copper nanoparticles have been used as an additive to enhance the tribological properties of lubricants [84,85].

4.2 Methodology

The geometric 3D model used here to represent asperity-asperity sliding contact is shown in Figure 4.1. The model consists of upper and lower sections each having a hemispherical asperity and a rigid base, composed of copper atoms in a fcc lattice structure. The x, y, and z axes are oriented in the [100], [010] and [001] lattice directions respectively. Periodic boundary conditions are imposed along the x- and z-axis so that the atoms can exit one side of the boundary and re-enter the other side. Non-periodic and shrink-wrapped (the extents of the boundary are set so as to include the atoms in that dimension no matter how far they move [59]) boundary conditions are imposed along the y-axis. The size of the model and the number of atoms in the simulation are chosen to obtain a reasonable balance between nano-scale representation and the computational time and power required. Copper asperities of radii 5 nm, 7.5 nm and 10 nm were used in this work and the number of corresponding atoms and system dimensions are given in Table 1.

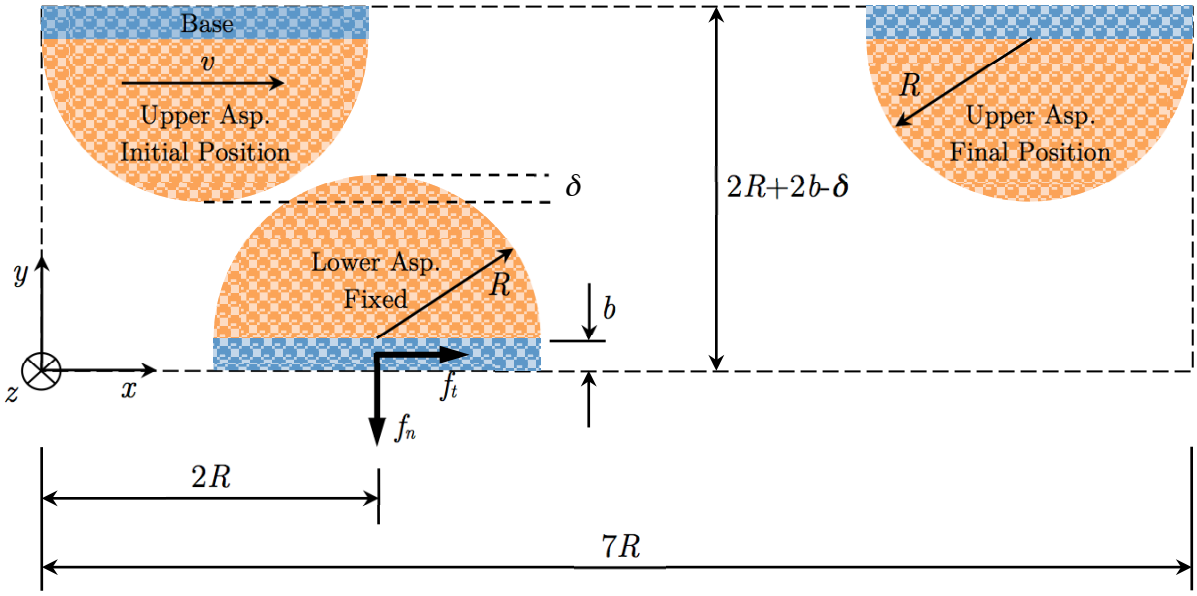

Figure 4.1: Asperity-asperity sliding contact simulation model

Table 4.1: Computation parameters for simulations

	R = 5 nm	R = 7.5 nm	R = 10 nm
b	0.5 nm	0.5 nm	0.5 nm
δ/R	0.10 – (-0.04)	0.10 – (-0.04)	0.10 – (-0.04)
Base Atoms	~ 4,600	~ 10,500	~ 18,400
Asperity Atoms	~ 22,400	~ 75,000	~ 177,000

The atomic interactions were described using the embedded atom method (EAM) given by Foiles et al. [68] provided in the LAMMPS library. In metals, since the valence electrons may be shared between atoms, local electron densities need to be taken into account and the bonds between atoms are not independent of each other. Therefore,

density-independent pair-potentials like the Lennard-Jones (LJ) potential are not always suitable to capture the physics of metallic bonding [68]. It should also be noted that EAM only accounts for the contribution of bound electrons to atomic potentials and not that of the valence electrons. An important difference of the current work compared to that of Zhong et al. [75] is that the latter's work a generic LJ potential was used for the hard (non-deformable) upper asperity and the EAM potential was used for the lower Al asperity.

Newton's equations of motion were numerically integrated using the velocity-Verlet algorithm with a time-step size of 0.002 ps. The MD simulations were performed in two stages on a high-performance computing cluster using between 40 and 80, 2.8 GHz Intel Xeon processors in parallel. First, for each simulation run, the system was initialized and equilibrated at 300 K temperature for 10 ps (5000 time-steps). For the remaining time of the simulation, the temperature control was not enforced anywhere on the system. However, it was found that holding the temperature constant on the base did not significantly influence the effective friction coefficient (as shown in a later section). After the equilibrating cycle, the top asperity was set in motion towards the bottom asperity by imposing an average velocity on the group of atoms in the base region in the x direction. During the asperity interaction, the normal and the tangential reaction forces were monitored on the base regions. These forces were averaged over the sliding distance and an effective friction coefficient was calculated for the distance through which the asperities were in contact, given by

$$F = \frac{1}{N} \sum_{i=n_i}^{n_o} f_i \tag{4.1}$$

$$\mu_{eff} = \frac{F_t}{F_n} \tag{4.2}$$

Here, n_i and n_o are the force values corresponding to the time when the asperities come in contact and get out of contact respectively and N is the number of force values between n_i and n_o. Note that μ_{eff} is not the same as the friction coefficient measured at the macro scale. However, they may correlate if an average is taken for different asperity sizes at different interferences using a method such as the statistical Greenwood and Williamson model for rough surface contact.

4.3 Results and Discussion

4.3.1 Asperity-Asperity Interaction

In order to obtain the sliding motion of the asperities across each other, the atoms in the base region of the upper asperity were imposed with a velocity in the x direction ([100] direction). The lower asperity was held fixed to its position while the position of the upper asperity was set to apply interference with the lower asperity for a range of $0.1R$ to $-0.04R$. The δ/R values of less than zero were included for two reasons: 1) at theoretical zero interference, a positive interference was generated when the system was equilibrated at 300 K as the atoms relaxed and 2) the adhesion was strong enough to pull the atoms to make contact if the two asperity tips were within the attractive range. The simulations were run for a sufficient number of time-steps to ensure that the asperities were completely out of contact. At every time-step, the forces on the atoms in the base regions were summed and recorded to obtain the reaction force components. These values of forces were averaged for the time the asperities remained in contact. A visualization tool was used to note the start and the end of the contact. This was also verified by the values of forces, which averaged to zero before and after the contact.

Figure 4.2 shows the asperities at the start and end of sliding contact for $\delta/R = 0.10$ and $v = 10$ m/s for the asperity of radius 5 nm. In the first part of the sliding process the

upper asperity makes contact with the lower one and a junction is formed. This junction grows through the sliding as more atoms bond to each other and the free surface decreases until the centers of the asperities align. In the second part, this adhered junction starts stretching along the sliding direction as the asperities move apart and finally breaks after necking. Such formation of necking is consistent with the work by Zhong et al. [75]. They report that the neck glides on the Al surface along a favorable slip system and material is transferred from the lower Al tip to the upper LJ tip by adhesion. It can be seen (in Figure 4.2) that in the current work both the asperities undergo severe plastic deformation along with several atoms being transferred from one asperity to the other.

Figure 4.3 shows the friction force through the sliding interaction as a function of the normalized sliding direction. The black line shows the moving average trend line for clarity while the vertical red lines mark the start and end of contact between the asperities. Note: the forces shown throughout this document are the reaction forces on the base of the lower asperity. The value $x/R = 0$ corresponds to the position when the center of the upper asperity align vertically. The friction force which starts from zero, reaches a maximum at approximately $x/R = 0.75$ soon after the asperities align and decreases back to zero as the asperities come out of contact. The first half of the sliding process, where the asperities are compressed, is characterized mostly by the ploughing of atoms while the second half is dominated by adhesion.

The normal force is shown in Figure 4.4. As the asperities come very close to each other, they get pulled into contact, which is shown as the first peak in the normal force (at x/R between -0.75 and -0.50) as the lower asperity gets pulled upwards. As the upper asperity moves on, the normal force starts decreasing as the asperities start compressing and the lower asperity gets pushed down till approximately when the upper and the lower asperities align at $x/R = 0$. It then starts increasing as the asperities pull away from each other and then goes back to zero when the asperities come out of contact. The asperities remain in contact for a much larger distance past $x/R = 0$ due to adhesion.

During the sliding interaction, the atoms are continuously vibrating about their mean lattice position as well as colliding with one another. Therefore, the positions and momenta of these atoms are continuously changing. As a result, the functions (e.g. forces) that depend on the positions and momenta are also fluctuating continuously [57]. The fluctuations seen in the forces can therefore be attributed to the vibratory motion and the frequent collisions of the atoms with one another.

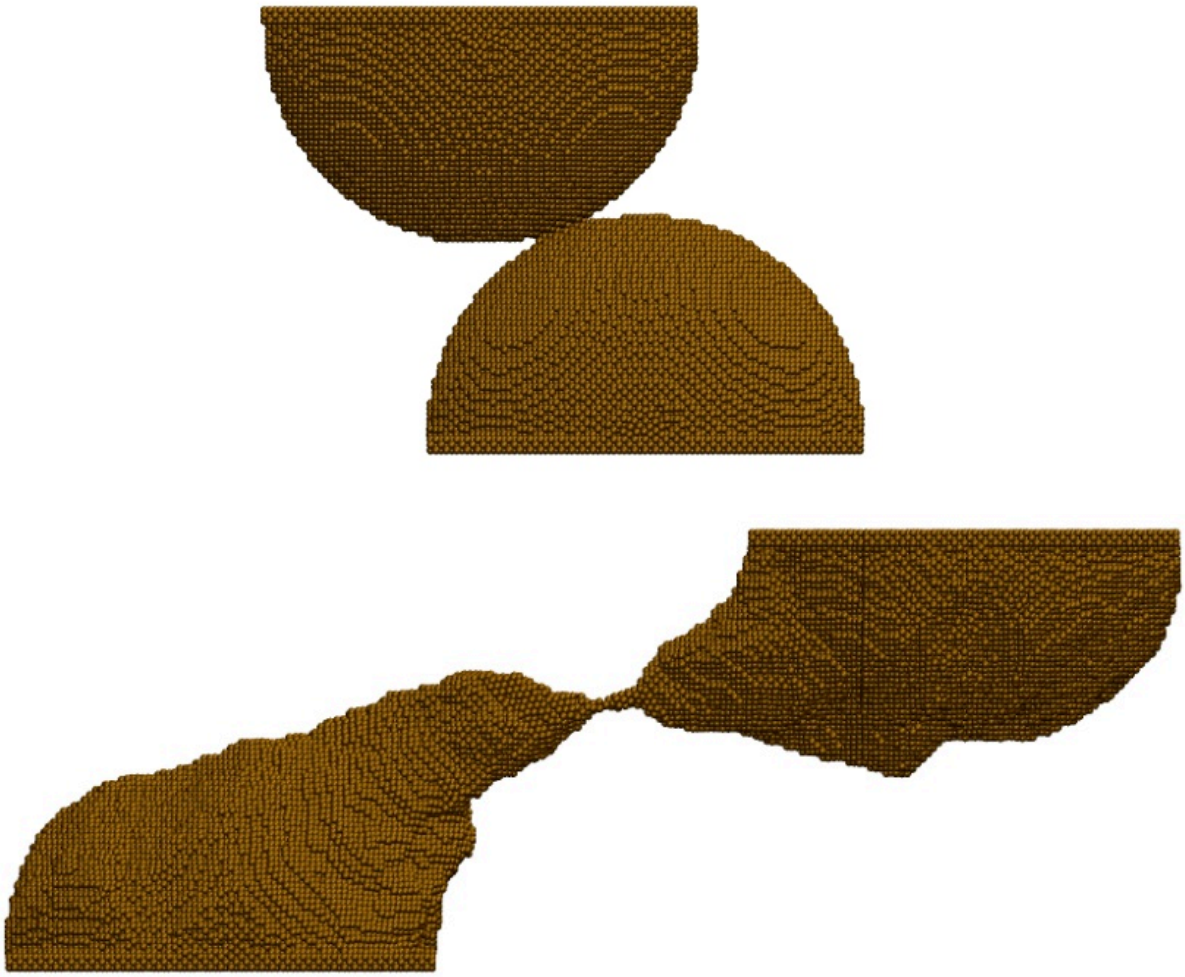

Figure 4.2: Copper asperities before (above) and after (below) sliding process for $R = 7.5$ nm, $v = 10$ m/s, and $\delta/R = 0.1$

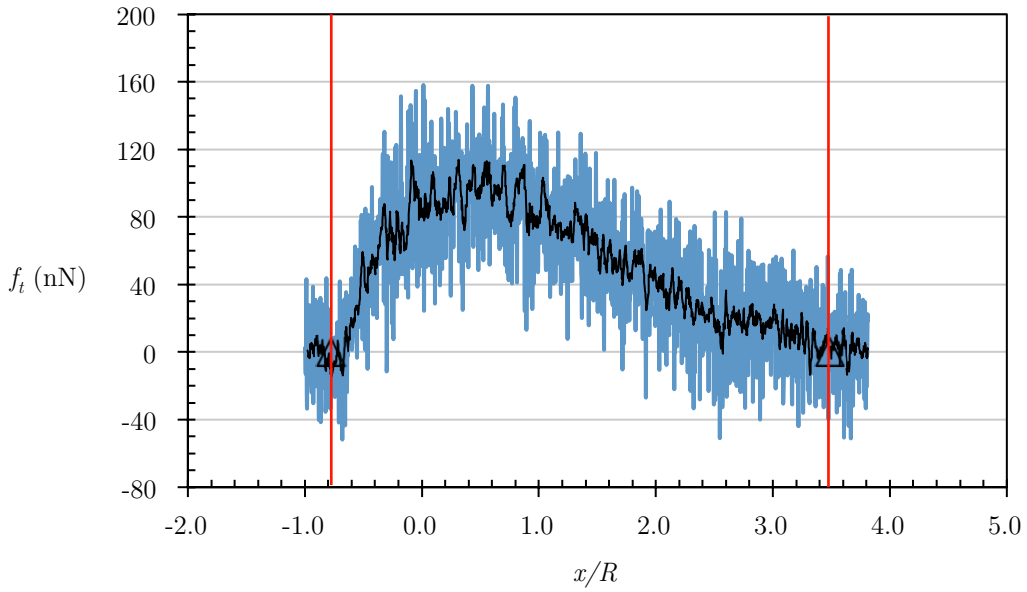

Figure 4.3: The friction force during sliding in normalized sliding direction for $R = 7.5$ nm, $v = 10$ m/s, and $\delta/R = 0.1$. The black line is the moving average trend line and the red lines mark the start and stop of the asperity contact.

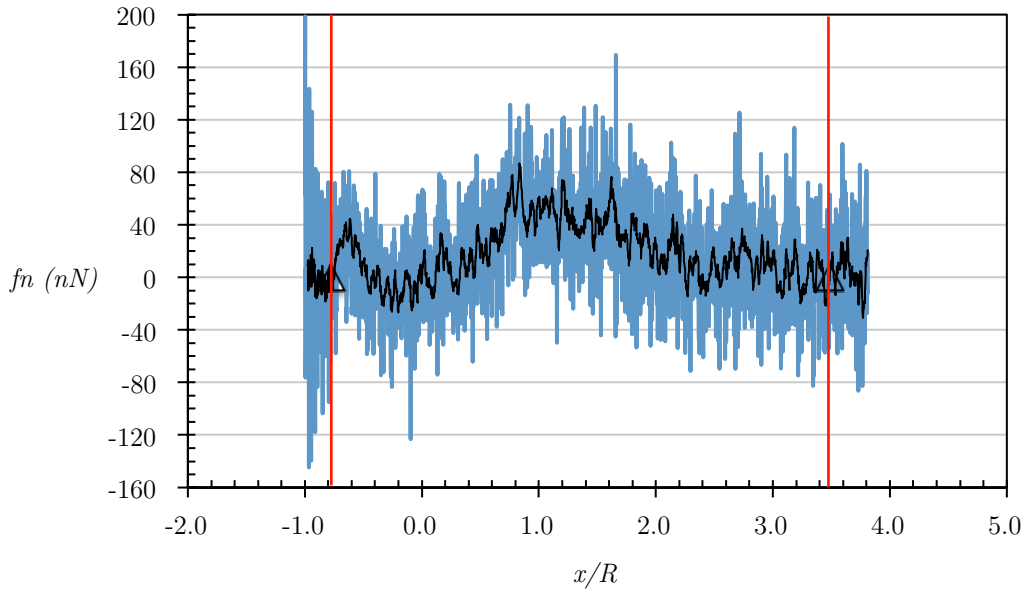

Figure 4.4: The normal force during sliding in normalized sliding direction for $R = 7.5$ nm, $v = 10$ m/s, and $\delta/R = 0.1$

At the micro-scale, the inverse trend has been observed for the friction and the normal forces [51,49]. In the elasto-plastic sliding of micro scale hemispherical asperities without adhesion, it is the friction force that changes direction as the asperities push each other apart at the end of the contact. The normal force does not show this behavior due to the absence of a strong adhesion force. However, here the adhesion was strong enough to pull the atoms of the asperities to make contact even when the interference was negative, i.e. the asperities were separated by a distance of $0.04R$. Such adhesion dominant interactions can lead to unpredicted contacts or larger contact areas than expected between sliding surfaces [17,27,86]. Figure 4.5 and Figure 4.6 show the friction force and the normal force respectively for $\delta/R = 0.00$. It can be seen that even at theoretical zero interference the friction force is not zero due to adhesion, which would not have been the case at the macro-scale. The normal force on the other hand shows only a minor variation as the asperities slide across each other. Figure 4.7 and Figure 4.8 show the friction force and the normal force respectively for $\delta/R = -0.04$. At this value of normalized interference, the force interactions between the asperities get closer to zero on an average and any trend in the values of forces would be undetectable due to the normal fluctuations of the measured values.

4.3.2 Effect of Interference, $\boldsymbol{\delta}$

Figure 4.9 shows the effect of normalized interference (δ/R) on the averaged friction force for all three asperity sizes and relative sliding velocities. Here, the interference, δ is normalized by the asperity radius R. As the interference increases, the number of atoms, which interact with each other, also increases. This causes increased atom displacement as well as adhesion and results in an increased friction force, which is needed to plough through the atoms and also overcome the adhesion. Thus, the average friction force is directly proportional to the interference.

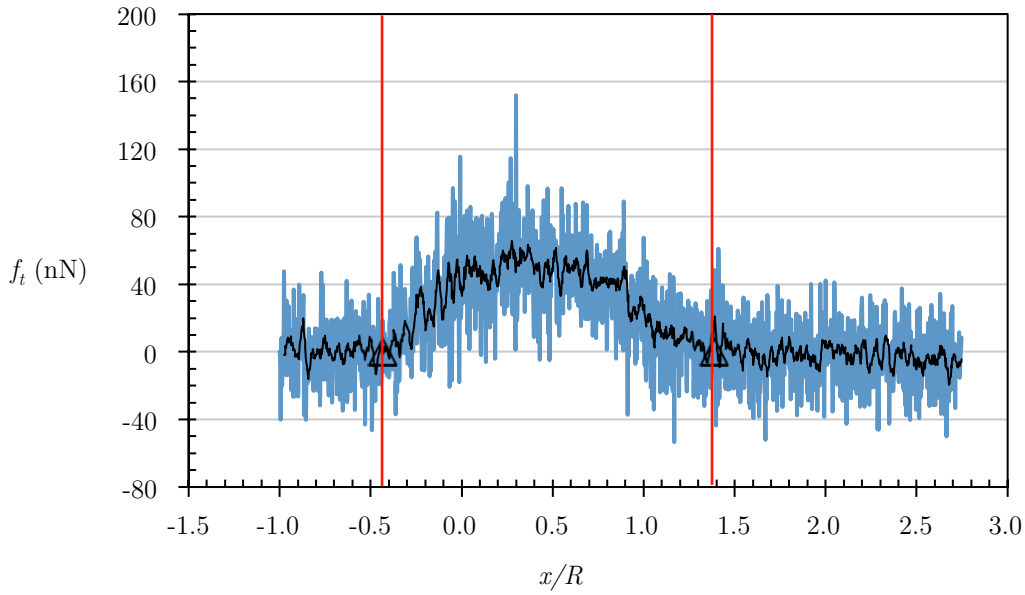

Figure 4.5: The friction force during sliding in normalized sliding direction for $R = 7.5$ nm, $v = 10$ m/s, and $\delta/R = 0$. The black line is the moving average trend line and the red lines mark the start and stop of the asperity contact.

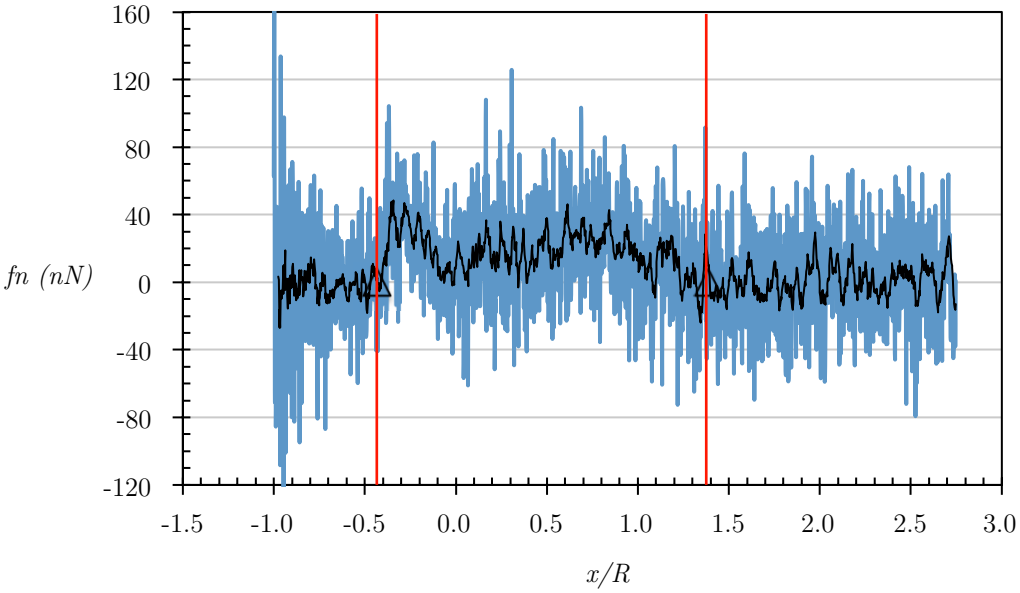

Figure 4.6: The normal force during sliding in normalized sliding direction for $R = 7.5$ nm, $v = 10$ m/s, and $\delta/R = 0$

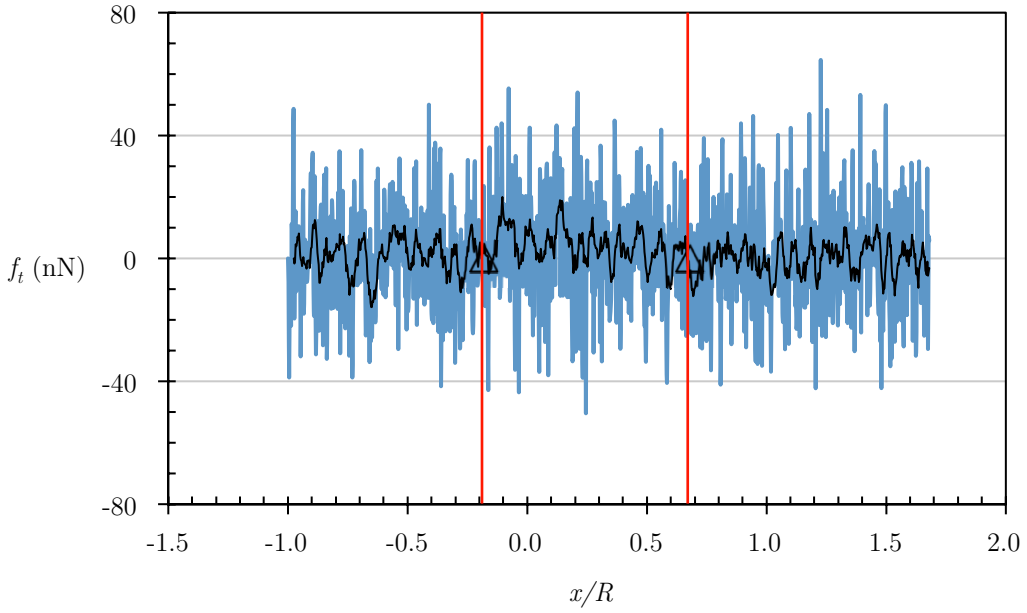

Figure 4.7: The friction force during sliding in normalized sliding direction for $R = 7.5$ nm, $v = 10$ m/s, and δ/R = -0.04. The triangles on the data mark the start and stop of the asperity contact.

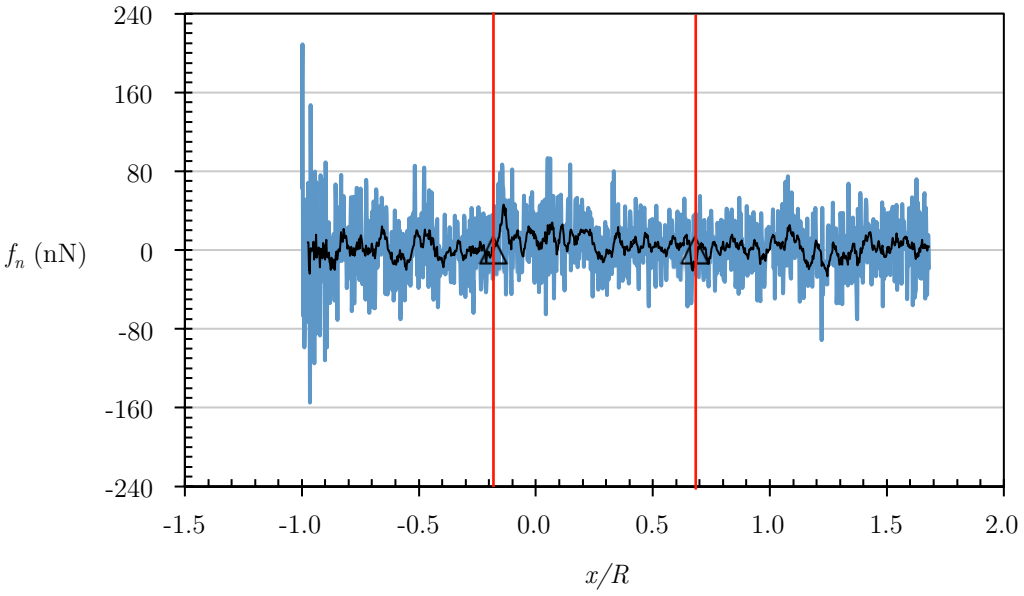

Figure 4.8: The normal force during sliding in normalized sliding direction for $R = 7.5$ nm, $v = 10$ m/s, and δ/R = -0.04

This is not the case with the average normal force (see Figure 4.10). The average normal force, while not showing a definite trend, seems to randomly fluctuate for certain interference values, which are different for each asperity size. This also results in a fluctuation of the effective coefficient of friction with interference (δ/R). The visualizations of the sliding process were analyzed which revealed that this fluctuation was caused due to the vertical alignment of the lattice and the resulting discretization of the smooth surface geometry for a given value of interference. Nevertheless, for all the values of interference, the asperities have the same average continuous geometry. The number of atoms would either increase or decrease slightly depending on the discretization and result in a biased value of the normal force.

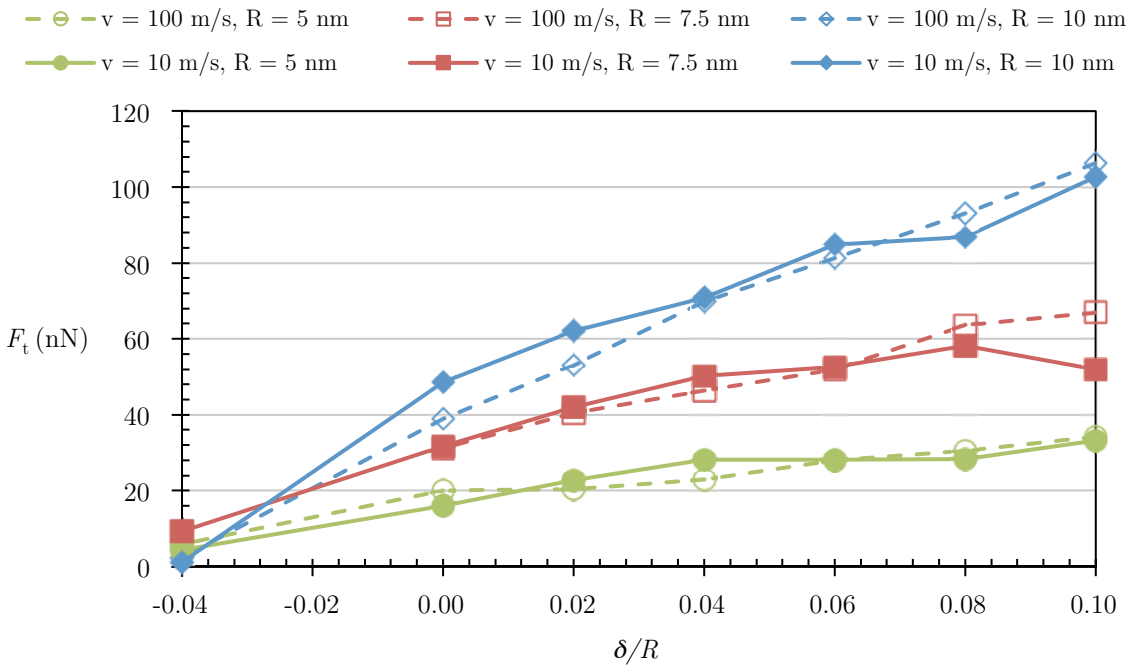

Figure 4.9: The effect of interference, asperity size, and relative sliding velocity on the average friction force

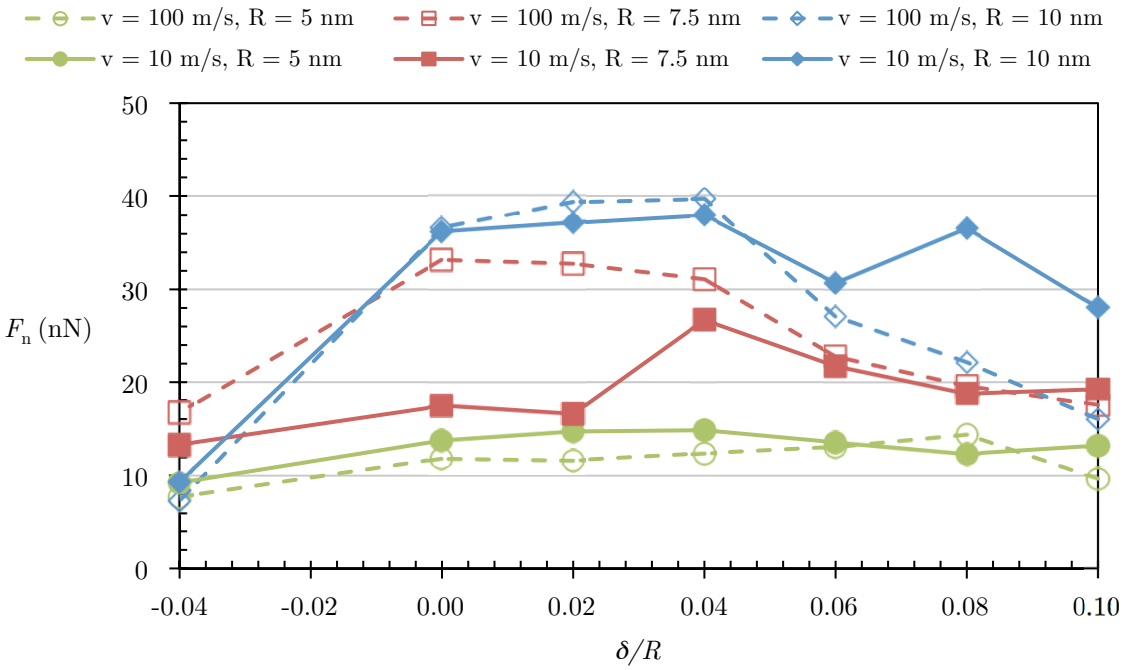

Figure 4.10: The effect of interference, asperity size, and relative sliding velocity on the average normal force

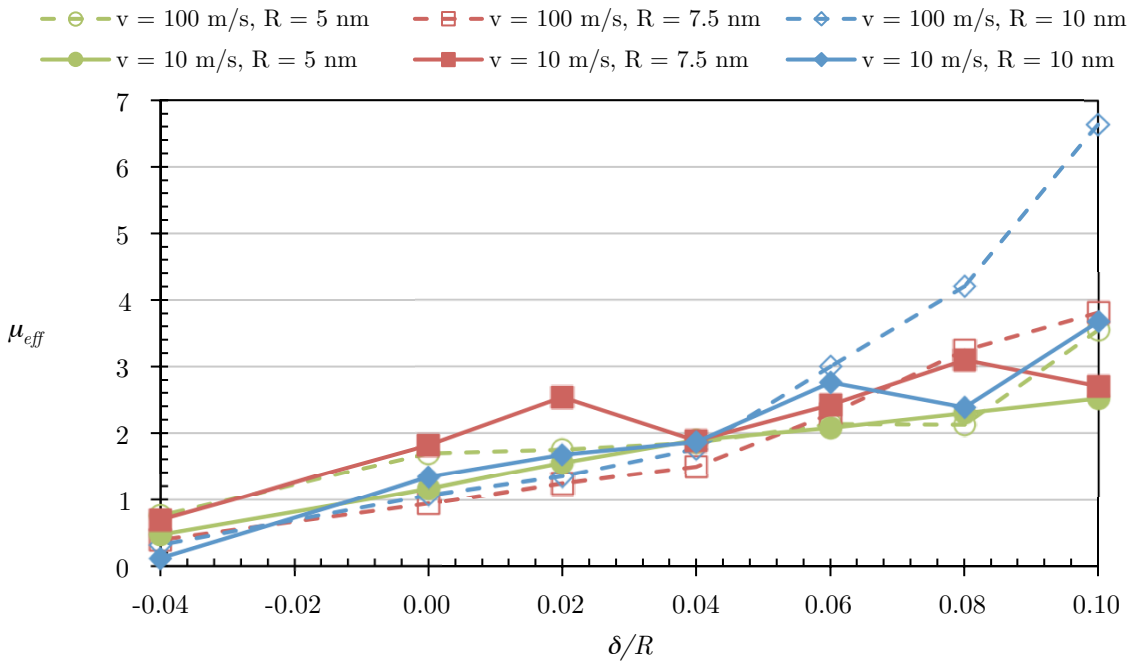

Figure 4.11: The effect of interference, asperity size, and relative sliding velocity on the effective friction coefficient

Similar to the current work, the results in a study of friction in nano-metric scratching of a rigid diamond tool on a copper work-piece [87] show a steeper increase in the friction force as compared to the normal force with increasing scratching depth and friction dominated by adhesion at smaller scratching depths. In this work since the average friction force is rapidly increasing compared to the average normal force, the effective friction coefficient also increases with the interference (see Figure 4.11).

4.3.3 Effect of Asperity Radius, R

To study the effect of asperity size on the forces and effective friction coefficient, asperities with radii of 5 nm, 7.5 nm, and 10 nm were considered. Again, as the asperity size increased, the number of atoms in both of the asperities taking part in the interaction also increased. Note that as the size increases the smoothness of the curvature of the asperity also increases. This further adds to the number of interacting atoms.

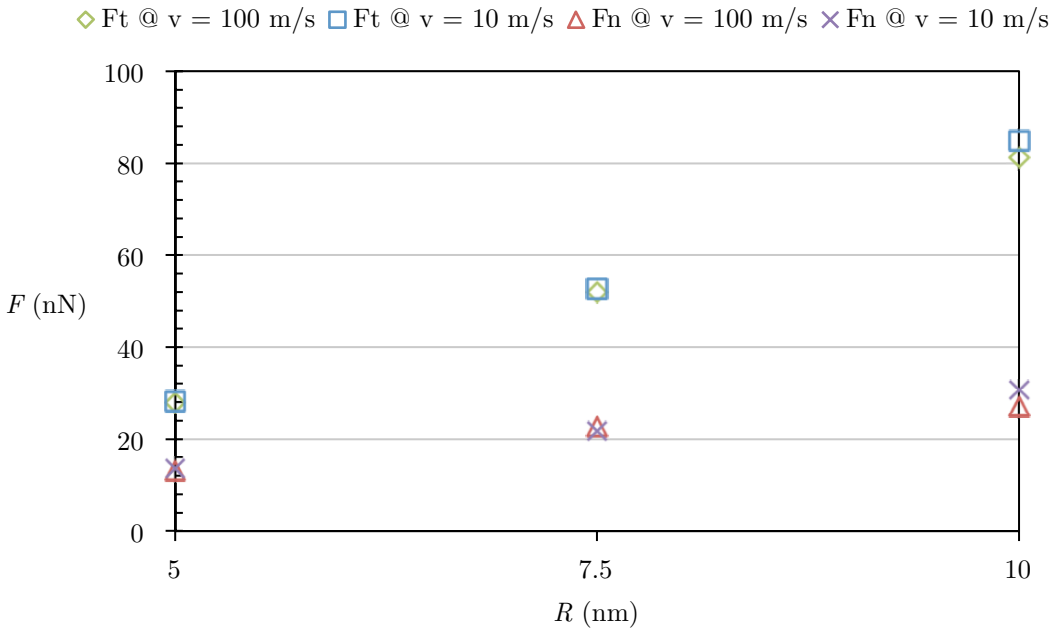

Figure 4.12: The effect of asperity size on the average friction force and the average normal force for $\delta/R = 0.06$

Figure 4.12 shows that the average friction force and the average normal force increase almost linearly with size. The effective coefficient of friction (Figure 4.11) also increases with size since the average friction force increases more rapidly than the average normal force. This was expected and was in agreement to other similar works [86,47].

4.3.4 Effect of Sliding Velocity, v

Two sliding velocities of 10 m/s and 100 m/s were used in this work to quantify its effect on the friction characteristics along with the change in the interference and size. These values of velocity represent the velocities commonly encountered in MEMS/NEMS devices [19,88,12]. For example, a high temperature micro gas turbine has a rotational speed that would translate into a sliding velocity of over 500 m/s [89].

An important observation of this work was that for the sliding velocity of 100 m/s, due to the sudden acceleration of the asperity atoms in the x direction at the start of the simulation, the upper asperity oscillated about its center as it travelled towards and across the lower asperity. This caused the normal force and as a result the friction coefficient to fluctuate severely. To reduce this effect, instead of applying an instantaneous increase in velocity, the atoms were gradually accelerated. A velocity ramping function given by

$$v(t) = tanh\left(\frac{t}{A}\right) \tag{4.3}$$

was used to accelerate the asperity to 100 m/s before the start of the contact and then was maintained at this velocity for the remaining sliding process. Although not evident during the visualization and in the force curves, some of this oscillation might still be present even after the gradual ramping of the velocity as well as for a sliding velocity of 10 m/s for which such a ramping function was not in place. This could also explain the random fluctuation of the average normal force as observed in Figure 4.10, but then one

would also expect the average tangential force to fluctuate and it does not. Therefore, it appears more likely that the previously mentioned lattice alignment effect causes these fluctuations.

As seen in Figure 4.9 - Figure 4.11, the change in the sliding velocity of the asperity did not produce any consistent and significant change in the forces and the effective friction coefficient. This is in contradiction to several reported results on asperity sliding friction [26,19,90]. Karthikeyan et al. [19] have reported a five-fold increase in the friction coefficient when the sliding velocity of copper block on an iron block was increased from 300 m/s to 1000 m/s. It should be noted that this sliding velocity is in a different range than that considered in the current work. In the sliding of a square prismatic diamond tip on a copper surface, the friction force increased as the sliding velocity increased from 10 m/s to 100 m/s while the normal force remained unchanged [26]. However, the main difference between the above mentioned works and the current work is that the sliding surfaces remain in contact for the entire duration and the contact area is also essentially constant throughout the sliding process in those works. In the current work, asperities remain in contact for only a small duration with the contact area is continuously changing. Intuitively, this seems logical since there would be less time for the temperature to rise. In better agreement with the current work, Zhong et al. [75] performed the simulations with sliding velocities of 50, 100, and 400 m/s and found that at 300 K the wear of the aluminum asperity changed very little with respect to the sliding velocity. Although the increased velocity did not have a significant effect on the average forces and the effective friction coefficient, the length for which the asperities remain in contact is much shorter (~32%) for the higher velocity as seen in Figure 4.13 and Figure 4.14. This means that the effect of adhesion was lower for the higher velocity. Furthermore, the peak friction force during the sliding was slightly higher for the higher velocity; however, the normal force does not show a significant change.

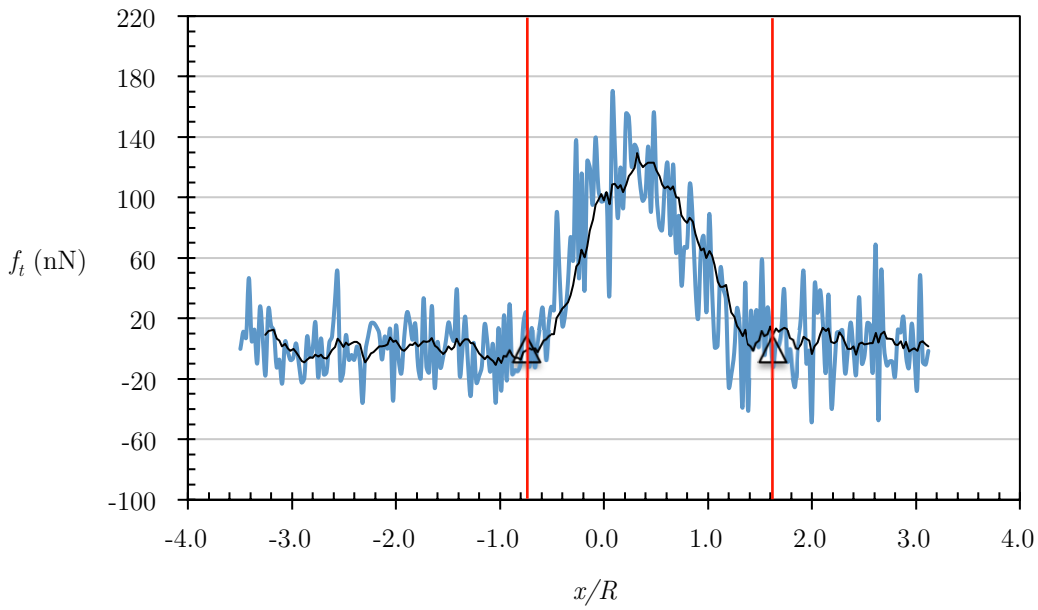

Figure 4.13: The friction force during sliding in normalized sliding direction for $R = 7.5$ nm, $v = 100$ m/s, and $\delta/R = 0.1$. The black line is the moving average trend line and the red lines mark the start and stop of the asperity contact.

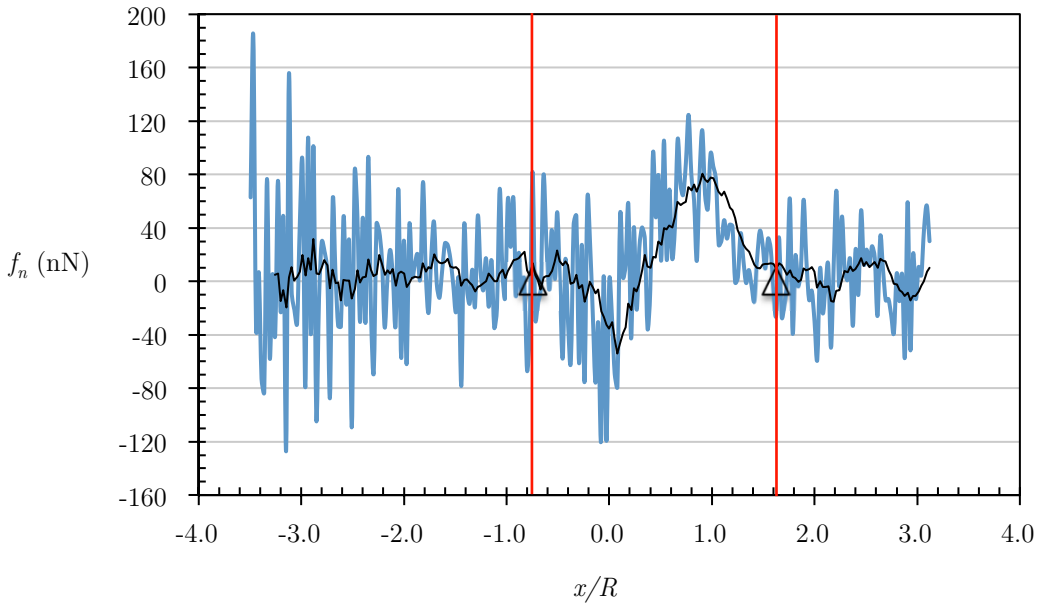

Figure 4.14: The normal force during sliding in normalized sliding direction for $R = 7.5$ nm, $v = 100$ m/s, and $\delta/R = 0.1$

4.3.5 Effect of Time-step size, Δt

As discussed in section 3.3, the time-step size of 0.002 ps, used in all of the simulations, was chosen based on the criterion that it should be sufficiently smaller than the time period of the highest frequency vibrations of the atoms so as to achieve reasonably good trajectories and conserve energy. Again, a larger time-step size is always desired since that will reduce the total time required to run a simulation. A simulation was run using the asperity size of 7.5 nm and a sliding velocity of 10 m/s, with the rest of the parameters unchanged, to investigate whether using a time-step size of 0.005 ps instead of 0.002 ps would have a significant effect on the trajectories and therefore the results. Figure 4.15 and Figure 4.16 show the average friction force and average normal force respectively for both the values of the time-step size. The average friction force does not change significantly with the time-step size except for the normalized interference values of -0.04, 0.08 and 0.10. These values of normalized interference correspond to the least and the most number of atoms of the asperities interacting with each other.

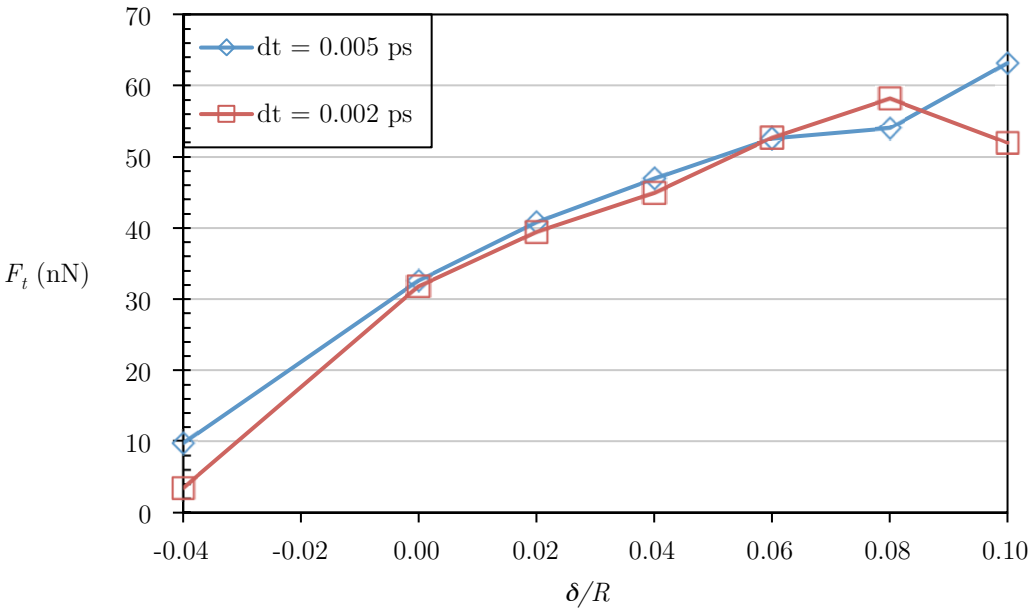

Figure 4.15: The effect of the time-step size on the average friction force

The average normal force, on the other hand, shows a significant variation between both the values of the time-step size for lower values of normalized interference. On an average, it almost stays constant for all the values of normalized interference, which is counter-intuitive. At $\delta/R = -0.04$, the asperities do not come in contact during sliding and only long range attractive forces are present. Such a high value of the average normal force for this value of interference suggests the presence of instability with the 0.005 ps time-step.

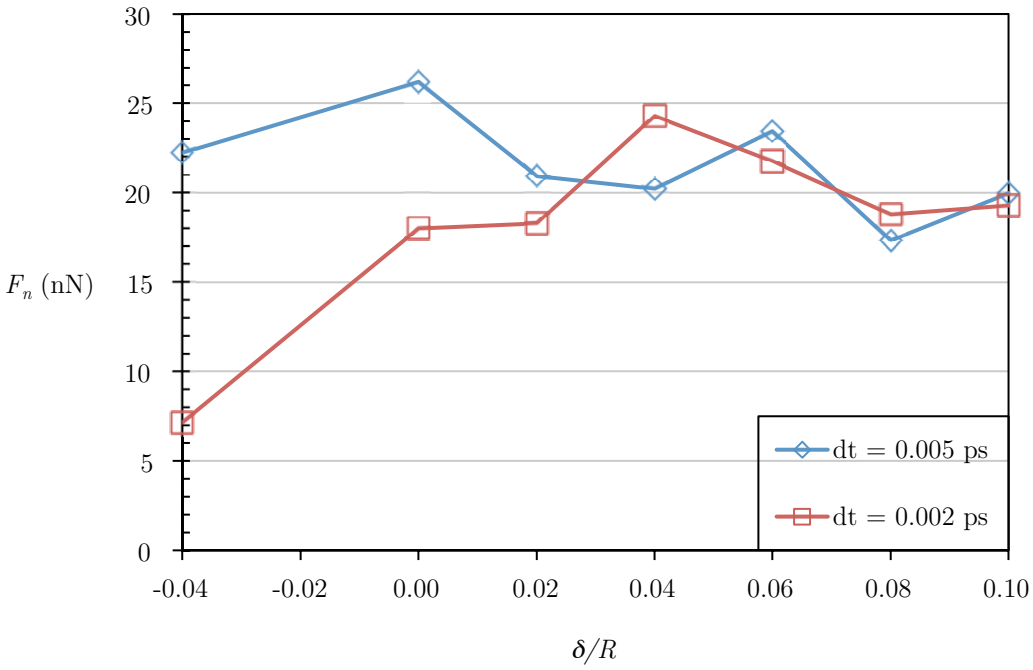

Figure 4.16: The effect of the time-step size on the average normal force

4.3.6 Effect of Lattice Orientation, θ

All of the simulations so far were performed with the x, y and z axis oriented in the [100], [010] and [001] lattice directions respectively, such that the (001) planes were parallel to the sliding direction. The average normal force fluctuation was perhaps caused due the vertical alignment of the lattices and the resulting discretization of the asperity surfaces for certain interference values. If the orientation of the lattice is changed then

this phenomena should disappear. This is demonstrated by performing simulations for various lattice orientations, θ, about the z-axis as listed in Table 2. This is probably a more realistic condition since, in a real surface, the lattices are oriented randomly within the asperities and thus, would average out the orientation bias. The slip planes of both the asperities remained parallel to each other as the lattices were reoriented the same for both asperities.

Table 2: Lattice orientations simulated

xyz direction	$\boldsymbol{\theta}$
[110],[$\bar{1}$10],[001]	45°
[320],[$\bar{1}$30],[001]	34°
[210],[$\bar{1}$20],[001]	27°
[310],[$\bar{1}$30],[001]	18°
[410],[$\bar{1}$40],[001]	14°

As θ increased, the sliding direction appeared more favorable for slip and the average friction force decreased while the average normal force increased. The deformation or the material transfer did not decrease visibly for the range $\theta = 0°$ to $\theta = 34°$. But at $\theta = 45°$, which corresponds to the (110) planes parallel to the sliding direction, the deformation decreased dramatically with much less material transfer as observed in Figure 4.17. Zhong et al. [75] also reported that the wear decreased significantly when the sliding surfaces where parallel to the (111) planes compared to the (100) planes. Further, Sorensen et al. [30] have shown that between a Cu tip and Cu surface, with non-matching surfaces parallel to the (111) plane the wear is minimum. Although, the most favorable case of (111) parallel to the sliding direction is not considered in this work, the results are comparable. However, one should also note that the contact plane actually changes in the

current work due to the curved nature of both surfaces (i.e. at the initial contact the plane between the two surfaces will be sloped, but as the asperities progress further, the slope eventually becomes zero). In most of the other works that are of an asperity against a flat, the contact plane is always parallel to the sliding plane, which may no represent reality.

Similar to the case of $\theta = 0°$, Figure 4.18 shows the friction force for the case of $\theta = 45°$ which starts from zero, reaches a maximum as the asperities align and decreases back to zero as the asperities come out of contact. However, the normal force does not show the same nature in this case (see Figure 4.19). Firstly, the asperities do not get pulled into contact as they come closer and the corresponding jump in the normal force is also not observed. Secondly, the normal force does not decrease as the asperities align at $x/R = 0$ as seen with the $\theta = 0°$ case. This suggests that as the upper asperity slides into the lower asperity, the atoms slip in the slip planes, which are now in a favorable orientation with respect to the sliding direction and therefore the asperities don't get compressed. The normal force then starts increasing as the asperities pull away from each other and then goes back to zero when the asperities come out of contact. The adhesion is comparatively much lower when $\theta = 45°$ to significantly resist the separation of asperities than when $\theta = 0°$.

Figure 4.20 shows the effect of lattice orientation on the effective friction coefficient for the asperity of radius 7.5 nm and a sliding velocity of 10 m/s. As the lattice is rotated about the z-axis from 0° to 45° the average friction force decreases while the average normal force increases and as a result the effective friction coefficient also decreases on average by a factor of about 6. Thus, friction is greatly influenced the lattice orientation within the sliding surfaces as reported by several other researchers.

Bulk metallic surfaces are comprised of grains with random lattice orientations. Furthermore, the lattice orientation within the surface is not always known even with nano-engineered components of MEMS/NEMS devices. If any one particular lattice

orientation data for friction is used then the prediction of friction that is highly dependent on the lattice orientation, will most likely be erroneous. In such a case, calculating an average friction data set, which represents a random lattice orientation of a realistic surface, would be more useful. Therefore, an average effective friction coefficient was calculated and plotted for the interference values considered as shown in Figure 4.21. The average effective friction coefficient was in the range 0.4 – 1.6 for the normalized interference range of 0 – 0.1.

In the MD study of nano-metric scratching of copper with diamond tip, Zhu et al. [87] obtained a friction coefficient value in range 0.85 – 1.05 for 0.16 – 0.5 normalized interference values with a sliding velocity of 200 m/s. These values are within the range obtained in the current work. Similar friction coefficient values were reported by Yang and Komvopoulos [26], Pen et al. [91], and Sun et al. [92]. However, these values do not agree with the work by Mishra et al. [93]. In their MD study of SiC tip on a Cu substrate, they obtained a friction coefficient value in 0.1 – 0.6 range for 0.02 – 0.35 normalized interference values and with a sliding velocity of 50 m/s. They also conducted an experimental study on the same setup with AFM and obtained friction coefficient values in range 0.35 – 0.55. Liu et al. also studied plowing and friction experimentally using SPM and obtained a friction coefficient value in range 0.25 – 3.25. Thus, friction coefficient values have been reported in a broad range.

It should be noted that in all of the above-mentioned works, the sliding tip was either diamond or SiC on a copper substrate. Therefore, adhesion is negligible compared to the copper on copper setup studied in the current work. Besides, the geometric model is that of a block or an asperity on a flat surface rather than an asperity-asperity interaction. In some of the early experiments [94], the values of the friction coefficient of pure polycrystalline bulk copper in a high vacuum were reported to be in the range 0.9 – 1.2. These are in reasonable agreement with the values of 0.4 – 1.6 obtained in the current work. This suggests that friction at the nano-scale is not entirely disconnected from

friction at the macro-scale. As the friction values are averaged over a range of parameters governing the friction mechanisms, the nano-scale values converge to the macro-scale values.

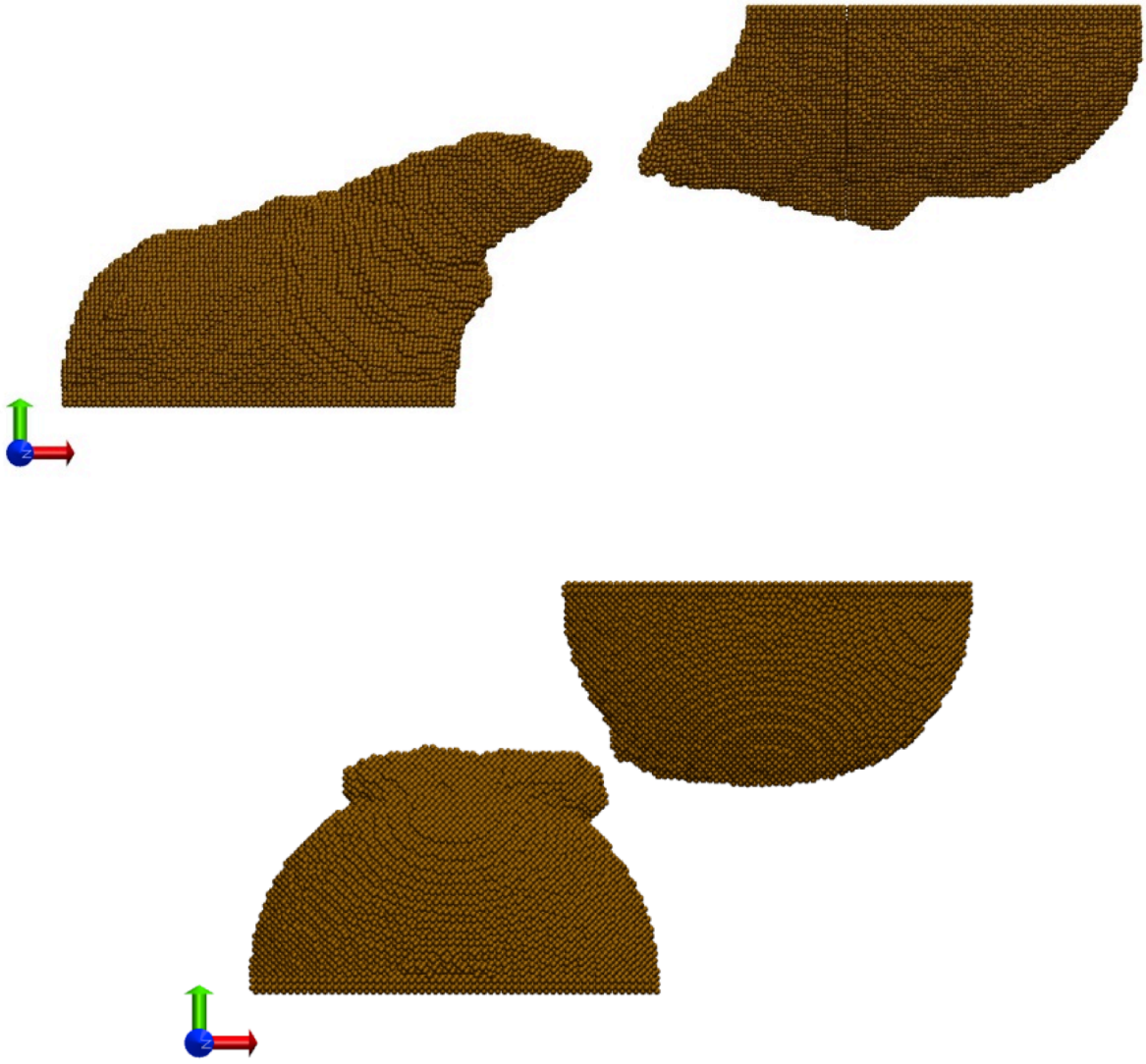

Figure 4.17: Deformation at the end of sliding for $\theta = 0°$ (top), $\theta = 45°$ (bottom) for $R = 7.5$ nm, $v = 10$ m/s, and $\delta/R = 0.1$

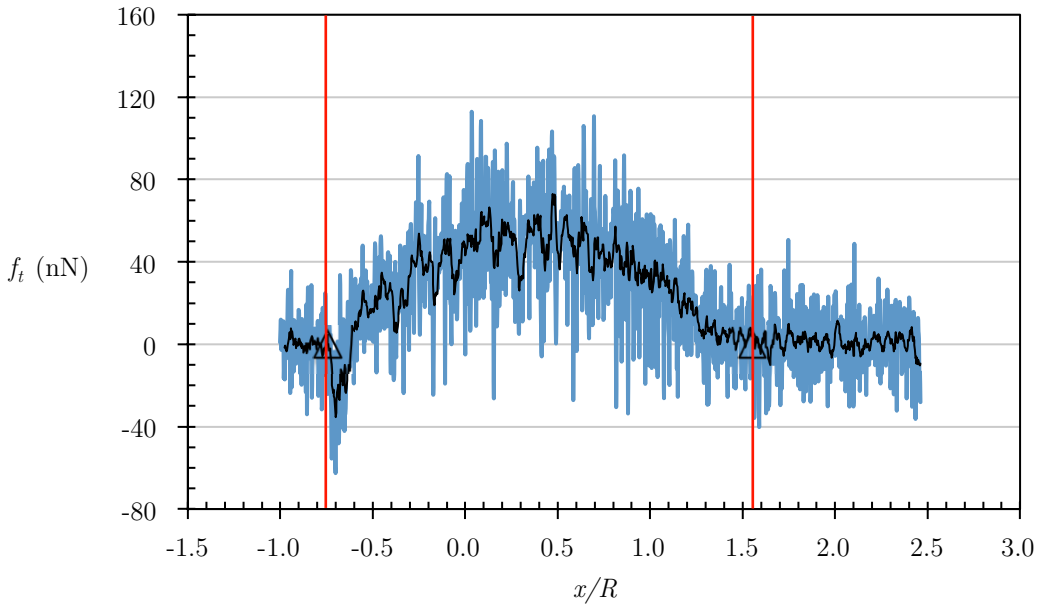

Figure 4.18: The friction force during sliding in normalized sliding direction for $R = 7.5$ nm, $v = 10$ m/s, and $\delta/R = 0.1$ with $\theta = 45°$

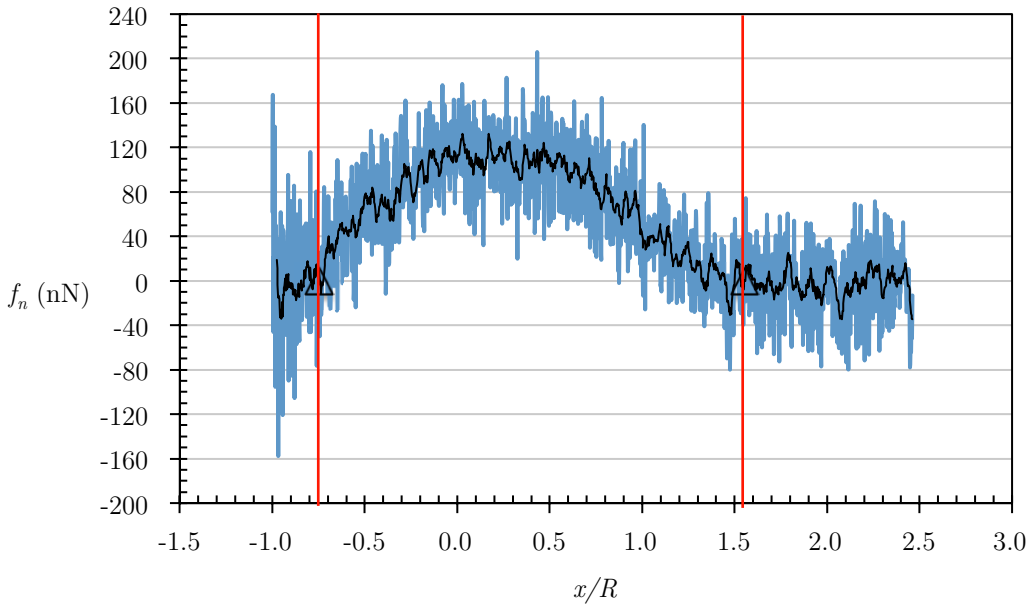

Figure 4.19: The normal force during sliding in normalized sliding direction for $R = 7.5$ nm, $v = 10$ m/s, and $\delta/R = 0.1$ with $\theta = 45°$

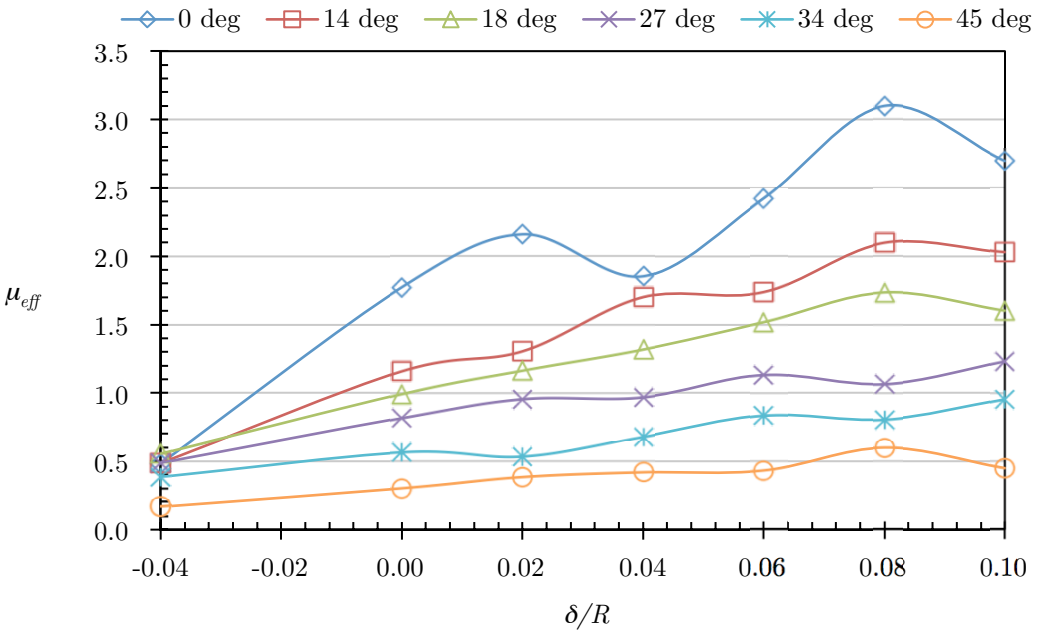

Figure 4.20: The effect of lattice orientation on the effective friction coefficient for $R = 7.5$ nm and $v = 10$ m/s

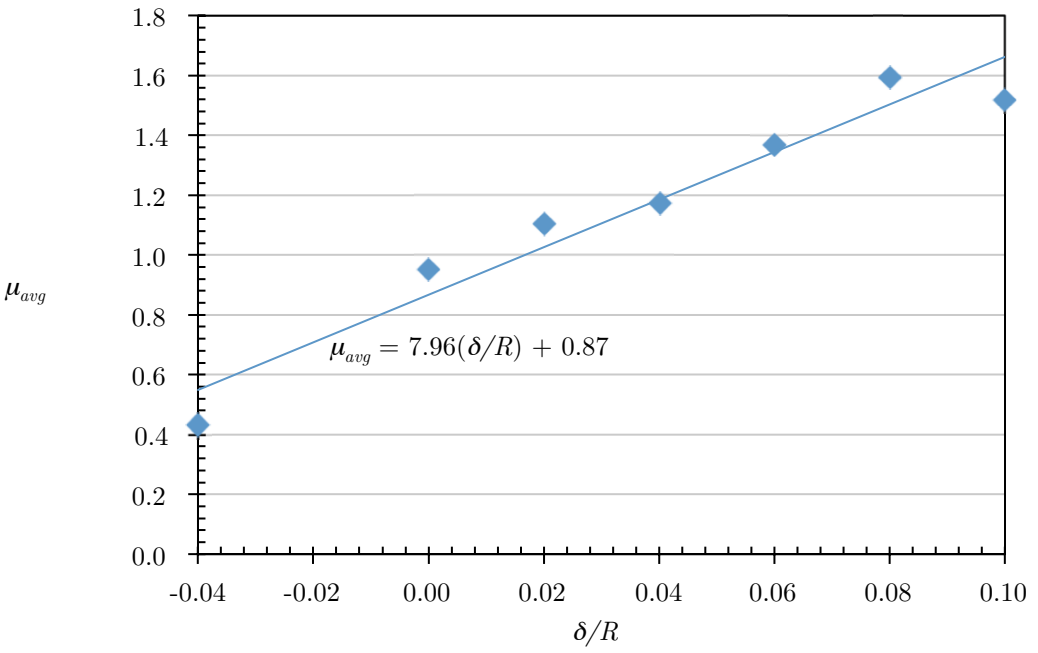

Figure 4.21: The average effective friction coefficient as a function of normalized interference for $R = 7.5$ nm and $v = 10$ m/s, solid line is a linear fit

4.3.7 Effect of Temperature Control

All of the simulations performed up to this point in this work did not have any temperature control or thermostat in place during the sliding interaction, which would drain the energy out of the system. However, most of the previous works in the literature reported in the background section of this report had some sort of thermostat present in their system. Therefore, further simulations were carried out with a temperature control in order to observe its effect on the frictional characteristics. An asperity radius of 7.5 nm with a sliding velocity of 10 m/s was simulated for two different lattice orientations: $\theta = 0°$ and $\theta = 45°$. After the entire system was equilibrated at 300 K, the base regions of both the lower and the upper asperities were held at 300 K by scaling the velocities of the atoms.

Figure 4.22 and Figure 4.23 show the friction force and the normal force respectively during the sliding interaction. The trend and the values of the forces for both the cases, with and without temperature control are nearly identical except that the asperities remain in contact for a slightly shorter length with the temperature control imposed. Therefore, the thermostat did not produce any significant effect on the forces and therefore the effective friction coefficient. Figure 4.24 shows the effective friction coefficient as a function of interference with and without a thermostat. It can be seen that there was little overall change observed by putting a temperature control for both the lattice orientations. Further, it confirms the previous finding of a lower effective friction coefficient at $\theta = 45°$.

The effect of temperature control on the asperity temperature for lattice orientation of $\theta = 0°$ and $\theta = 45°$ is shown in Figure 4.25. When the thermostat was not in place, the asperity temperature increased by approximately 80 K for the case of $\theta = 45°$ as compared to 230 K for $\theta = 0°$ since the work required to slide the asperities across each other is more in the later case. Thus the temperature rise is a function of adhesion and

this finding is in agreement with the work by Ray et al. [95]. Also, the duration for which the asperities remained in contact is also much smaller for $\theta = 45°$ for the same reason. This was also the case when the thermostat was in place, however there was no significant increase in the asperity temperature for either of the orientations.

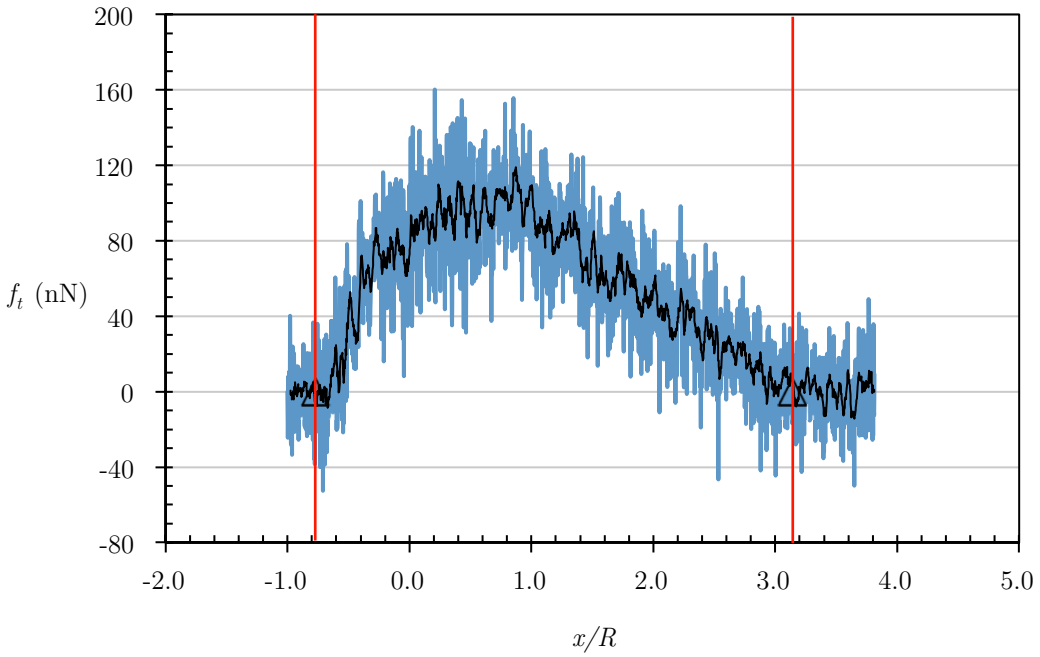

Figure 4.22: The friction force during sliding in normalized sliding direction for $R = 7.5$ nm, $v = 10$ m/s, and $\delta/R = 0.1$ with temperature control. The black line is the moving average trend line and the red lines mark the start and stop of the contact.

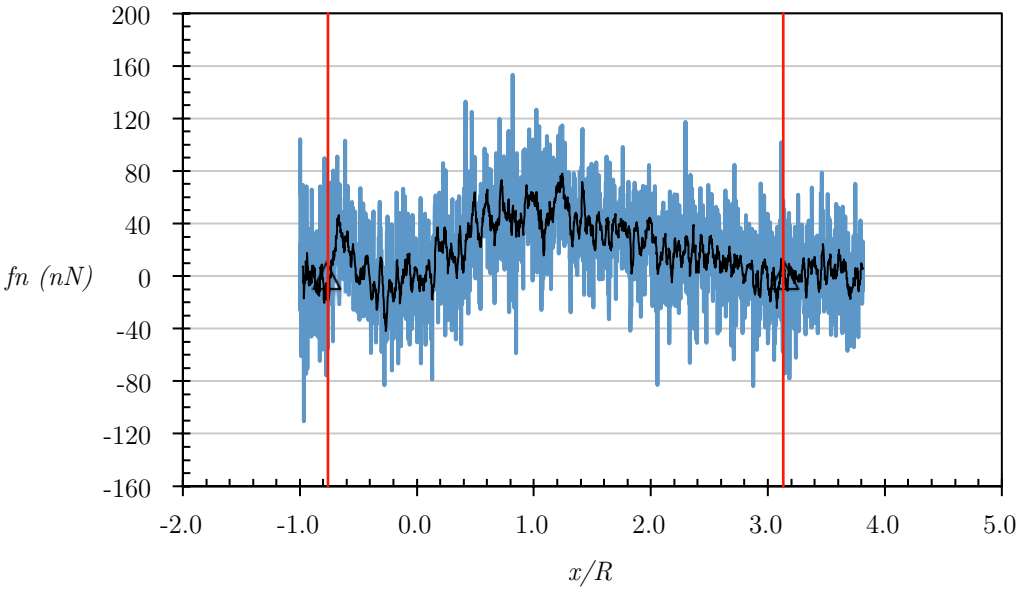

Figure 4.23: The normal force during sliding in normalized sliding direction for $R = 7.5$ nm, $v = 10$ m/s, and $\delta/R = 0.1$ with temperature control

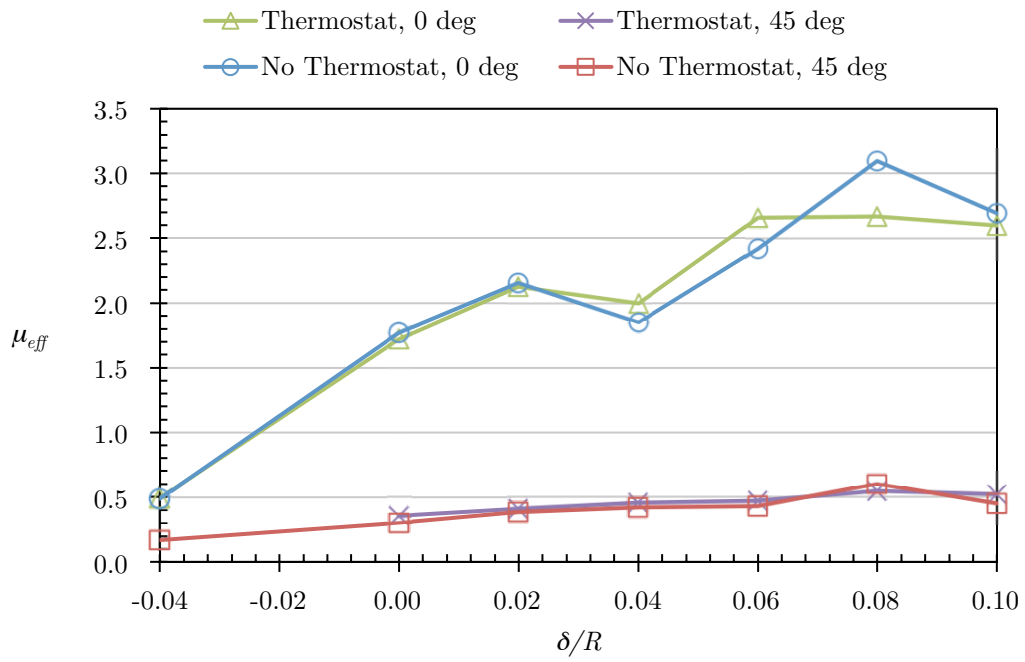

Figure 4.24: The effect of temperature control on the effective friction coefficient for $R = 7.5$ nm and $v = 10$ m/s

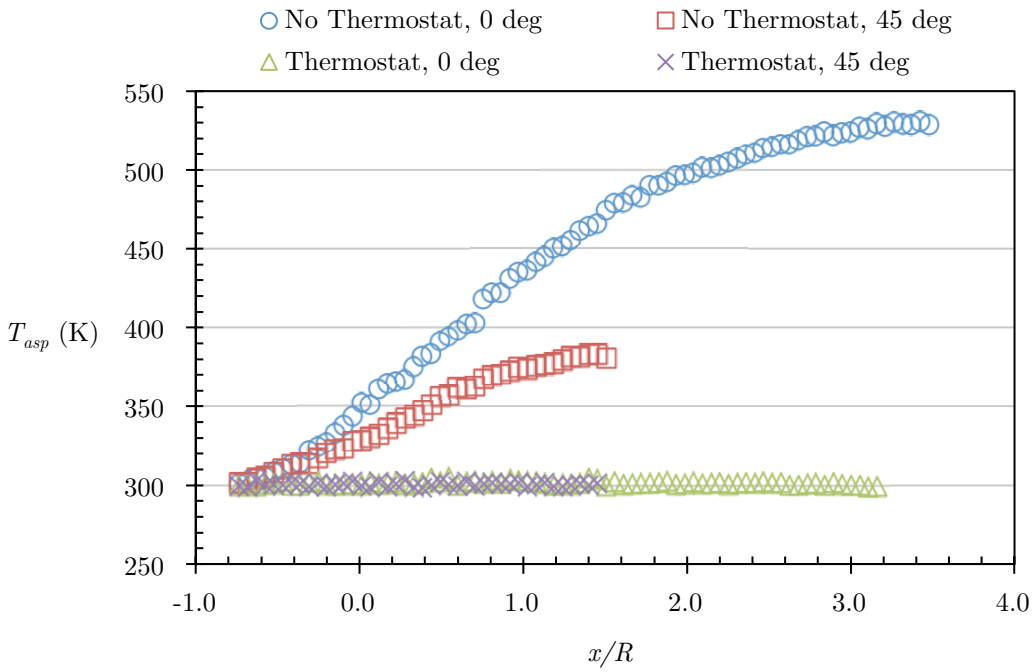

Figure 4.25: The effect of temperature control and lattice orientation on the asperity temperature for $R = 7.5$ nm and $v = 10$ m/s

Electrons and phonons carry out thermal transport in metals, and for pure bulk metals the phononic contribution can be negligible. At the nano scale, the thermal transport decreases due to boundary scattering of electrons and phonons, and size effects [96]. Since the mean free path for electrons is larger than that of phonons, electrons suffer more scattering than phonons and therefore their contribution to thermal transport decreases [97]. Even then the contribution of conducting electrons is crucial in thermal transport. As mentioned earlier, although EAM describes metallic interactions effectively it neglects the contribution of conducting electrons and therefore under-predicts the thermal transport. Consequently, the temperature rise observed as mentioned above is probably over-predicted, and yet its effect is still relatively small on the friction coefficient.

4.4 Conclusions

Molecular dynamics simulations of the dry sliding of copper asperities were performed using the embedded atom potential with LAMMPS. The aim of this work was to study asperity-asperity interaction to gain useful insights on the deformation mechanisms and frictional characteristics in a dry sliding process with a geometry that could be compared and perhaps coupled to continuum models. The effect of interference, asperity size, sliding velocity, lattice orientation and temperature control on sliding friction was investigated. The important findings and conclusions are summarized as follows:

As the asperities come in contact a junction is formed which grew through the sliding as more atoms bonded to each other. This adhered junction stretched along the sliding direction as the asperities moved apart and finally broke after necking. Extensive deformation and material transfer was observed for most of the cases that were studied. Adhesion dictated the sliding process as opposed to ploughing resulting in higher values of effective friction coefficient, which is consistent with literature.

The average friction force and the effective friction coefficient increased with the interference whereas the average friction force, average normal force, and effective friction coefficient increased with the asperity size. This is attributed to the increase in the number of interacting atoms. Fluctuations in the average normal force were observed due to the vertical lattice alignment and the resulting discretization of the smooth surface geometry for a given value of interference.

For the range of 10 m/s to 100 m/s, the velocity presented no significant change in the friction characteristics as the duration of contact was not long enough to realize its effect. However, higher velocity reduced the adhesion effect between the asperities and therefore they remained in contact for a shorter length of the sliding distance.

Lattice orientation presented a significant influence on the frictional characteristics with a reduction in the effective friction coefficient by a factor of about six for the range of orientation considered. For the case when the sliding direction was parallel to the (101) plane, the least material transfer and deformation were observed. Furthermore, lattice alignment or misalignment of the sliding surfaces greatly affects the friction characteristic.

Using a temperature control during the sliding with the base of the asperities at 300 K produced almost no change in the friction characteristics in comparison to no temperature control.

Chapter 5

Sliding Friction on Copper Asperities: Energy Analysis

In the process of sliding friction, energy is 'consumed' or work is required to overcome friction between the sliding surfaces. This imparted energy is converted to thermal energy and deformation energy (elastic and plastic). In this work, the sliding surfaces are the asperities and the energy added to the system to slide one asperity past the other gets converted in part to the kinetic energy of the system and by extension, to thermal energy. The remaining gets converted to the potential energy of the system, which in effect is the deformation energy. It is important to know quantitatively the energy distribution between these two forms to understand the atomistic origins of friction. Furthermore, the ratio of the contributions of each energy type gives deeper insight into the deformation mechanisms of surfaces as well as efficiencies of sliding systems. In the following sections, the method used to quantify each energy type is described and the resulting analyses based on the previous cases described earlier are presented.

5.1 Total Energy

In this work the simulations are performed using the NVE ensemble. The boundaries are periodic in the x and z directions and non-periodic in the y direction. Along the x and z directions, any atom that leaves one boundary, re-enters from the corresponding opposite boundary. The boundaries in the y direction are fixed and therefore atoms cannot leave the system through the y direction boundaries. Therefore, the number of

atoms in the system remains constant throughout the simulation. The system boundaries are also adiabatic; that is a thermostat is not used to control the temperature of the system. As a result, the frictional work done should increase the total energy of the system by the energy conservation principle.

As the upper asperity collides against the lower asperity, some of the atoms are displaced permanently from their original lattice positions to new positions, where the original atomic bonds are broken and new ones are formed. While some of the atoms are not displaced sufficient enough to break the bond and therefore snap back to their original lattice positions after the contact is over. The former case will manifest as a change in the potential energy and for the current work this will be defined as deformation. The latter case will result in a change in the kinetic energy of the atoms and therefore the thermal energy of the system. (It should once again be emphasized that due to the limitation of EAM in taking into account the contribution of valence electrons, only phononic vibrations will be accountable for the thermal conduction.) Therefore, the total energy change or the work done on the system can be bifurcated into the energy consumed in causing deformation and the energy lost through thermal energy dissipation, given by

$$E = E_p + E_k \tag{5.1}$$

5.1.1 Potential Energy

In MD, the interactions between atoms or particles in any system are defined by the intermolecular potential function, which is empirically derived from quantum mechanics and available a priori. The potential function used in this work is EAM and the total potential energy of the ensemble therefore is given by,

$$E_p = \sum_{i=1}^{N} G_i \left[\sum_{j \neq i}^{N} \rho_j(r_{ij}) \right] + \frac{1}{2} \sum_{i,j \neq i}^{N} u_{ij}(r_{ij}) \tag{5.2}$$

The values for G, U, and ρ are provided for specific values of distance and electron density spacing in LAMMPS.

At the start of every simulation, the system was allowed to stabilize and achieve equilibrium. At this stage the system would have a certain potential energy depending on the atomic arrangement at that instance. Any change in this arrangement and therefore the physical structure of the system will cause a change in the potential energy. As the asperities interact with each other, some of the atoms move to a new location and the structure of the asperities change, which is termed deformation in this work. The system gets a new atomic arrangement and therefore a new potential energy value. Once again the system is allowed to stabilize at the end of sliding. The difference between the potential energies at the start of sliding and at the end of sliding will thus give the total change in the potential energy of the system.

$$\Delta E_p = E_p(t) + E_p(0) \tag{5.3}$$

The change in the atomic arrangement however does not entirely occur due to physical interaction; part of it is due to the increase in the kinetic energy or the temperature of the system. As the temperature increases, the average distance between the atoms increases and consequently the potential energy of the system also does. Therefore, the potential energy change now consists of two contributions; one from the temperature change and second from the physical sliding interaction of the asperities and will be given as

$$\Delta E_p = \Delta E_{p,therm} + \Delta E_{p,def} \tag{5.4}$$

where, $\Delta E_{p,therm}$ is the contribution from the temperature change and is termed *thermal potential energy* and $\Delta E_{p,def}$ is the contribution from the deformation of asperities and is termed *deformation potential energy*.

In order to obtain the thermal potential energy, a set of simulations were run, one for each asperity size, in which the system was initialized at 0 K and then was subsequently allowed to stabilize at different higher temperatures without draining energy from the system. The sliding motion was also switched off so as to prevent the interaction of the asperities and to isolate the potential energy change solely due to a system temperature change. Equation (5.5) then gives the energy consumed in causing dislocation of the atoms from its original positions or in other words, deformation of the asperities.

$$\Delta E_{p,def} = \Delta E_p - \Delta E_{p,therm} \tag{5.5}$$

5.1.2 Kinetic Energy

The kinetic energy of the system with N atoms (or particles) is the sum of individual atom velocities and is given by

$$E_k = \frac{m}{2} \sum_{i=1}^{N} v_i^2 \tag{5.6}$$

Here m is the mass of the atom and v_i is the velocity vector.

The upper asperity is sliding in the x direction with a finite and constant velocity and some kinetic energy is associated with this motion, which is called the *translational kinetic energy*. In addition, the atoms are vibrating about their mean lattice position corresponding to the local temperature and the kinetic energy associated with this vibrational motion is called the *thermal kinetic energy*. The translational kinetic energy does not influence the total internal energy of the system since the translational motion by itself neither increases the temperature of the system nor dislocates the atoms to cause

deformation. Therefore it does not need to be considered in the frictional energy balance and henceforth in this work the thermal kinetic energy will be referred to as kinetic energy.

As the asperities interact, the velocities of the atoms about its mean lattice position increases as the temperature increases and this increases the kinetic energy of the system. The difference between the kinetic energies at the start of sliding and at the end of sliding will thus give the total change in the kinetic energy of the system.

$$\Delta E_k = E_k(t) + E_k(0) \tag{5.7}$$

5.1.3 Temperature

The thermodynamic temperature of the system arises from the kinetic energy of the vibrational motion of its atoms and is defined by the relation

$$E_k = \frac{3}{2} N k_B T \tag{5.8}$$

In the absence of degrees of freedom within the atoms, the thermodynamic temperature is identical to the kinetic temperature.

Therefore equations (5.6) and (5.8) give,

$$T = \frac{1}{3} \frac{m}{N k_B} \sum_{i=1}^{N} v_i^2 \tag{5.9}$$

LAMMPS uses equations (5.1) through (5.5) to calculate the respective quantities and each of these could be taken as a simulation output. For the current work however, only the total energy and the temperature were taken as outputs whereas the potential and the kinetic energies were calculated afterward.

5.2 Work

The only work done in the MD simulation is sliding the upper asperity past the lower asperity with a finite interference. This frictional work can be defined using mechanics as

$$W = \int_{in}^{out} f_t dx \tag{5.10}$$

Here the tangential force, f_t, in the direction of sliding is taken over the sliding distance during which the asperities remain in contact. Therefore, the change in the total energy of the system due to sliding of the asperities should equal to the work done on the system and the following relation should hold true for the simulation.

$$\Delta E = \Delta E_p + \Delta E_k = W \tag{5.11}$$

5.3 Results and Discussion

During the sliding of the copper asperities across each other, the temperature and the total energy of the system were taken as one of the outputs from LAMMPS. The total energy change results from LAMMPS were cross checked using equations (5.10) and (5.11) and the values matched with a relative error of less than 1% for all the cases that were run except for two: for $\delta/R = -0.04$ and $\theta = 45°$. For the cases when $\delta/R = -0.04$, the surface atoms on the two asperities were pulled towards each other due to long range attractive forces as the asperities got closer. As a result, the deformation was less and therefore the change in energy was small. This made it hard to determine the exact positions between which the asperities interacted and this lead to an error in calculating the work. The relative error for these cases was in the range of 1.8% - 40%. As seen previously, for the case when $\theta = 45°$, the friction force as well as the deformation was

lowest for respective interference values and therefore the former justification applies here as well. The relative error for this case was in the range of 1% - 3.2%.

The results from the simulations performed to isolate the thermal potential energy component of the total potential energy are shown in Figure 5.1 - Figure 5.4. The system was initiated at 0 K and was stabilized at several higher temperature values. A second order polynomial is fitted to the data. The corresponding equations of the thermal potential energy as a function of temperature for all the asperity sizes are given below.

$$R = 5\ nm: \quad E_{p,therm} = 0.0014T^2 + 6.665T - 186184 \tag{5.12}$$

$$R = 7.5\ nm: \quad E_{p,therm} = 0.0041T^2 + 20.96T - 592889 \tag{5.13}$$

$$R = 10\ nm: \quad E_{p,therm} = 0.00146T^2 + 43.579T - 1356082 \tag{5.14}$$

$$R = 7.5\ nm, \theta = 14^\circ: \quad E_{p,therm} = 0.0042T^2 + 20.513T - 585588 \tag{5.15}$$

$$R = 7.5\ nm, \theta = 18^\circ: \quad E_{p,therm} = 0.0041T^2 + 20.584T - 584873 \tag{5.16}$$

$$R = 7.5\ nm, \theta = 27^\circ: \quad E_{p,therm} = 0.0039T^2 + 20.5846T - 587091 \tag{5.17}$$

$$R = 7.5\ nm, \theta = 34^\circ: \quad E_{p,therm} = 0.0041T^2 + 20.62T - 586617 \tag{5.18}$$

$$R = 7.5\ nm, \theta = 45^\circ: \quad E_{p,therm} = 0.004T^2 + 20.724T - 590393 \tag{5.19}$$

The values from these relations were used to subtract the thermal potential energy from the total potential energy to obtain the deformation potential energy as per equation.

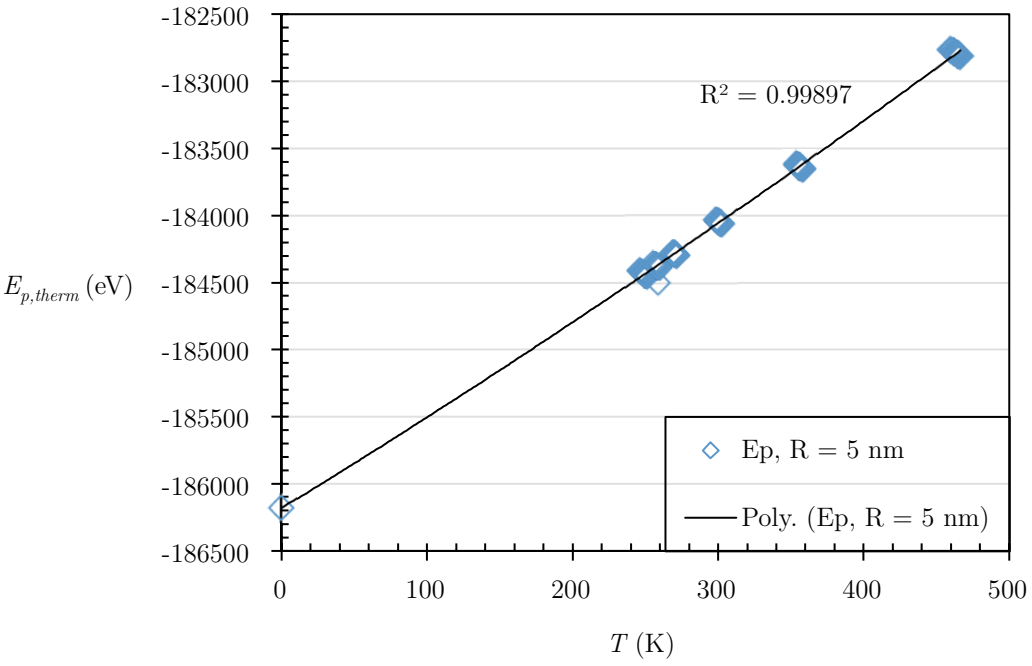

Figure 5.1: Effect of temperature on the thermal potential energy for $R = 5$ nm, no sliding

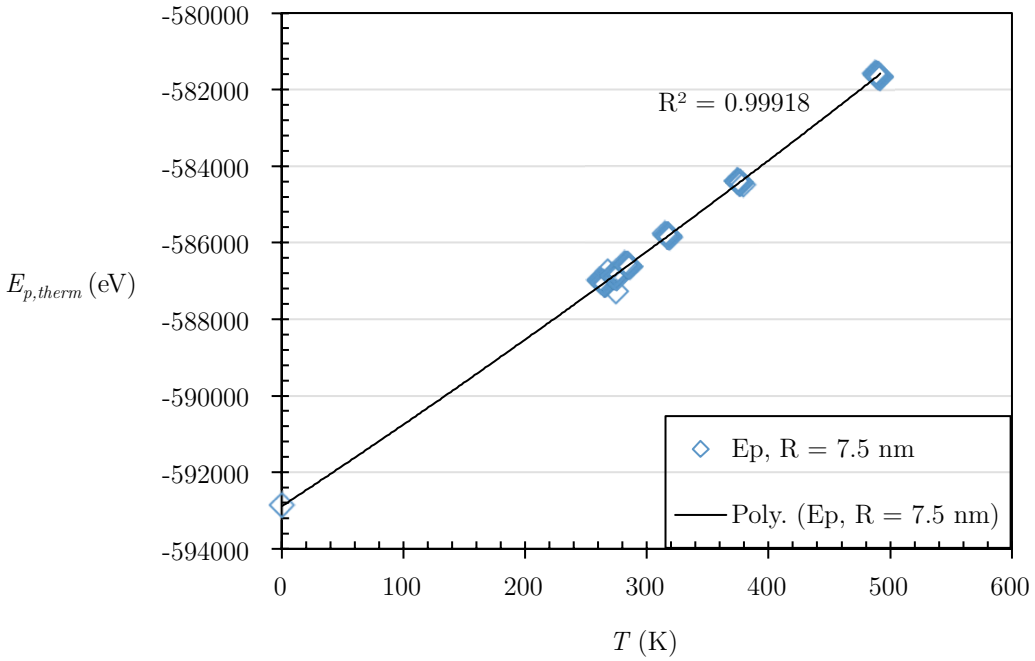

Figure 5.2: Effect of temperature on the thermal potential energy for $R = 7.5$ nm, no sliding

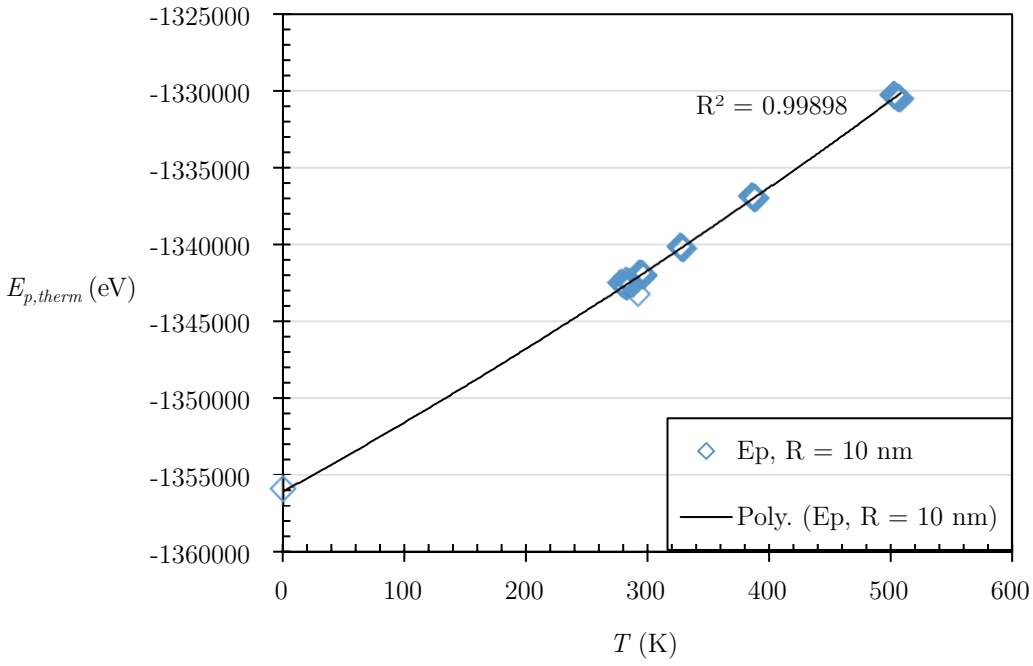

Figure 5.3: Effect of temperature on the thermal potential energy for $R = 10$ nm, no sliding

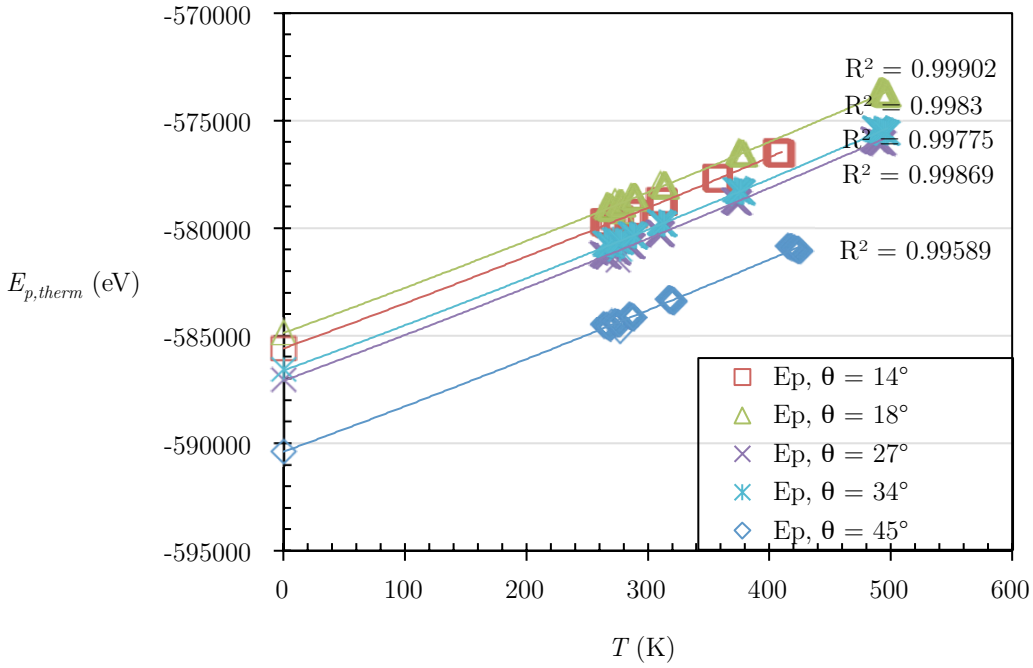

Figure 5.4: Effect of temperature on the thermal potential energy for $R = 7.5$ nm, for all lattice orientation values, no sliding. Solid lines are a polynomial fit.

5.3.1 Effect of Interference, δ

Figure 5.5 – Figure 5.7 show the change in all the energies and the frictional work done during the sliding interaction for normalized interference values of 0.10, 0.00, and -0.04, respectively. As the upper asperity slides across the lower asperity these values keep increasing for the duration the asperities remain in contact. The frictional work done is equal to the sum of the change in the kinetic energy, the thermal potential energy, and the deformation potential energy. It can be seen that the changes in the thermal potential energy and the kinetic energy are fairly close and together they constitute a majority of the frictional work. This result is also consistent with varying normalized interference. An interesting observation here is that right after the asperities come in contact, the change in the deformation potential energy becomes negative and remains so till the asperities align vertically ($x/R = 0.0$). Beyond this point, it becomes positive and keeps increasing as long as the asperities remain in contact. This means that in the first part of the sliding interaction the atoms move to positions, which reduce the potential energy of the system, or in other words the atoms get rearranged to more favorable positions.

For $\delta/R = -0.04$ the frictional work is not zero even though the asperities do not actually come in contact due to the long range interactions. However, the changes in the energies show severe fluctuations and the data is therefore not useful or reliable. It is for this reason that the results for $\delta/R = -0.04$ have been omitted from the discussions for the energy analysis. Figure 5.8 shows the amount of work done to slide the upper asperity past the lower asperity during a simulation run for a sliding velocity of 10 m/s for all the values of interferences (normalized by the asperity radius) considered in this work. As the interference increases, the work done on the system also increases and this result is consistent with all three asperity sizes as well as for the case when sliding velocity was 100 m/s as shown in Figure 5.9. The result is logical since the increase in the interference

increases the volume of the asperities coming in contact and therefore the number of interacting atoms.

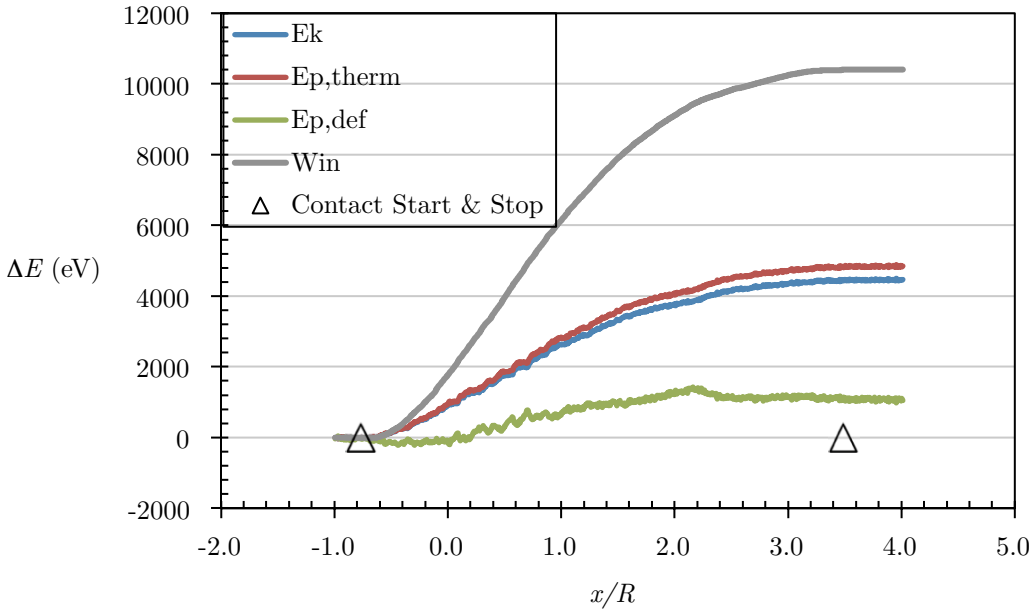

Figure 5.5: The energy change during sliding for $R = 7.5$ nm, $v = 10$ m/s and $\delta/R = 0.1$

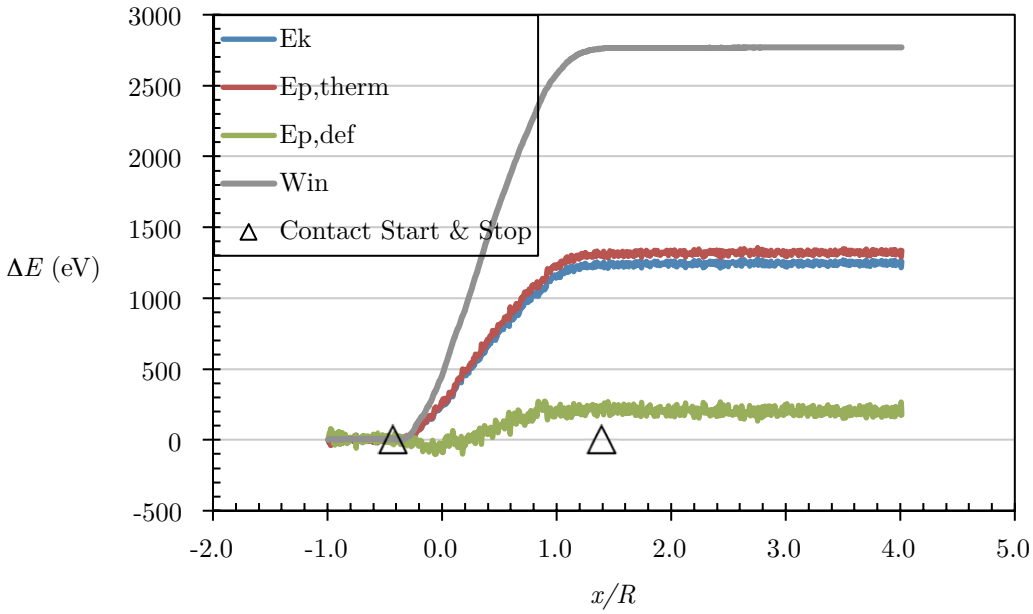

Figure 5.6: The energy change during sliding for $R = 7.5$ nm, $v = 10$ m/s and $\delta/R = 0$

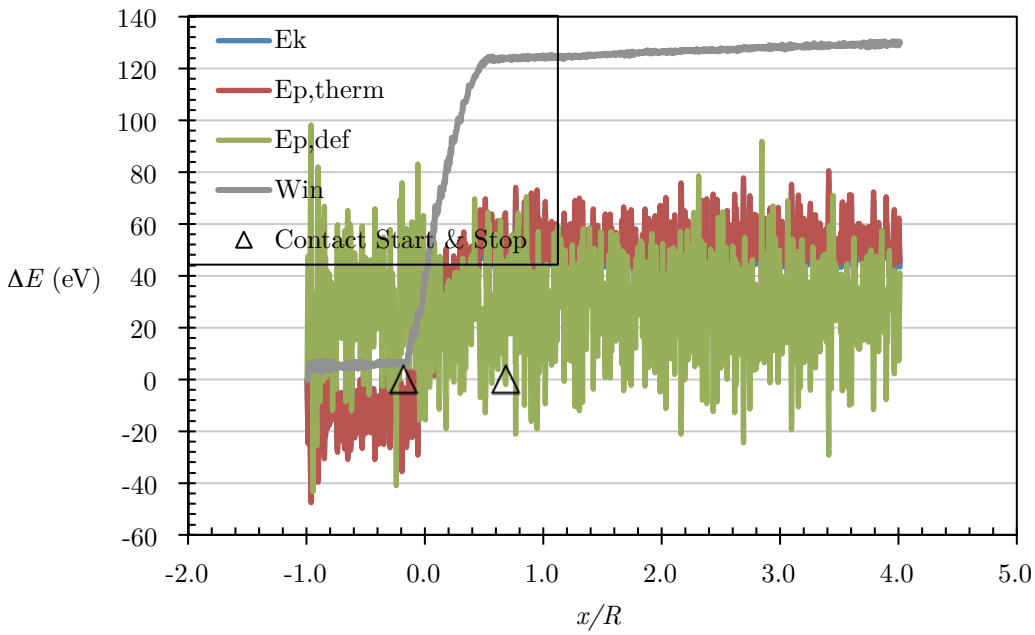

Figure 5.7: The energy change during sliding for $R = 7.5$ nm, $v = 10$ m/s and $\delta/R = -0.04$

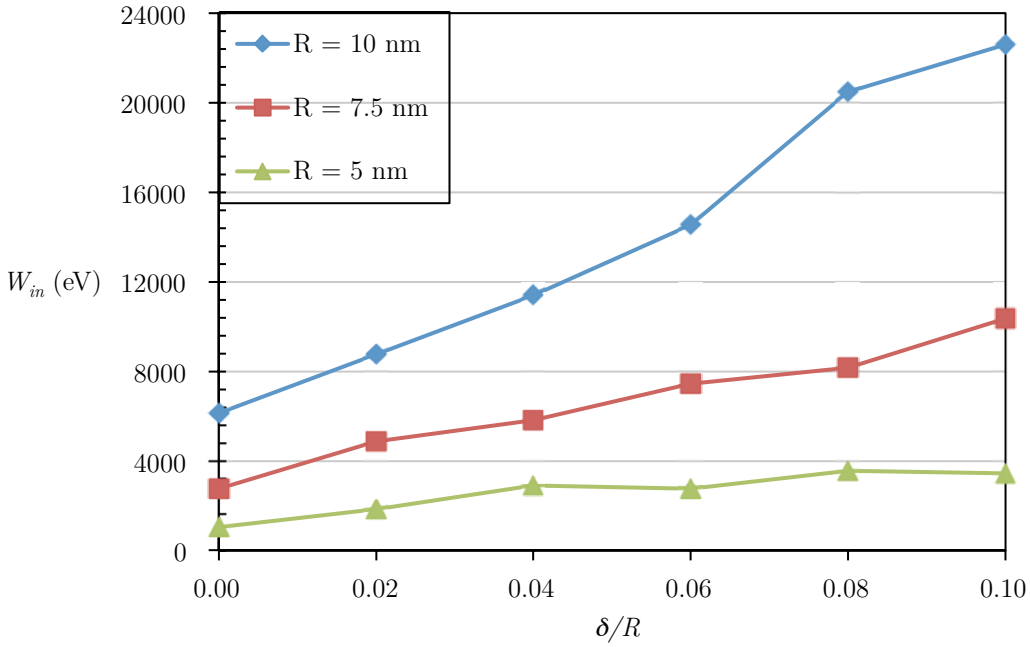

Figure 5.8: Effect of normalized interference on the sliding work done during simulation for $v = 10$ m/s

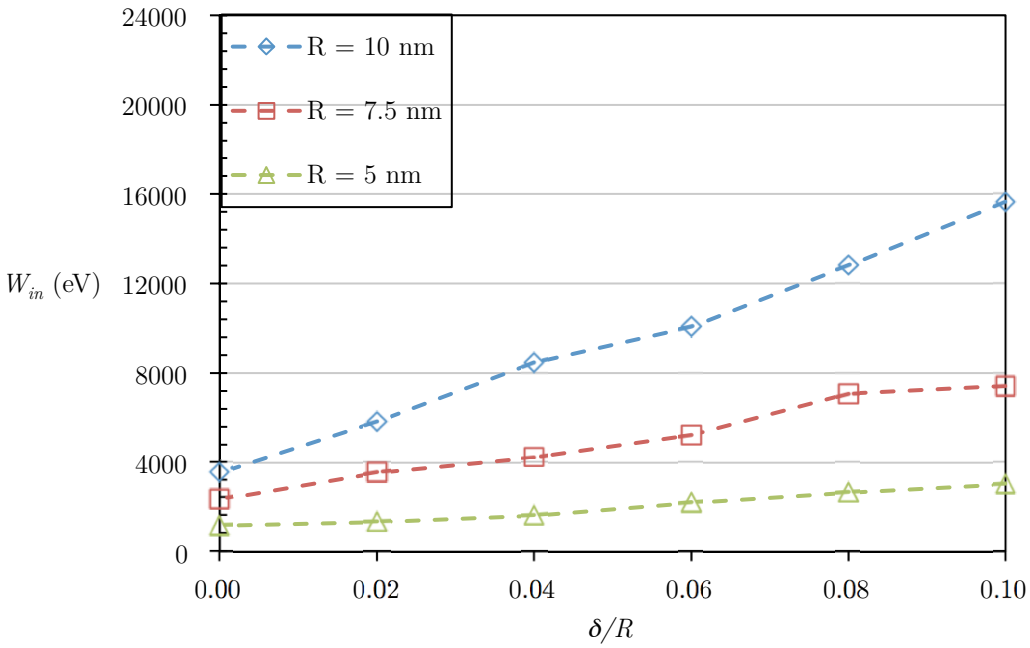

Figure 5.9: Effect of normalized interference on the sliding work done during simulation for $v = 100$ m/s

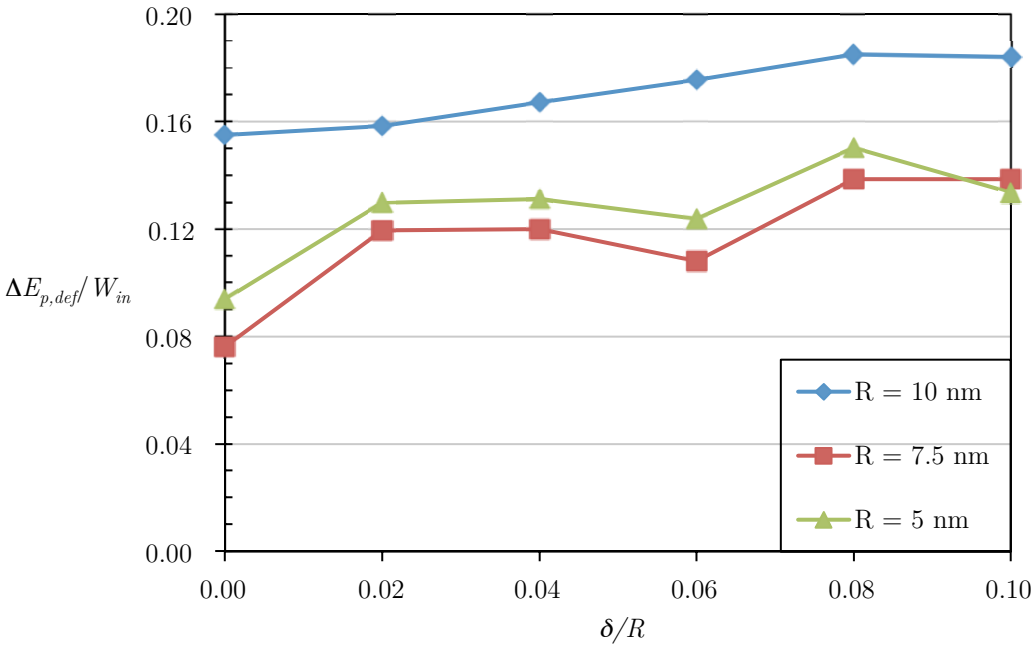

Figure 5.10: Effect of normalized interference on the ratio of change in deformation potential energy to frictional work for $v = 10$ m/s

The interaction volume of asperities is a cubic function of the interference, however, the amount of work done as per the results is almost a linear function of the interference. This could be due to the atomic discretization of the asperity surface at the nano-scale. At zero interference, the work done is not zero since the asperity surfaces are in the attractive range at this value of interference (i.e. it is not a perfectly smooth surface). The surfaces adhere to each other as the asperities slide, plastic deformation occurs, and work is required to pull these surfaces apart. Figure 5.10 and Figure 5.11 show the ratio of change in the deformation potential energy to the frictional work as a function of normalized interference for sliding velocities 10 m/s and 100 m/s, respectively. This ratio shows the contribution of frictional work consumed to deform the original structure of the asperities. As the interference increases, the ratio of deformation potential energy to the frictional work increases almost consistently for the sliding velocity of 10 m/s for all three sizes. But this ratio is fluctuating quite randomly for the sliding velocity of 100 m/s, while showing a slight increasing trend on an average again for all three sizes. This means that the asperity surfaces are deforming more as the interference increases for both the sliding velocities, however, it is less so for the higher sliding velocity. As per the results only ~ 8% - 19% of the frictional work goes into deforming the asperities for a sliding velocity of 10 m/s and this range drops to ~ 7% - 11% for 100 m/s between all three asperity sizes. Again, it should be noted that this deformation potential energy arises purely from the asperity interaction and does not include the thermal potential energy. The values for the ratio of deformation potential energy to frictional work obtained in this work are fairly close to the values obtained by Junge and Molinari [98]. They use a similar analysis to quantify the deformation potential energy in nano-scratching of an aluminum substrate with a spherical aluminum asperity. For their range of substrate heights and sliding velocities, this ratio was in the range of approximately 13% - 16%.

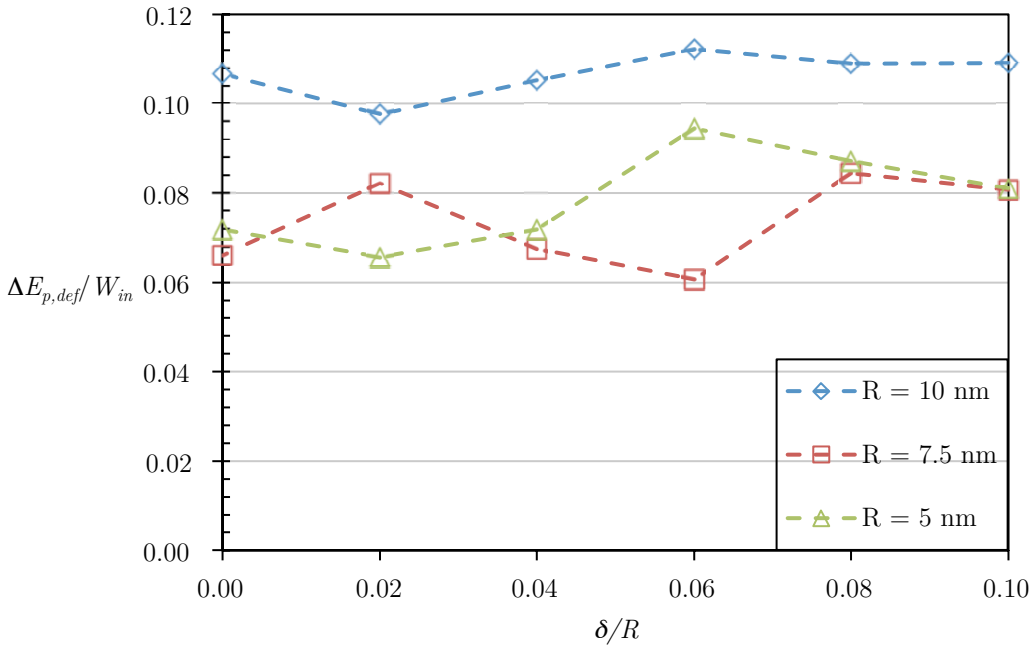

Figure 5.11: Effect of normalized interference on the ratio of change in deformation potential energy to frictional work for $v = 100$ m/s

Figure 5.12 and Figure 5.13 show the ratio of change in the kinetic energy to the frictional work as a function of normalized interference for sliding velocities 10 m/s and 100 m/s respectively. This ratio shows the contribution of frictional work consumed in thermal dissipation manifested as the temperature rise. The trend is complimentary to one observed for the deformation potential energy. This ratio decreases as the interference increases suggesting the reduced contribution to thermal dissipation. Again, the trend for the sliding velocity of 10 m/s is much more consistent than for 100 m/s velocity, nonetheless, the ratios for both decrease with interference. The change in kinetic energy for 10 m/s sliding velocity ranges from approximately 47% - 43% of the total frictional work and the corresponding range for 100 m/s is approximately 49% - 46%. This shows that the majority of the frictional work is converted to thermal kinetic energy. The remaining frictional work besides kinetic energy and deformation potential energy is converted to thermal potential energy as defined previously.

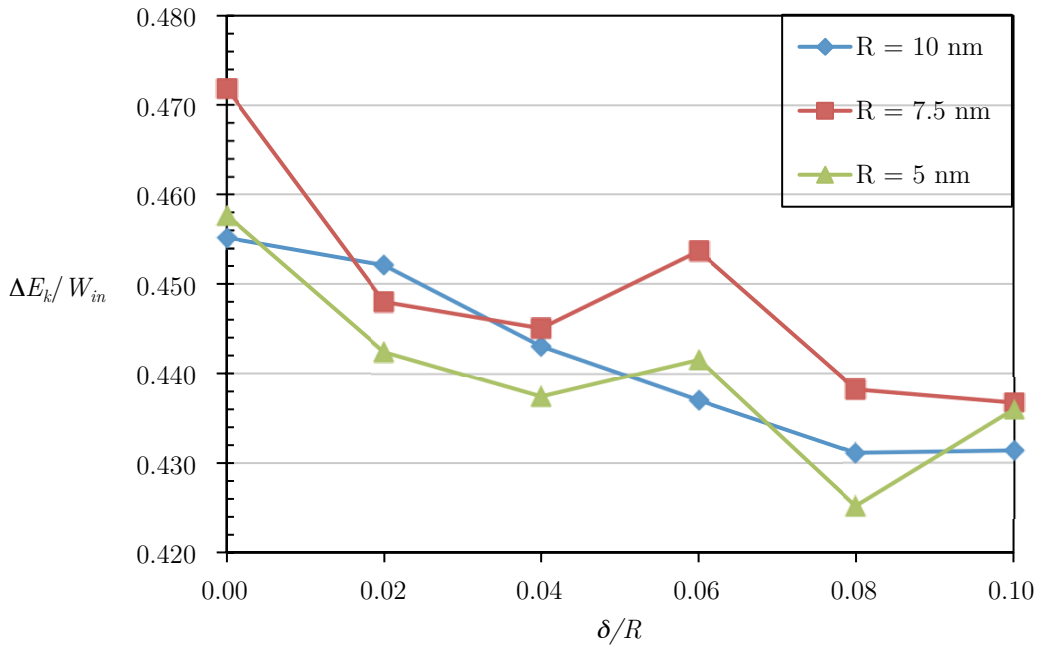

Figure 5.12: Effect of normalized interference on the ratio of change in kinetic energy to frictional work for $v = 10$ m/s

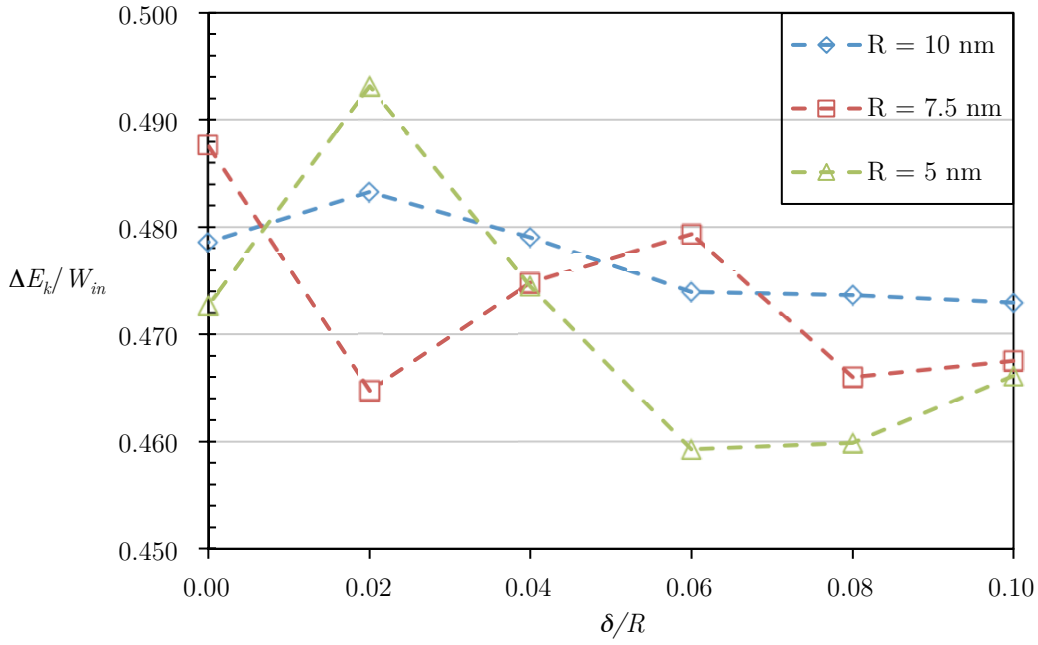

Figure 5.13: Effect of normalized interference on the ratio of change in kinetic energy to frictional work for $v = 100$ m/s

Therefore, the total frictional work converted to thermal dissipation is in the range of ~ 82% - 97% between both sliding velocities and all three asperity sizes.

5.3.2 Effect of Asperity Radius, R

Asperity interference and asperity radius are the two dimensional quantities that control the number of atoms participating in the sliding interaction in the current work. Therefore, the basic effects of these two quantities are also similar. Accordingly, as the asperity radius increases, the frictional work done on the system also increases (Figure 5.8 - Figure 5.9) for both sliding velocities. As the radius is doubled from 5 nm to 10 nm, the increase is frictional work is between 4-6 times for 10 m/s sliding velocity and between 3-5 times for 100 m/s sliding velocity. This is the case for all interference values numerically explored.

The ratio of the change in deformation potential energy to frictional work also increases distinctly as the radius increases to 10 nm. However, it does not show a significant change between 5 nm and 7.5 nm radius asperities (Figure 5.10 - Figure 5.11). This means that the energy distribution does not remain consistent with asperity size. Another interesting result is that the fluctuations observed in the ratios for the smaller asperity sizes, are quite negligible for the 10 nm radius asperity.

The ratio of the change in the kinetic energy to frictional work does not show any trend for changing asperity size and fluctuates significantly for the smaller asperities. Once again the fluctuations for the 10 nm asperity size are negligible when compared to the other two sizes. The dynamic fluctuations seem to dampen out as the asperity size and therefore the number of atoms increases significantly. The primary reason suspected for this is that the discretization of the surface increases as the asperity size gets smaller and as it approaches the lattice constant some of the dimensions cause the surface to fall in between half lattices, where atoms cannot be present.

5.3.3 Effect of Sliding Velocity, v

The values of sliding velocity simulated were 10 m/s and 100 m/s, which were assigned only to the atoms of the upper asperity. Provisions were made so that the system had sufficient time to stabilize at each sliding velocity before the asperities interacted. As mentioned previously, this was particularly important for the case of 100 m/s sliding velocity since the sudden motion caused the atoms of the upper asperity to swing back and forth along the sliding direction. Figure 5.14 shows the frictional work as a function of normalized interference comparing the effect of both sliding velocities. For all three sizes of asperities, the frictional work was lower for the higher sliding velocity of 100 m/s by 20%, 24%, and 33% on average for the 5 nm, 7.5 nm, and 10 nm asperities, respectively. As the velocity increases from 10 m/s to 100 m/s, the momentum also increases 10 times and the translational kinetic energy of the upper asperity increases 100 times. Although this translational kinetic energy does not increase the total internal energy of the system, the frictional work required for the sliding process decreases. This means that adhesion is lower and as a result the in-contact distance is smaller when the sliding velocity is higher. Therefore, the frictional work is lower for this case. This is an important finding that for the case of asperity-asperity interaction like in the current work, the frictional work decreases with increase in velocity but for an asperity-slab interaction by Junge and Molinari [98] the frictional work increased as the velocity increased.

The ratio of change in the deformation potential energy to the frictional work is also lower for the higher velocity. This is consistent for all three asperity sizes, as shown in Figure 5.15 - Figure 5.17. The portion of energy required to deform the asperities is lower for 100 m/s sliding velocity than the 10 m/s cases by 37%, 35%, and 37% on an average for 5 nm, 7.5 nm, and 10 nm asperities respectively. Consequently, the thermal contribution increased for the same case by 7%, 5%, and 8% respectively. Since the thermal potential energy is only a function of temperature as explained previously, the

sum of the kinetic energy and thermal potential energy contributions are higher for the higher velocity case. On an average, for 5 nm, 7.5 nm, and 10 nm asperities the total contribution of the thermal energy increases from 88% to 94%, 89% to 93%, and 83% to 90%, respectively. Thus as the velocity and the asperity momentum in the sliding interaction increases, the thermal dissipation increases while deformation energy decreases. This is again a contradicting result to the one obtained by Junge and Molinari [98] where the plastic energy (equivalent to deformation potential energy) was "somewhat insensitive" to the sliding velocity.

An interesting exception is for the case when $\delta/R = -0.04$ (not included in the charts for clarity). For this case for all three sizes, the frictional work done on the system is higher for the higher velocity. The energy ratios for this case however do not show any definite trend.

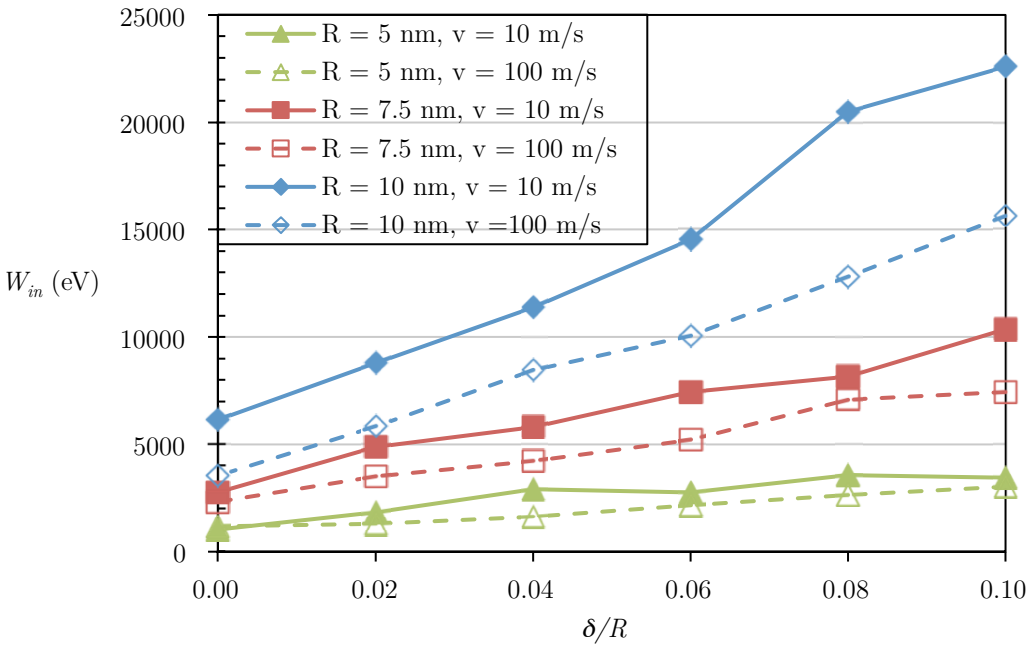

Figure 5.14: The effect of sliding velocity on the frictional work for all asperity sizes

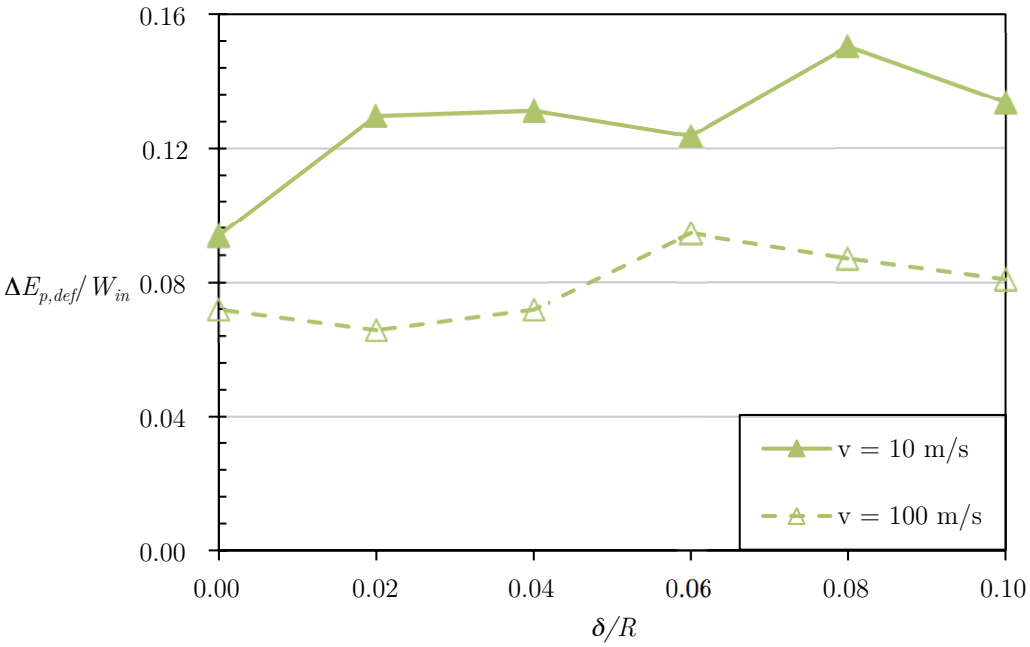

Figure 5.15: Effect of sliding velocity on the ratio of change in deformation potential energy to frictional work for $R = 5$ nm

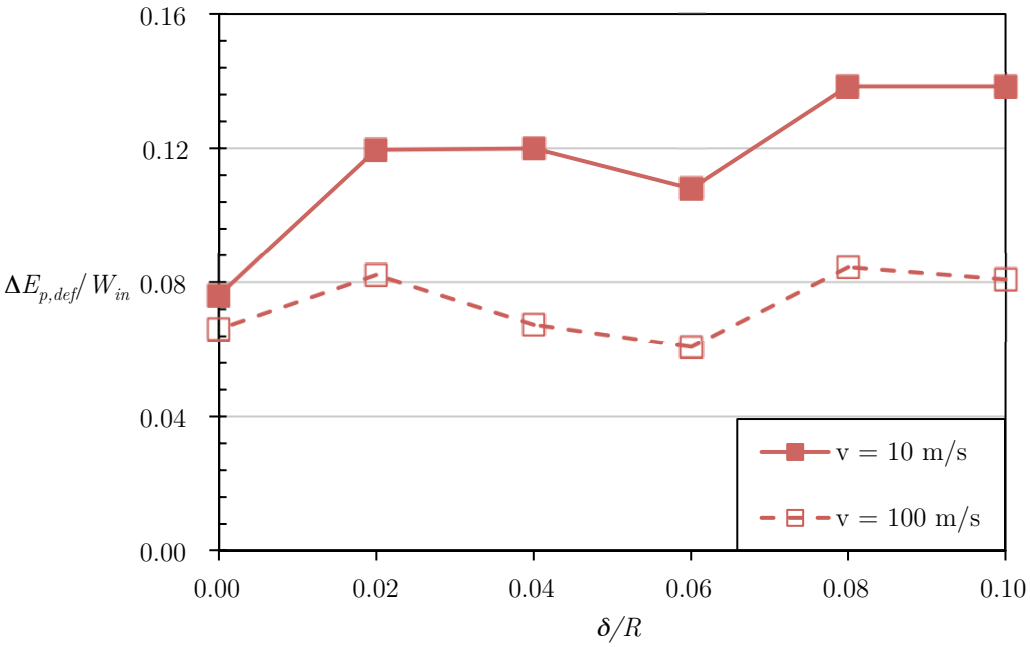

Figure 5.16: Effect of sliding velocity on the ratio of change in deformation potential energy to frictional work for $R = 7.5$ nm

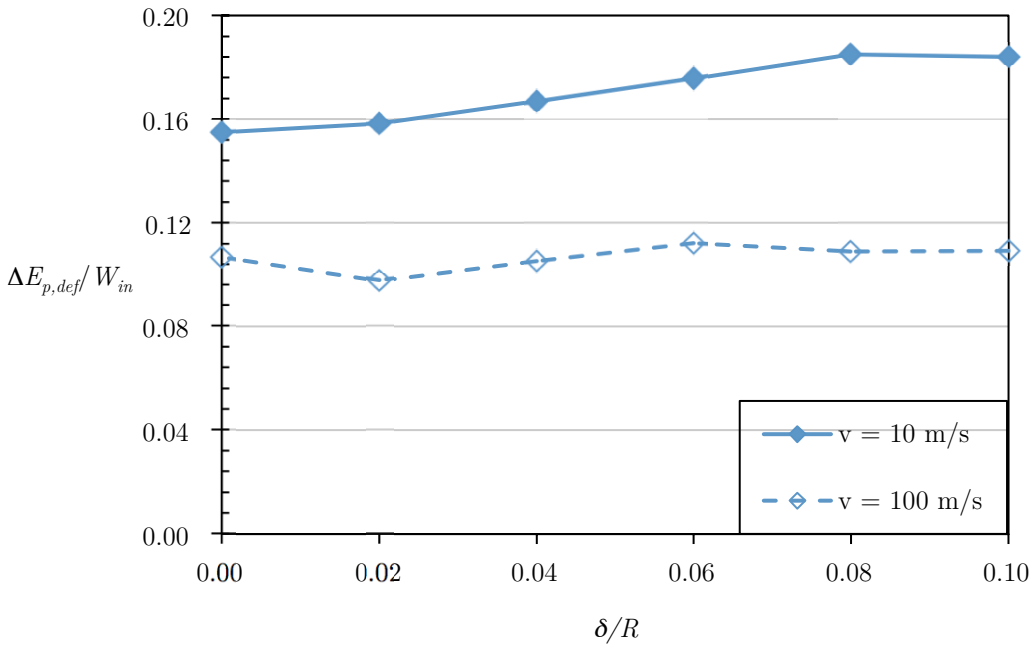

Figure 5.17: Effect of sliding velocity on the ratio of change in deformation potential energy to frictional work for $R = 10$ nm

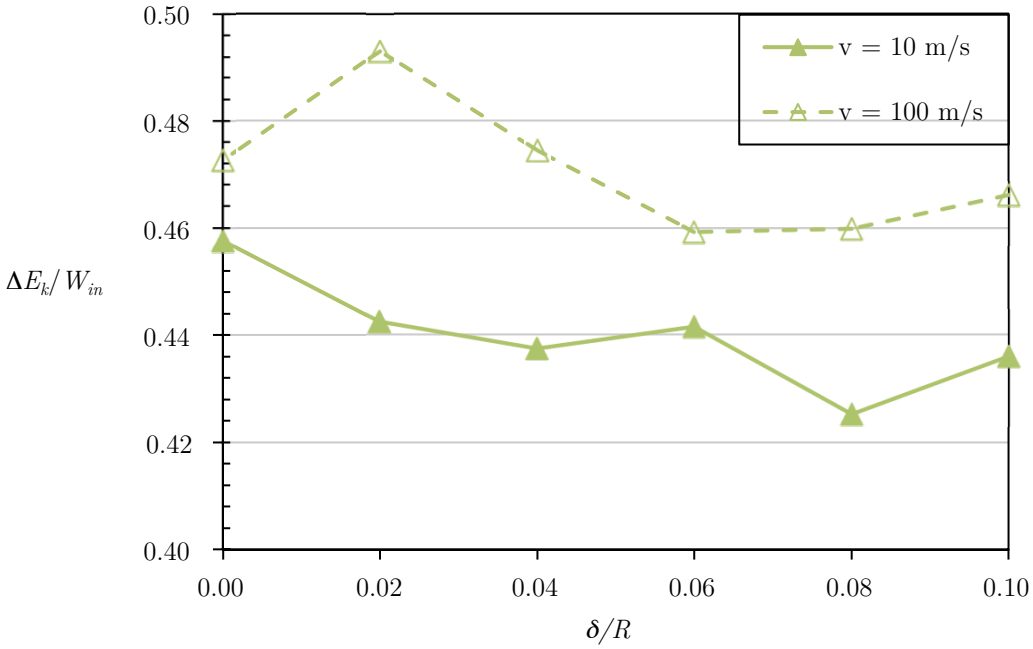

Figure 5.18: Effect of sliding velocity on the ratio of change in kinetic energy to frictional work for $R = 5$ nm

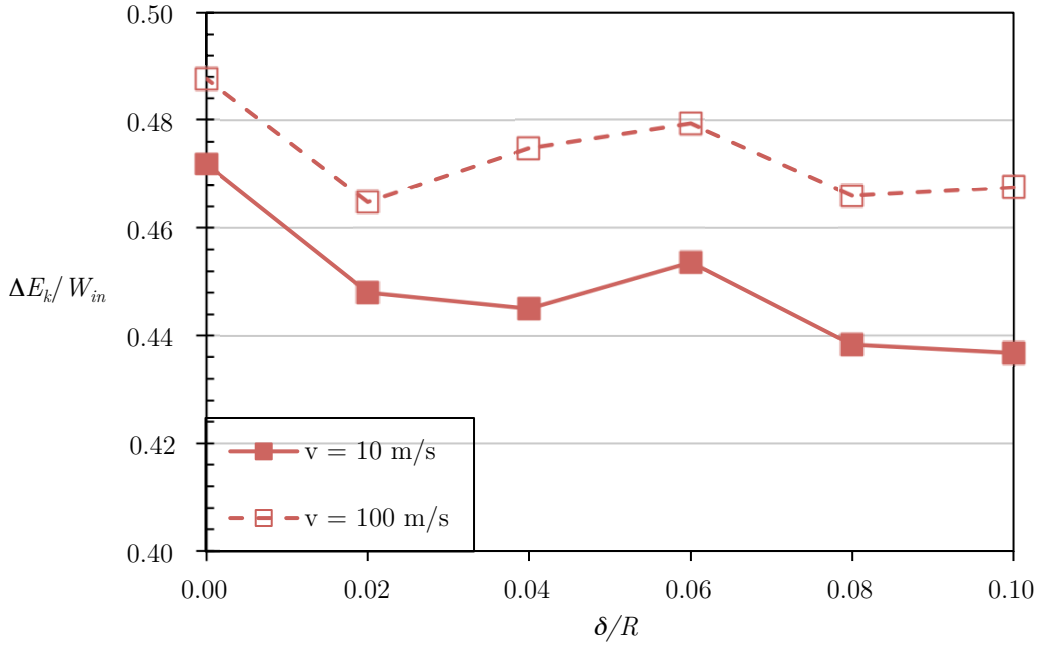

Figure 5.19: Effect of sliding velocity on the ratio of change in kinetic energy to frictional work for $R = 7.5$ nm

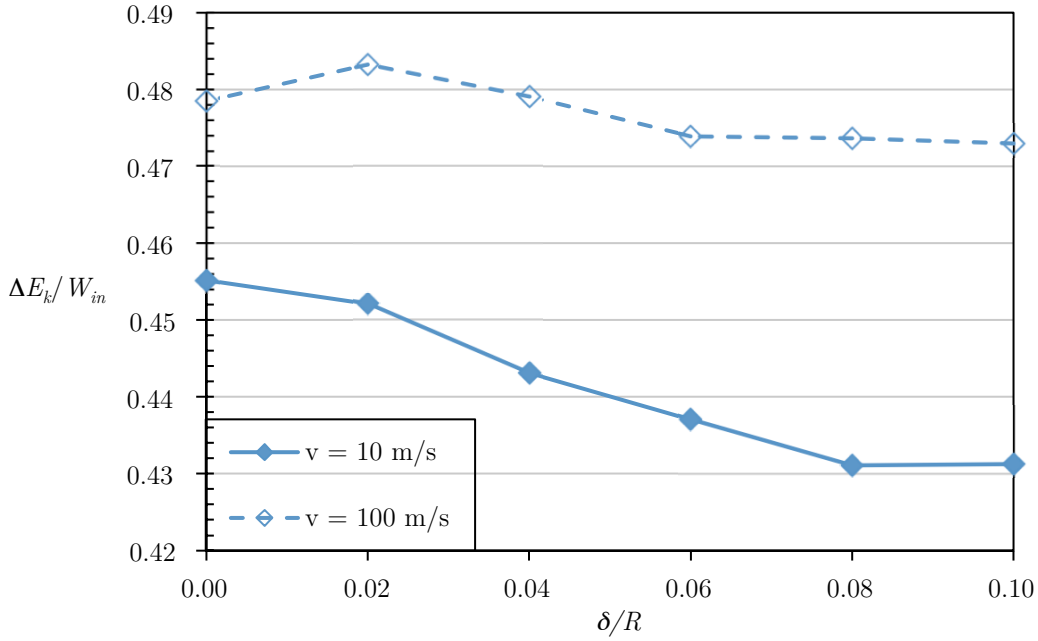

Figure 5.20: Effect of sliding velocity on the ratio of change in kinetic energy to frictional work for $R = 10$ nm

5.3.4 Effect of Time-step Size, Δt

Figure 5.21 and Figure 5.22 show the effect of the increase in the time-step size on the total energy change and the work done in sliding the asperities across each other, respectively, for the asperity size of 7.5 nm sliding at 10 m/s. In both cases the values are significantly higher for the normalized interference values of 0.06 and 0.08 when the time-step size was 0.005 ps. This, however, does not provide us with a useful deduction as to which value of the time-step size provides us with an accurate version of the total energy change or the work done during sliding.

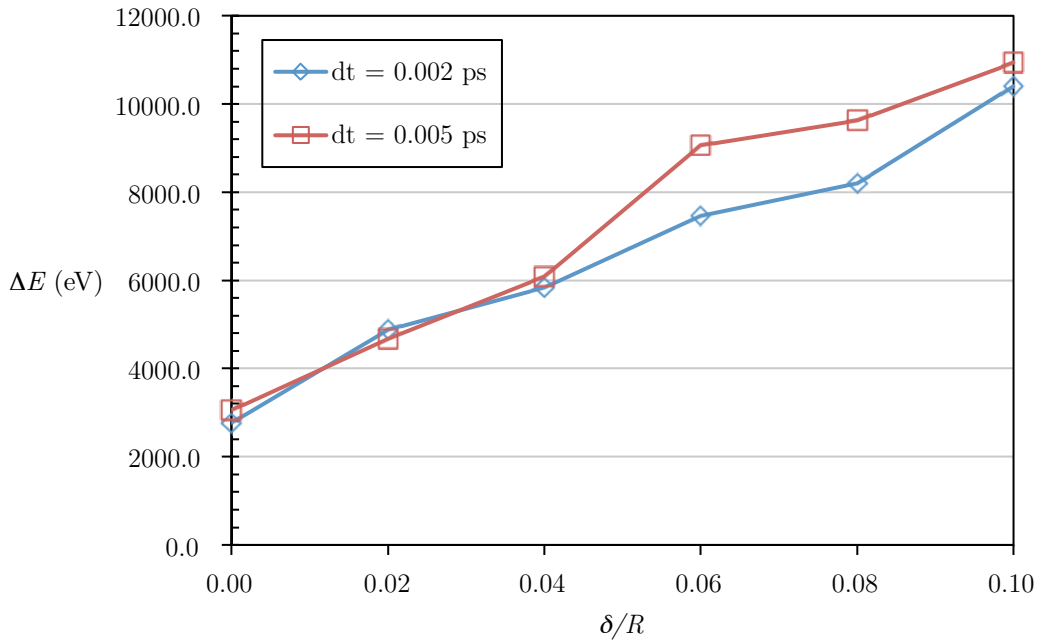

Figure 5.21: The effect of time-step size on the total energy change for $R = 7.5$ nm and $v = 10$ m/s

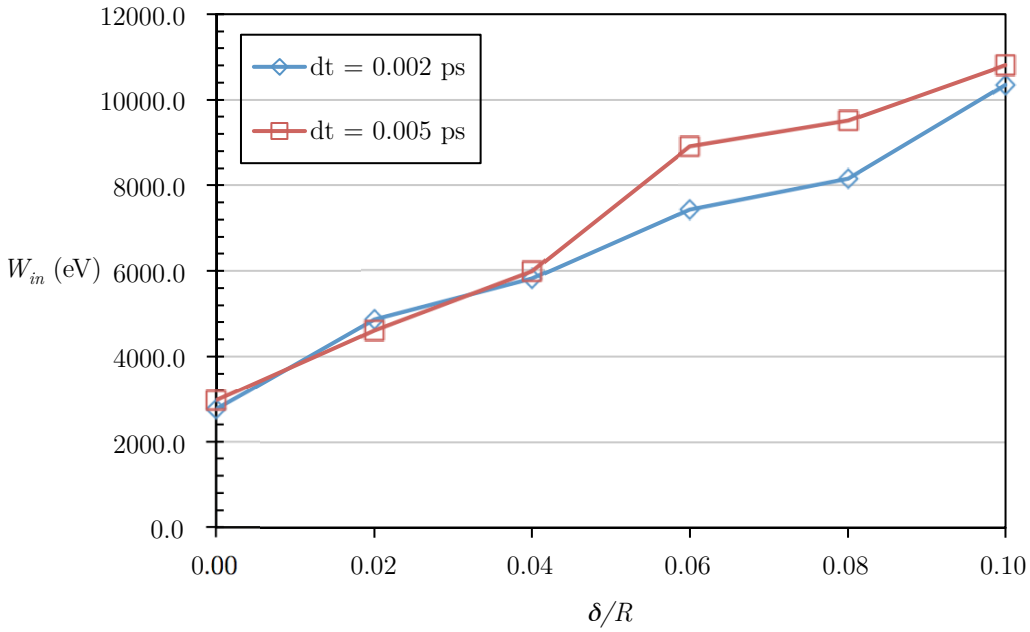

Figure 5.22: The effect of time-step size on the work done for $R = 7.5$ nm and $v = 10$ m/s

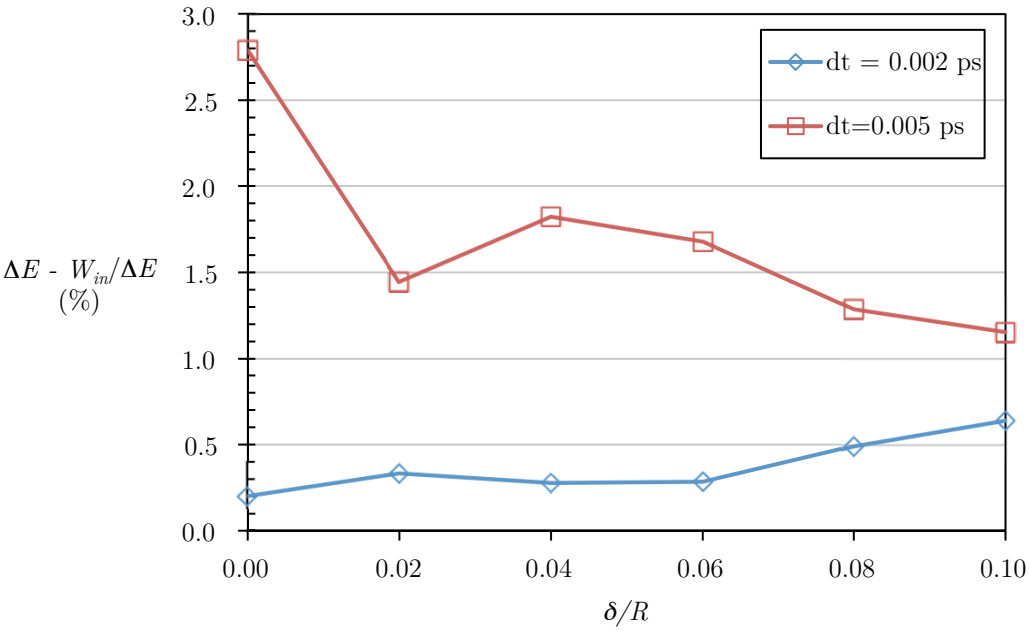

Figure 5.23: The effect of time-step size on the difference between the total energy change and the work done.

Figure 5.23 shows the difference in the values of the total energy change and the sliding work for both the values of the time-step size. In the ideal case, the difference between these values should be zero, provided we can calculate all the values without any approximation and the total energy is conserved. But this is not the case since we are looking for an approximate solution in the absence of an exact one. Accordingly, it can be seen that this difference is proportionally larger for the larger time-step size, therefore suggesting degradation in the energy conservation. This simulation was carried out before all the other simulations and therefore, the time-step size of 0.002 ps was chosen for all the other simulations.

5.3.5 Effect of Lattice Orientation, θ

As the crystal lattice orientation changes, the orientation of the slip planes change and the manner in which the material behaves in a sliding interaction varies. The crystal lattice was rotated about the z-axis to study the effect of orientation on the frictional work and the resulting energy distribution. The asperity of radius 7.5 nm and the sliding velocity of 10 m/s were opted and kept constant for this particular study. The frictional work as a function of lattice orientation for all interference values is shown in Figure 5.24. As the lattice orientation parameter θ is changed from 0° to 45° the frictional work increases to a certain maximum and then decreases. This trend is consistent for all interference values. Figure 5.25 shows the same plot but with second order polynomials fitted to the data for convenience. The frictional work reaches a maximum for a lattice parameter value between 10° and 20° and reaches a minimum at a 45° lattice parameter. As the lattice orientation changes, it also orients the slip planes favorable to sliding, that is parallel to the sliding direction with the most favorable case being achieved when $\theta = 45°$. As a result, the work required to slide the upper asperity across the lower asperity also varies and reaches a minimum when $\theta = 45°$. Table 1 shows the percentage

increase and decrease in the frictional work with respect to $\theta = 0°$ at its maximum and minimum values, respectively. It can be easily seen that the decrease in the frictional work is in the range of 47% - 73% for the most favorable lattice orientation, which is a very significant reduction. It would be helpful to obtain an approximate prediction of the frictional work for the case when the lattice orientation of the crystal structure is randomly distributed over a rough surface of many asperities, which would most likely be a case in a practical sliding contact. Therefore, average values for the frictional work were calculated for every interference value and the results are plotted in Figure 5.26.

Table 5.1: Increase and decrease in frictional work compared to $\theta = 0°$

δ/R	Increase in Frictional Work at maximum value compared to $\theta = 0$ (%)	Decrease in Frictional Work at minimum value compared to $\theta = 0$ (%)
0.10	9	67
0.08	25	47
0.06	21	67
0.04	13	62
0.02	17	71
0.00	62	73

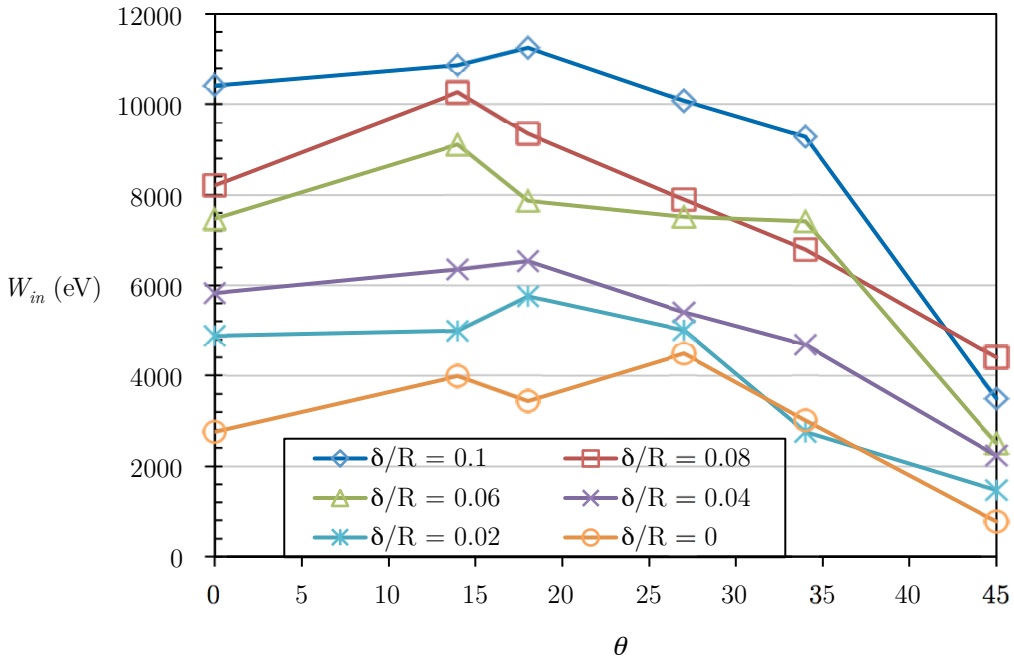

Figure 5.24: Effect of lattice orientation on the frictional work for $R = 7.5$ nm and $v = 10$ m/s

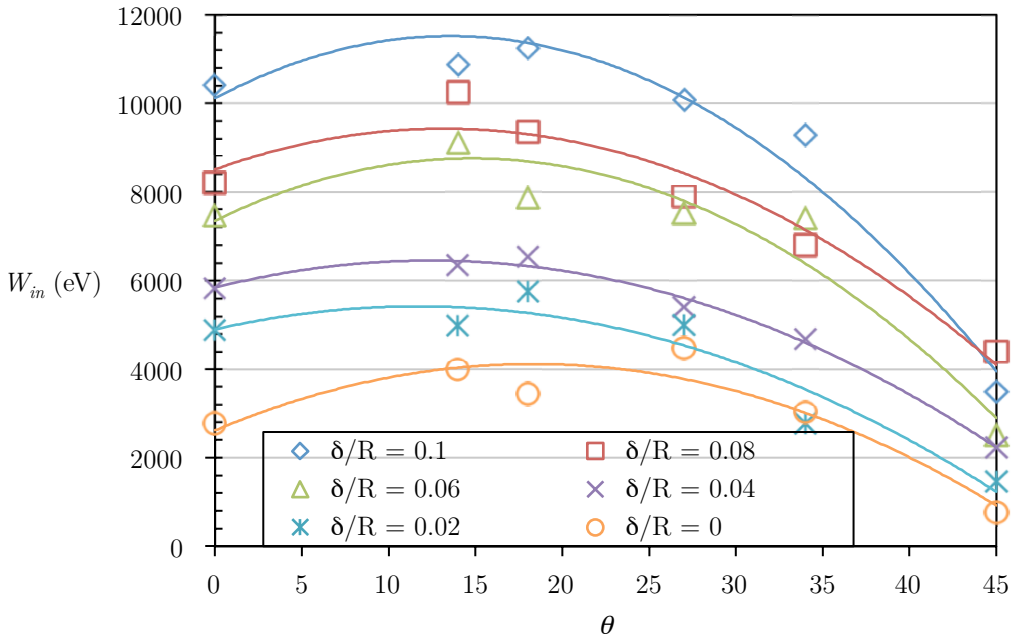

Figure 5.25: Effect of lattice orientation on the frictional work for $R = 7.5$ nm and $v = 10$ m/s with second order polynomials fitted (solid lines)

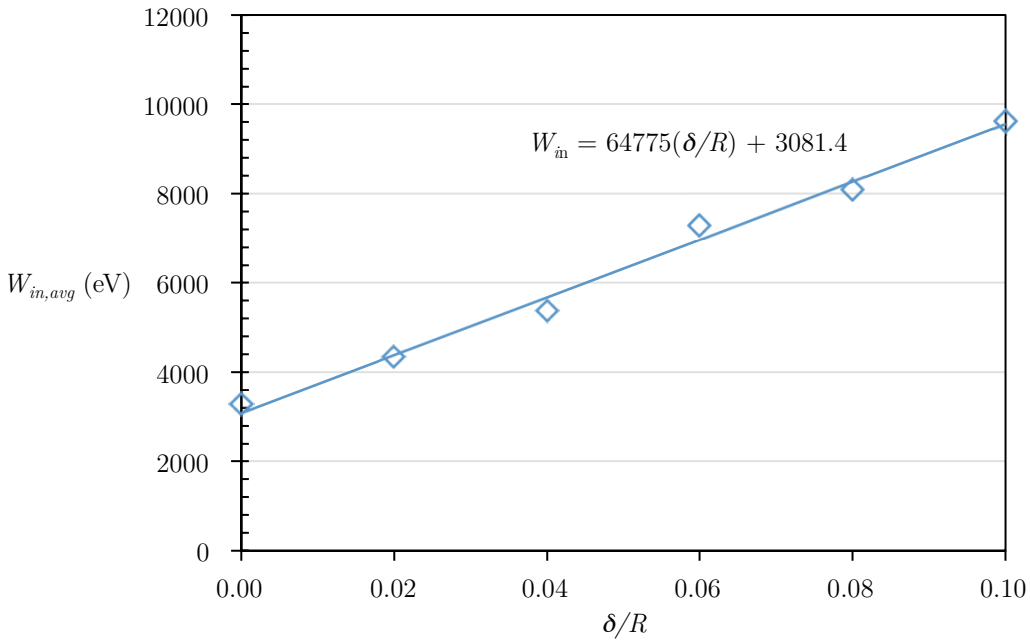

Figure 5.26: Average frictional work as a function of interference. The solid line is a linear fit.

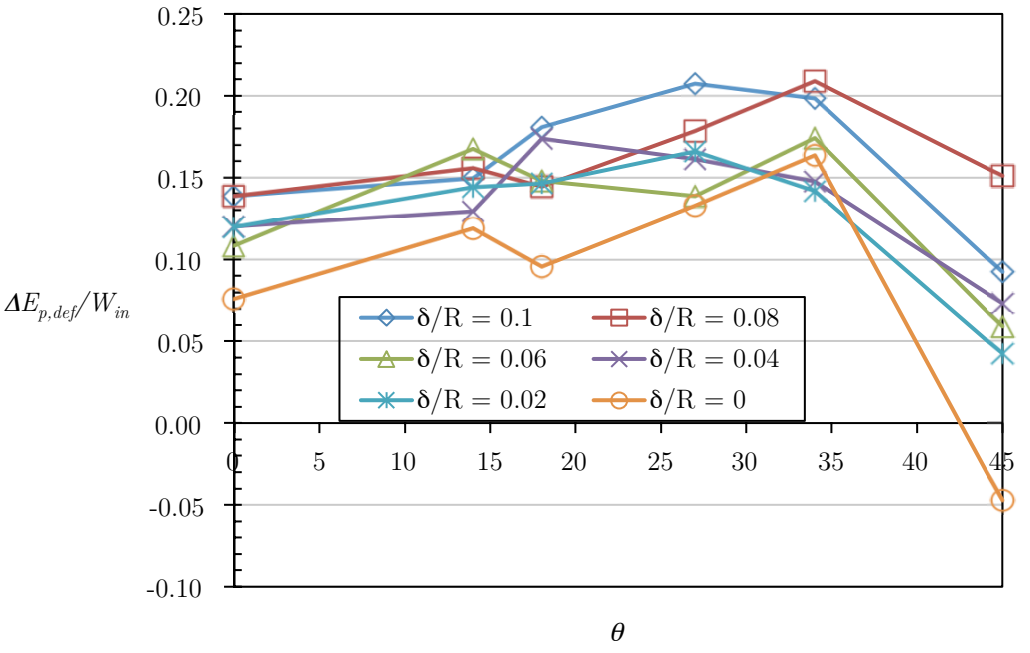

Figure 5.27: Effect of lattice orientation on the ratio of the deformation potential energy to the frictional work for $R = 7.5$ nm and $v = 10$ m/s

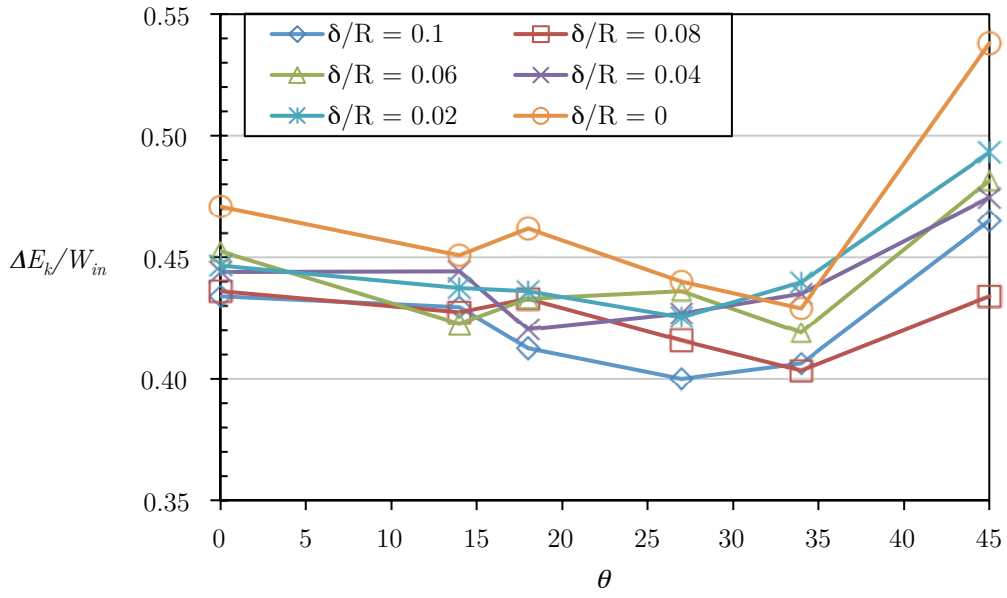

Figure 5.28: Effect of lattice orientation on the ratio of the kinetic energy to the frictional work for $R = 7.5$ nm and $v = 10$ m/s

Figure 5.27 shows the ratio of deformation potential energy to the frictional work as the lattice orientation changes from 0° to 45°. This ratio also increases as θ increases up to a certain value and then it decreases as θ approaches 45°. It reaches a maximum between 25° and 35° and is minimum at 45° for all interference values except at $\delta/R = 0.08$. The ratio for 0° and 45° remains mostly unchanged for this value of normalized interference. Again, the values of the ratio of the deformation potential energy to the frictional work and the ratio of kinetic energy to the frictional work are complimentary to each other. Therefore, a reverse trend is seen for the ratio of kinetic energy to the frictional work (Figure 5.28). These ratios suggest that at certain lattice orientations, the deformation potential energy and therefore the deformation is highest even though the frictional work is not. And therefore the thermal dissipation is also the lowest for the same lattice orientation. At $\theta = 45°$ when the frictional work is lowest for all interference values, the contribution of the deformation potential energy is lowest and that of the thermal

dissipation is highest. This agrees with the case of least deformation that was observed in the visualization of simulations as shown in an earlier section.

5.3.6 Effect of Thermostat

Most of the research done in the field of nano-tribology using molecular dynamics has enforced some form of temperature control on the system; that is, using the canonical ensemble as opposed to the micro-canonical ensemble used in this work. Note that actual asperities should behave between these two cases. To check the influence of a thermostat in the current model, simulations were performed using a velocity scaling thermostat for the asperity of size 7.5 nm for two different lattice orientations of 0° and 45° at 10 m/s sliding velocity. A 300 K thermostat was placed at the bottom of both the asperities throughout the simulation to observe its effect on the friction characteristics as well as energy dissipation. Since energy is drained from the system as a result of the thermostat, the energy balance equation will change as follows

$$\Delta E = W - Q \tag{12}$$

where, Q is the thermal energy drained to maintain the temperature at the base of the asperities. Therefore,

$$W = \Delta E_p + \Delta E_k + Q \tag{13}$$

As mentioned previously, each asperity was divided into five sections of equal heights in the x-z planes where the temperatures were recorded. Figure 5.29 shows the temperatures of each of these sections as the asperity slides in the absence of the thermostat. The data series T1-T5 and T6-T10 belong to the lower asperity and the upper asperity respectively. It can be seen that the temperature of all the sections increase simultaneously as the sliding takes place. This means that there is no significant thermal gradient between the base and the tip of the asperities even in the absence of a thermostat. Figure 5.30 shows

the corresponding data for the case when the thermostat is present and again there is no significant thermal gradient and the temperatures for all the sections remain constant at 300 K. The change in the kinetic energy and the potential energy as well as the frictional work and the thermal energy during sliding in the presence of the thermostat are shown in Figure 5.31. Since the temperature is held constant at 300 K, the kinetic energy and the thermal potential energy do not change. Now the major part of the frictional work is drained as the thermal energy due to the thermostat. Figure 5.32 shows the effect of the thermostat on the frictional work. When the thermostat is present, there seems to be no significant change in the frictional work than for the case of without a thermostat and the trend is consistent as the interference increases. For $\theta = 45°$, the frictional work is again significantly lower following the same trend as before. The ratio of the deformation potential energy to the friction work on the other hand shows some intriguing behavior. For the case when $\theta = 0°$, there is no significant change due to the presence of the thermostat for all interference values except for $\delta/R = 0.06$. Atomic discretization seems to be the cause of this particular inconsistency, but for the case when $\theta = 45°$, the ratio shows the complete opposite trend. As the interference increases, the contribution of deformation potential energy in the absence of the thermostat increases whereas it decreases in the presence of the thermostat. This means that the deformation decreases when the temperature is held constant at 300K for this lattice orientation. Since the temperature is controlled when the thermostat is present, the thermodynamic kinetic energy is also controlled. As shown in Figure 5.34, the ratio of kinetic energy to the frictional work is very low in the presence of the thermostat since the change in the kinetic energy is lower due to the lower temperature change. The ratio decreases from 47% to 2.5% for $\theta = 0°$ and from 49% to 7% for $\theta = 45°$. This change in the ratio is compensated by the heat rejection from the system, Q. As shown in Figure 5.35, the heat rejection from the system is 83% and 72% on average for all interferences for $\theta = 0°$ and $\theta = 45°$ respectively.

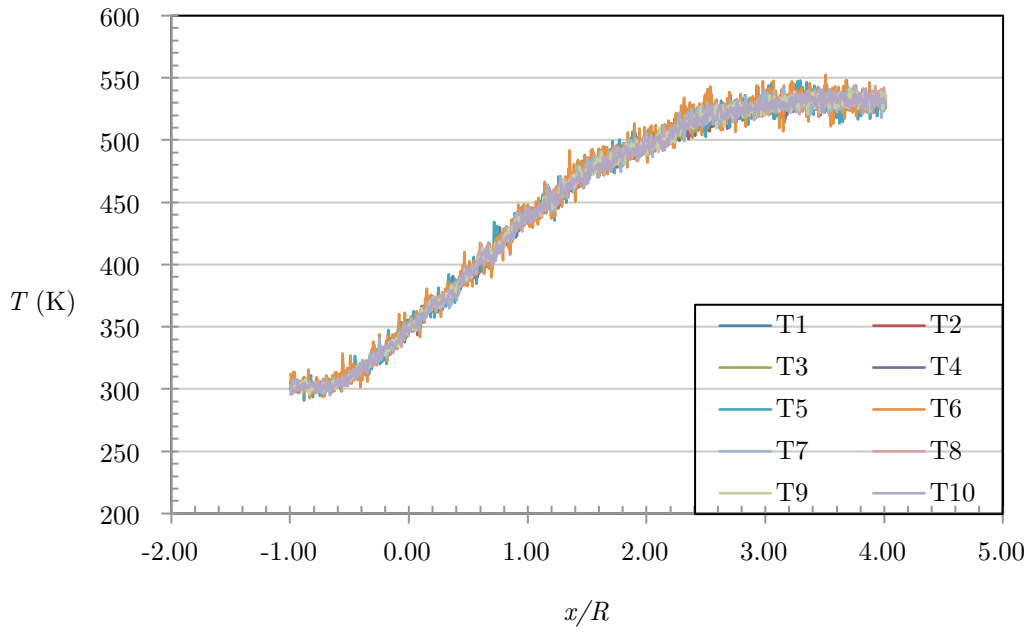

Figure 5.29: Asperity temperatures during the sliding interaction for $R = 7.5$ nm, $v = 10$ m/s and $\delta/R = 0.1$, without thermostat

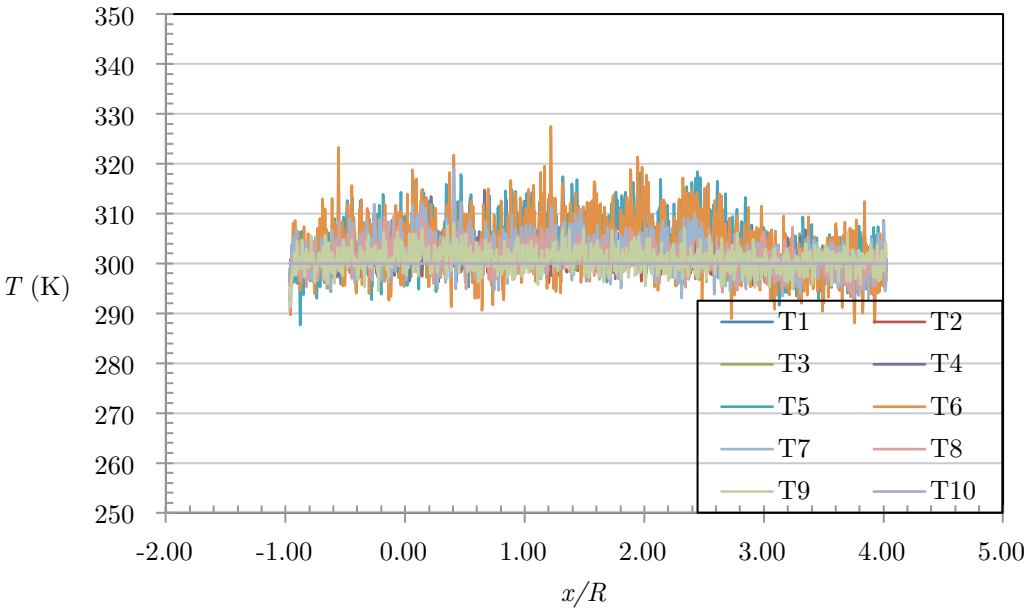

Figure 5.30: Asperity temperatures during the sliding interaction for $R = 7.5$ nm, $v = 10$ m/s and $\delta/R = 0.1$, with thermostat

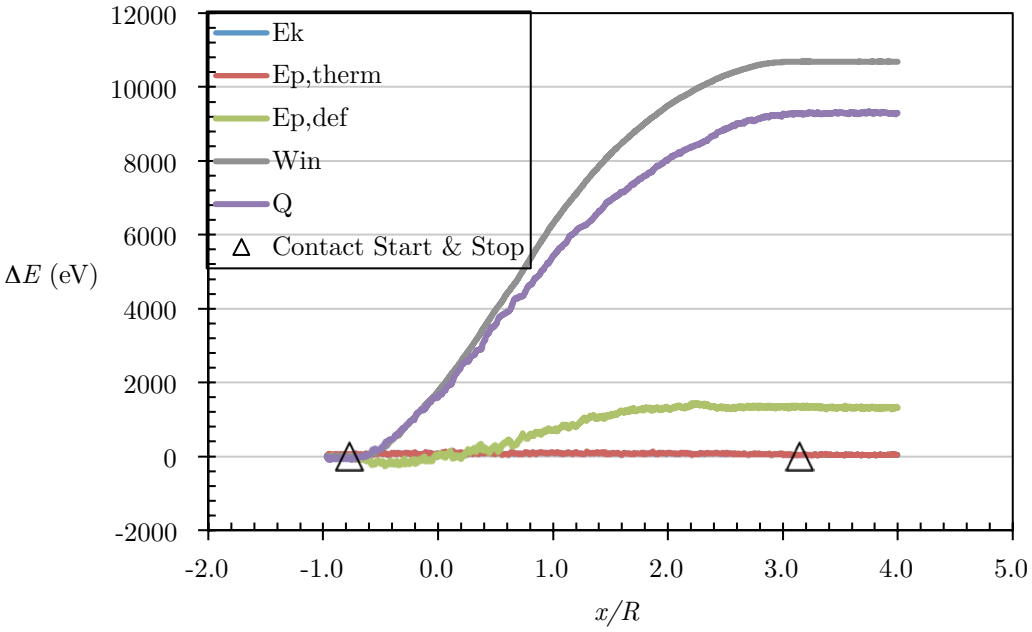

Figure 5.31: The energy change during sliding for $R = 7.5$ nm, $v = 10$ m/s and $\delta/R = 0.1$, with thermostat

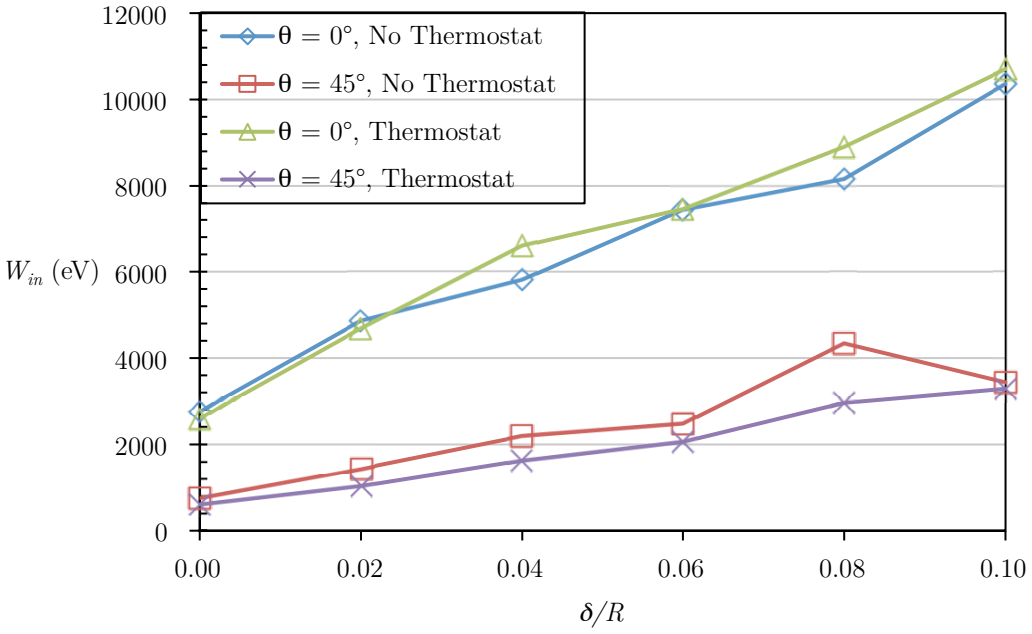

Figure 5.32: Effect of thermostat on the frictional work for $R = 7.5$ nm, $v = 10$ m/s

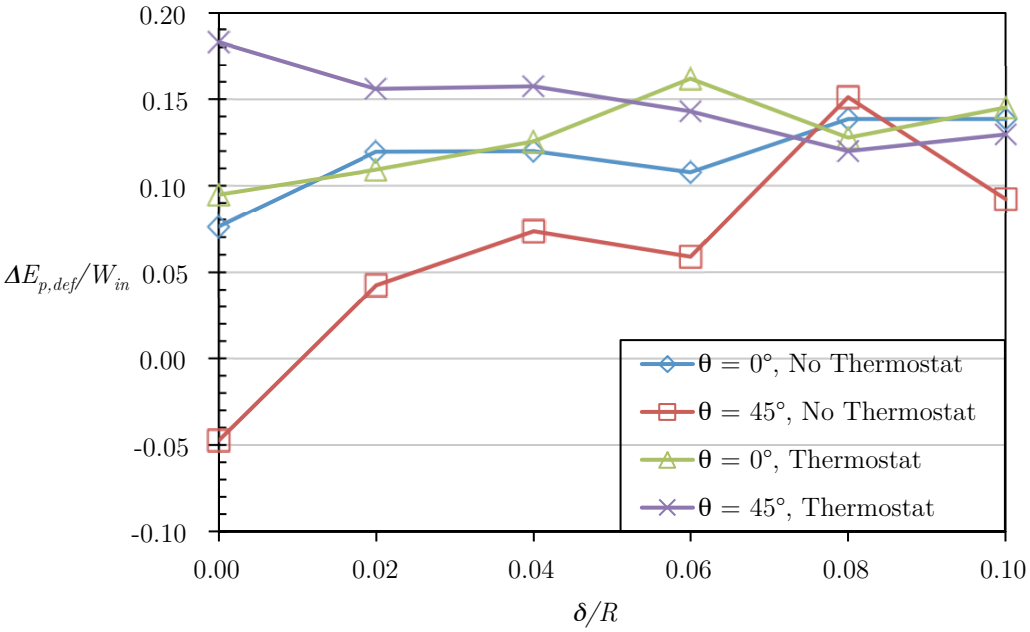

Figure 5.33: Effect of thermostat on the ratio of the deformation potential energy to the frictional work for $R = 7.5$ nm, $v = 10$ m/s

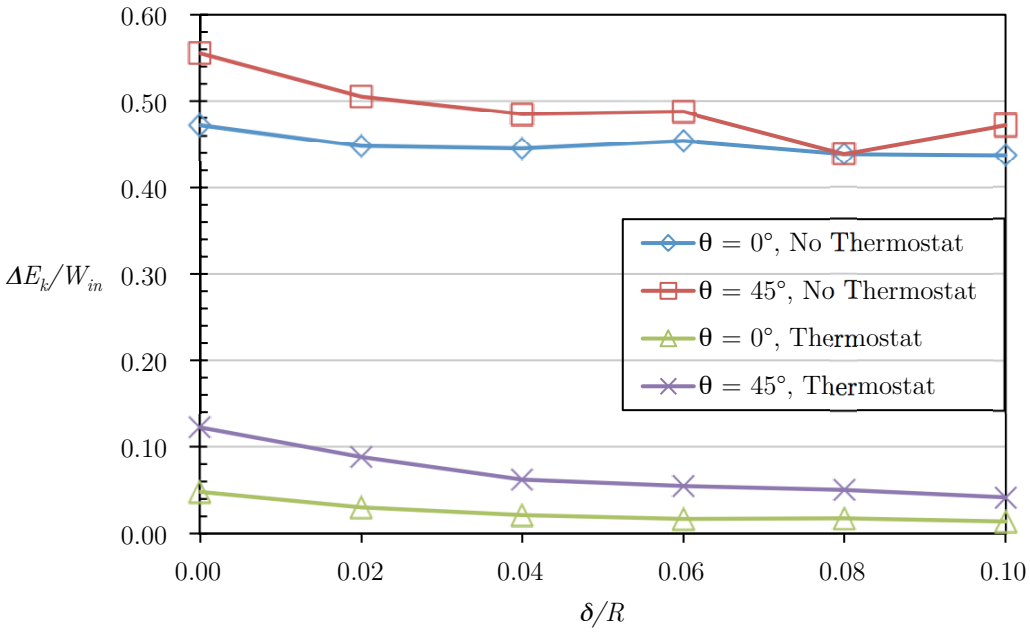

Figure 5.34: Effect of thermostat on the ratio of the kinetic energy to the frictional work for $R = 7.5$ nm, $v = 10$ m/s

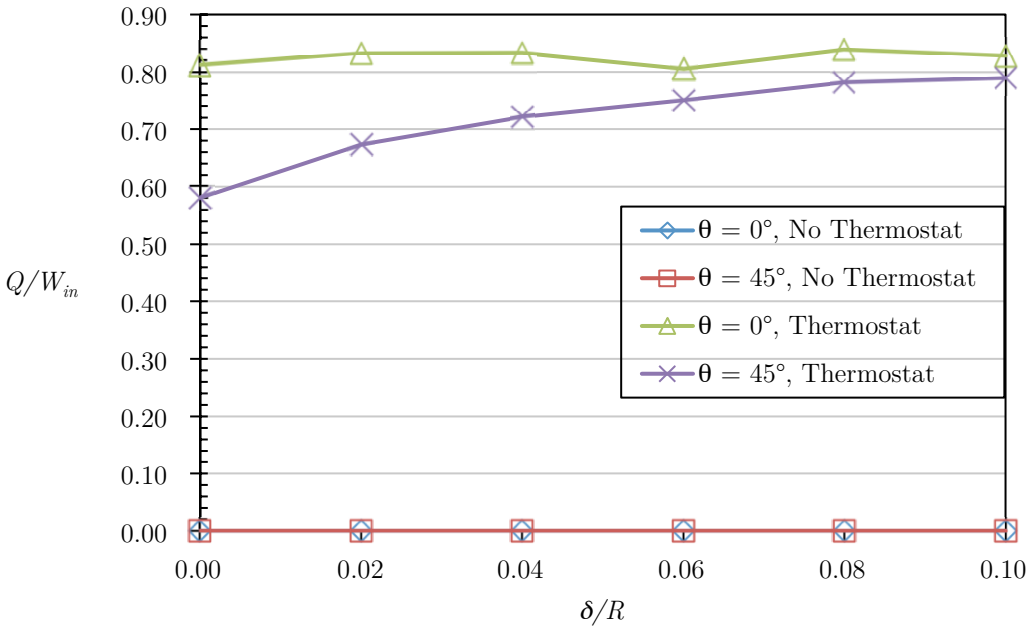

Figure 5.35: Effect of thermostat on the heat rejection from the system for $R = 7.5$ nm, $v = 10$ m/s

Overall, it can be deduced that the presence of the thermostat did not produce any significant change as far as frictional work is concerned. The only change seen is due to a change in the lattice orientation, which is consistent with the previous analysis. Even though the energy distribution was shuffled between ΔE_k and Q, total thermal dissipation was still the major sink to the frictional work input and constituted about 87% and 85% for $\theta = 0°$ and $\theta = 45°$, respectively.

5.4 Conclusions

A molecular dynamics study was performed to investigate the energy dissipation mechanism in a sliding process of an asperity-asperity contact of single crystal copper. The interference, asperity size, sliding velocity, and lattice orientation were varied to study their effects on the atomistic origins of frictional work and energy distribution.

Additionally, the effect of a velocity-scaling thermostat was studied for selected asperity sizes and sliding velocities.

The frictional work has been separated into change in potential energy, kinetic energy and heat rejection. The potential energy is further bifurcated to thermal potential energy, arising due to the system temperature, and deformation potential energy, which arises from the dislocation of the atoms from their initial equilibrium positions (i.e. thermal expansion). Thereby, the contribution of the frictional work to asperity deformation and thermal dissipation has been quantified.

The frictional work is directly proportional to the number of atoms participating in the sliding interaction and therefore to the size of the asperities and the interference between the asperities. It is an inverse function of the sliding velocity and decreases significantly as the sliding velocity is increased. This is due to the additional momentum of the upper asperity atoms resulting from the increased velocity. The lattice orientation also significantly affected the frictional work. It was maximum for a lattice orientation parameter range of 10° - 20° and was minimum for a lattice orientation parameter value of 45°. The presence of a thermostat at the base of both asperities did not affect the frictional work appreciably.

The deformation potential energy contribution increases as the interference and asperity size increases. However this increase is less sensitive to the higher velocity. Again, the deformation potential energy is inversely related to the sliding velocity and the previous argument for this applies here as well. The lattice orientation significantly affected the deformation potential energy which was maximum for the lattice orientation parameter range of 25° - 35° and was minimum for a lattice orientation parameter value of 45°. Thus, the frictional work and the deformation potential energy assume peak values at different orientations but both have their lowest values at 45°. The presence of a thermostat only affected the deformation potential energy for a lattice orientation parameter value of 45° when it decreases with increasing interference. The thermal energy

dissipation is complimentary to the deformation potential energy and hence showed reversed trends. The majority of the frictional work for all the cases was converted to thermal energy dissipation through the combination of thermal potential energy with kinetic energy (without a thermostat) or kinetic energy and heat rejection (with a thermostat).

The dynamic fluctuations were considerable for smaller asperity sizes and they damped out for the asperity with a 10 nm radius. This is believed to be primarily due to the severe atomic discretization of the asperity surface.

Chapter 6

Summary and Conclusions

6.1 Key Developments

In this work sliding interaction between two hemispherical copper asperities were simulated using molecular dynamics. Atomistic origins of friction were studied and the energy dissipation mechanics were analyzed qualitatively and quantitatively. LAMMPS, the molecular dynamics code developed at Sandia National Laboratories, was used to set up the friction model and to run the simulations. LAMMPS was first used to simulate LJ argon and thereby calculate its pressure and internal energy. EOS for LJ fluid developed analytically as well as using results of several computer experiments, along with a similar molecular dynamics work is used to learn and validate LAMMPS.

In the physical model, the lower asperity is fixed while the upper asperity slides past it with a finite interference and a fixed velocity at 300 K starting temperature. Both the asperities were made up of copper atoms in an fcc lattice structure. The effects of the interference between the asperities, asperity size, sliding velocity, lattice orientation, and temperature control on friction mechanisms as well as energy dissipation mechanisms were studied.

In the absence of any impurities on the surface, the atoms from both the asperities formed bonds and acted as one single structure when the asperities ploughed against each other. Such adhesion (or cohesion) dictated the sliding process and resulted in higher values of effective friction coefficient. However, when the average was taken over different

lattice orientations, the values of the effective friction coefficient greatly agree with macro-scale measurements of extremely clean surfaces in vacuum. Therefore, for the current geometry, the friction values at nano-scale are not different from those at macro-scale.

For the range of sliding velocity considered in this work, its variation presented no significant change in the friction characteristics as the duration of contact was not long enough to realize its effect. However, the higher velocity reduced the adhesion effect between the asperities and therefore they remained in contact for a shorter length of the sliding distance. Therefore, the frictional work also decreased significantly as the sliding velocity increased due to the additional momentum of the upper asperity atoms resulting from the increased velocity.

At nano-scale, the surfaces of devices or structures are not smooth but are rather discretized. This discretization governs the lattice alignment of the contacting surfaces with matching lattice orientations and affects the frictional mechanisms significantly. As the asperity size increased this effect started decreasing. Lattice orientation also presented a significant influence on the frictional characteristics with a reduction in the effective friction coefficient by a factor of about 6 for the range of orientation considered. Therefore, if the lattice orientation could be controlled during fabrication of nano-structures, friction characteristics could be tailored.

The frictional work has been separated into change in potential energy, kinetic energy and heat rejection. The potential energy is further bifurcated to thermal potential energy, arising due to the system temperature, and deformation potential energy, which arises from the dislocation of the atoms from their initial equilibrium positions (i.e. thermal expansion). Thereby, the contribution of the frictional work to asperity deformation and thermal dissipation has been quantified.

The deformation increased as the interference and the asperity size increased but decreased with an increase in the sliding velocity. Correspondingly, thermal dissipation decreased with interference and asperity size but increased with sliding velocity. The

thermal energy dissipation is complimentary to the deformation and hence showed reversed trends. The majority of the frictional work for all the cases was converted to thermal energy dissipation through the combination of thermal potential energy with kinetic energy (without thermostat) or kinetic energy and heat rejection (with thermostat). Thus, energy dissipation agrees with macro scale estimations [99]. The presence of a thermostat at the base of both asperities did not appreciably affect the frictional characteristics or the energy dissipation.

6.2 Statement of Intellectual Contribution

In order to better predict friction and therefore control friction in various tribological applications including MEMS/NEMS, the gap between the knowledge of nano-scale friction and macro-scale friction must be bridged. Questions such as - what size and number of individual asperities represent a real macro-scale surface and under what governing parameters does the nano-scale friction values converge to macro-scale values - need to be answered. This work presents qualitatively and quantitatively the influence of the individual parameters on the friction mechanisms at the nano-scale which is necessary in answering these questions.

6.3 Suggestions for Future Work

Asperity-asperity interactions are the fundamental unit of the friction process between two surfaces. When two surfaces slide over each other, several asperity pair interactions take place simultaneously. Therefore, an obvious extension would be to develop a method to analyze friction and energy dissipation for multiple asperity pair interactions. This work could be extended to predict the frictional characteristics for a nano-scale rough surface using the following two techniques:

6.3.1 MD Simulations of Multiple Asperity Pair

MD can be used to simulate multiple asperities interacting simultaneously using a model similar to the one used in the current work. The effect of asperities of varying size, varying shape, and varying lattice orientation placed randomly on a surface can be studied, which would mimic a real surface much closely. It would also provide a means of keeping the surfaces in contact for a longer sliding distance, as the chances of having at least one asperity pair in contact at any point of time would be higher. Such a geometric model would provide a more accurate understanding of the sliding mechanisms compared to the combination of single geometric features. However, multiple asperity pairs would quickly increase the number of atoms in the system and therefore techniques allowing for accelerated dynamics or larger time-step size [72] or hybrid methods would have to be utilized if the available computational powers are not sufficient to handle the huge number of atoms in the system.

6.3.2 Statistical Model

Another approach to extend the current work would be using a statistical model. Statistical extensions to single asperity results have been successfully done to estimate the frictional characteristics at macro- and micro-scales [100]. A statistical model can be used as follows [101]:

If $\bar{\mu}(\delta)$ is an interference dependent frictional property of a single asperity then statistically the same property over a nominal area, A_n and asperity density, η is given by

$$\mu(\delta) = \eta A_n \int_d^\infty \bar{\mu}(\delta)\phi(z)dz \tag{6.1}$$

where $\phi(z)$ is a Gaussian Distribution given by

$$\phi(z) = \frac{1}{(2\pi)^{\frac{1}{2}}\sigma_s} exp\left(-\frac{z^2}{2\sigma_s^2}\right) \tag{6.2}$$

$$z = \delta + d \tag{6.3}$$

Here, σ_s is the standard deviation of the asperity heights, z is the asperity height measured from the mean of asperity heights and d is the separation based on asperity heights.

The results for $R = 7.5$ nm from the current work:

$$\bar{\mu}(\delta) = 0.106\delta + 0.867 \tag{6.4}$$

Using equations (6.1) and (6.4) gives

$$\mu(\delta) = \eta A_n \frac{1}{(2\pi)^{\frac{1}{2}}\sigma_s} exp\left(-\frac{d^2}{2\sigma_s^2}\right) \int_0^\infty (0.106\delta + 0.867) exp\left[\frac{(-\delta^2 + 2\delta d}{2\sigma_s^2}\right] d\delta \tag{6.5}$$

This is the friction coefficient of the entire area.

References

[1] John Williams, *Engineering Tribology.*: Cambridge University Press, 2006.

[2] O. M. Braun and A. G. Naumovets, "Nanotribology: Microscopic mechanisms of friction," *Surface Science Reports*, vol. 60, pp. 79-158, 2006.

[3] M. H. Cho, S. J. Kim, D. Lim, and H. Jang, "Atomic scale stick-slip caused by dislocation nucleation and propagation during scratching of a Cu substrate with a nanoindenter: a molecular dynamics simulation," *Wear*, vol. 259, pp. 1392-1399, August 2005.

[4] S. Achanta, T. Liskiewicz, D. Drees, and J. Celis, "Friction mechanisms at the micro-scale," *Tribology International*, vol. 42, pp. 1792-1799, Dec. 2009.

[5] Somuri V. Prasad, Michael T. Dugger, Todd R. Christenson, and David R. Tallant, "LIGA Microsystems: Surface Interactions, Tribology, and Coatings," *Journal of Manufacturing Processes*, vol. 6, no. 1, 2004.

[6] C. Mathew Mate, *Tribology on the Small Scale: A Bottom Up Approach to Friction, Lubrication, and Wear*, 1st ed., Harold G. Craighead et al., Eds. New York, USA: Oxford University Press, 2008.

[7] R. Arvind Singh, Kyounghwan Na, Jin Woo Yi, Kwang-Ryeol Lee, and Eui-Sung Yoon, "DLC nano-dot surfaces for tribological application in MEMS devices," *Applied Surface Science*, vol. 257, pp. 3153-3157, 2011.

[8] S. L. Miller et al., "Failure modes in surface micromachined microelectromechanical actuation systems," *Microelectronics Reliability*, vol. 19, pp. 1229-1237, 1999.

[9] N. Ansari and W. R. Ashurst, "An easy-to-fabricate improved microinstrument for systematically investigating adhesion between MEMS sidewalls," *Applied Surface Science*, vol. 257, pp. 10917-10925, 2011.

[10] W. Robert Ashurst, M. P. de Boer, C. Carraro, and R. Maboudian, "An investigation of sidewall adhesion in MEMS," *Applied Surface Science*, vol. 212-213, pp. 735-741, 2003.

[11] S. Ciraci and A. Buldum, "Atomic scale study of friction and energy dissipation," *Wear*, vol. 254, pp. 911-916, 2003.

[12] Yang Ping and Liao NingBo, "Surface sliding simulation in micro-gear train for adhesion problem and tribology design by using molecular dynamics model," *Computational Materials Science*, vol. 38, pp. 678-684, 2007.

[13] J. A. Harrison, C. T. White, R. J. Colton, and D. W. Brenner, "Molecular-dynamics simulations of atomic-scale friction of diamond surfaces," *Physical Review B*, vol. 46, no. 15, pp. 9700-9708, Oct 1992.

[14] Bin Shen and Fanghong Sun, "Molecular dynamics investigation on the atomic-scale friction behaviors between copper (001) and diamond (111) surfaces," *Applied Surface Science*, vol. 255, pp. 7663-7668, 2009.

[15] U. Landman et al., "Frictional Forces and Amontons' Law: From the Molecular to the Macroscopic Scale," *Journal of Physical Chemistry B*, vol. 108, no. 11, pp. 3410-3425, 2004.

[16] Keiji Hayashi et al., "Velocity-dependent threshold behavior of wearless nano-friction," *Computational Materials Science*, vol. 44, pp. 152-155, 2008.

[17] B. Li, P. C Clapp, J. A. Rifkin, and X. M. Zhang, "Molecular dynamics calculation of heat dissipation during sliding friction," *International Journal of Heat and Mass Transfer*, vol. 46, pp. 37-43, 2003.

[18] Y. R. Jeng, P. C. Tsai, and T. H. Fang, "Molecular dynamics studies of atomic-scale tribological characteristics for different sliding systems," *Tribology Letters*, vol. 18, no. 3, pp. 315-330, March 2005.

[19] S. Karthikeyan, A. Agrawal, and D. A. Rigney, "Molecular dynamics simulations of sliding in an Fe-Cu tribopair system," *Wear*, vol. 267, pp. 1166-1176, 2009.

[20] En-Quang Lin, Li-Sha Niu, Hui-Ji Shi, and Zheng Duan, "Molecular dynamics simulation of nano-scale interfacial friction characteristic for different tribopair systems," *Applied Surface Science*, vol. 258, pp. 2022-2028, 2012.

[21] Min Kyu Yeo and Yong Hoon Jang, "Molecular dynamics simulation of a nanoscale sliding layer system," *Wear*, vol. 269, pp. 206-212, 2010.

[22] Peter Spijker, Guillaume Anciaux, and Jean-Francois Molinari, "Relations between roughness, temperature and dry sliding friction at the atomic scale," *Tribology International*, vol. 59, pp. 222-229, 2013.

[23] G. Anciaux and J. F. Molinari, "Sliding of rough surfaces and energy dissipation with a 3D multiscale approach," *International Journal for Numerical Methods in Engineering*, vol. 83, pp. 1255-1271, February 2010.

[24] Yeau-Ren Jeng and Shin-Rung Peng, "Investigation into the lateral junction growth of single asperity contact using static atomistic simulations," *Applied Physics Letters*, vol. 94, no. 16, pp. 163103:1-3, 2009.

[25] R. Komanduri, N. Chandrasekaran, and L. M. Raff, "Molecular dynamics simulation of atomic-scale friction," *Physical Review B*, vol. 61, no. 20, May 2000.

[26] J. Yang and K. Komvopoulos, "A Molecular Dynamics Analysis of Surface Interference and Tip Shape and Size Effects on Atomic-Scale Friction," *Journal of Tribology*, vol. 127, pp. 513-521, July 2005.

[27] Pil-Pyung Cha, David J. Srolovitz, and T. Kyle Vanderlick, "Molecular dynamics

simulation of single asperity contact," *Acta Materialia*, vol. 52, pp. 3983-3996, 2004.

[28] Liangchi Zhang and Hiroaki Tanaka, "Towards a deeper understanding of wear and friction on the atomic scale - a molecular dynamics analysis," *Wear*, vol. 211, pp. 44-53, Oct. 1997.

[29] Liangchi Zhang and Hiroaki Tanaka, "Atomic scale deformation in silicon monocrystals induced by two-body and three-body contact sliding," *Tribology International*, vol. 31, no. 8, pp. 425-433, 1998.

[30] M. R. Sorensen, K. W. Jacobsen, and P. Stoltze, "Simulations of atomic-scale sliding friction," *Physical Review B*, vol. 53, no. 4, pp. 2101-2113, January 1996.

[31] J. Song and D. J. Srolovitz, "Adhesion effects in material transfer in mechanical contacts," *Acta Materialia*, vol. 54, pp. 5305-5312, Nov. 2006.

[32] Jun Song and David J. Srolovitz, "Atomistic simulation of multicycle asperity contact," *Acta Materialia*, vol. 55, pp. 4759-4768, Aug. 2007.

[33] Roger Smith et al., "Stick slip and wear on metal surfaces," *Wear*, vol. 259, pp. 459-466, 2005.

[34] Eui-Sung Yoon, R. A. Singh, Hyun-Jin Oh, and Hosung Kong, "The effect of contact area on nano/micro-scale friction," *Wear*, vol. 259, pp. 1424-1431, Aug. 2005.

[35] Eui-Sung Yoon, Seung H. Yang, Hung-Gu Han, and Hosung Kong, "An experimental study on the adhesion at a nano-contact," *Wear*, vol. 254, pp. 974-980, July 2003.

[36] R. Komanduri, N. Chandrasekaran, and L. M. Raff, "MD simulation of indentation and scratching of single crystal aluminum," *Wear*, vol. 240, pp. 113-143, May 2000.

[37] K. Cheng, X. Luo, R. Ward, and R. Holt, "Modeling and simulation of the tool wear in nanometric cutting," *Wear*, vol. 255, pp. 1427-1432, 2003.

[38] B. Lin, S. Y. Yu, and S. X. Wang, "An experimental study on molecular dynamics simulation in nanometer grinding," *Journal of Materials Processing Technology*, vol.

138, pp. 484-488, 2003.

[39] K. Maekawa and A. Itoh, "Friction and tool wear in nano-scale machining - a molecular dynamics approach," *Wear*, vol. 188, pp. 115-122, 1995.

[40] Tadatoshi Nozaki, Masao Doyama, Yoshiaki Kogure, and Tatsuo Yokotsuka, "Micromachining of pure silicon by molecular dynamics," *Thin Solid Films*, vol. 334, pp. 221-224, 1998.

[41] J. Shimizu, L. B. Zhou, and H. Eda, "Simulation and experimental analysis of super high-speed grinding of ductile material," *Journal of Materials Processing Technology*, vol. 129, pp. 19-24, 2002.

[42] In-Ha Sung and Dae-Eun Kim, "Study on nanoscale abrasive interaction between nanoprobe and self-assembled molecular surface for probe-based nanolithography process," *Ultramicroscopy*, vol. 107, pp. 1-7, Jan. 2007.

[43] Y. D. Yan, T. Sun, S. Dong, X. C. Luo, and Y. C. Liang, "Molecular dynamics simulation of processing using AFM pin tool," *Applied Surface Science*, vol. 252, pp. 7523-7531, Aug. 2006.

[44] Ping Yang and Huazhong Zhang, "Numerical analysis on meshing friction characteristics of nano-gear train," *Tribology International*, vol. 41, pp. 535-541, June 2008.

[45] Sergio B. Legoas, Ronaldo Giro, and Douglas S. Galvao, "Molecular dynamics simulations of C60 nanobearings," *Chemical Physics Letters*, vol. 386, pp. 425-429, Mar. 2004.

[46] Farid F. Abraham, William E. Rudge, and Pantelis S. Alexopoulos, "Fragmentation dynamics in asperity collisions: A molecular dynamics simulation study," *Computational Materials Science*, vol. 3, pp. 21-40, Sep. 1994.

[47] T. W. Stone, M. F. Horstemeyer, Y. Hammi, and P. M. Gullett, "Contact and

friction of single crystal nickel nanoparticles using molecular dynamics," *Acta Materialia*, vol. 56, pp. 3577-3584, August 2008.

[48] Binquan Luan and Mark O. Robbins, "Contact of single asperities with varying adhesion: Comparing continuum mechanics to atomistic simulations," *Physical Review E*, vol. 74, pp. 026111:1-17, 2006.

[49] A. Faulkner and R. D. Arnell, "The development of a finite element model to simulate the sliding interaction between two, three-dimensional, elastoplastic, hemispherical asperities," *Wear*, vol. 242, pp. 114-122, 2000.

[50] Jeremy J. Dawkins and Richard W. Neu, "Influence of Crystallographic Orientation on Energy Dissipation During Sliding," *Journal of Tribology*, vol. 130, pp. 041604:1-9, October 2008.

[51] R. L. Jackson, R. S. Duvvuru, H. Meghani, and M. Mahajan, "An analysis of elasto-plastic sliding spherical asperity interaction," *Wear*, vol. 262, pp. 210-219, January 2007.

[52] V. Boucly, D. Nelias, and I. Green, "Modeling of the Rolling and Sliding Contact Between Two Asperities," *Journal of Tribology*, vol. 129, pp. 235-245, April 2007.

[53] Satish Achanta, Dirk Drees, and Jean-Pierre Celis, "Friction from nano to macroforce scales analyzed by single and multiple-asperity contact approaches," *Surface & Coatings Technology*, vol. 202, pp. 6127-6135, 2008.

[54] Uzi Landman et al., "Fricitional Forces and Amontons' Law: From the Molecular to the Macroscopic Scale," vol. 108, no. 11, 2004.

[55] Michael Rieth, *Nano-Engineering in Science and Technology: An Introduction to the World of Nano-Design.*: World Scientific Publication, 2003, vol. 6.

[56] Tamar Schlick, *Molecular Modeling and Simulation: An Interdisciplinary Guide.* New York: Springer, 2006.

[57] J. M. Haile, *Molecular Dynamics Simulation: Elementary Methods.*: Wiley & Sons, Inc, 1997.

[58] Daan Frenkel and Berend Smit, *Understanding Molecular Simulation.*: Academic Press, 2002.

[59] Steve Plimpton, "Fast Parallel Algorithms for Short Range Molecular Dynamics," *Journal of Computational Physics*, vol. 117, pp. 1-19, 1995.

[60] M. P. Allen and D. J. Tildesley, *Computer Simulation of Liquids.*: Oxford University Press, 2007.

[61] Loup Verlet, "Computer "Experiments" on Classical Fluids. I. Thermodynamical Properties of Lennard-Jones Molecules," *Physical Review*, vol. 159, no. 1, pp. 98-103, July 1967.

[62] V. G. Baidakov, S. P. Protsenko, and Z. R. Kozlova, "Thermal and caloric equations of state fro stable and metastable Lennard-Jones fluids: I. Molecular-dynamics simulations," *Fluid Phase Equilibria*, vol. 263, pp. 55-63, 2008.

[63] Jiri Kolafa and Ivo Nezbeda, "The Lennard-Jones fluid: An accurate analytic and theoretically-based equation of state," vol. 100, pp. 1-34, 1994.

[64] A. Hisham Abdel-Aal, "Thermal compatibility of dry sliding tribo-specimens," *Wear*, vol. 251, pp. 939-948, 2001.

[65] J. H. Li et al., "Interatomic potentials of the binary transition metal systems and some applications in materials physics," *Physics Reports*, vol. 455, pp. 1-134, 2008.

[66] Murray S. Daw and Michael I. Baskes, "Embedded-atom method: Derivation and application to impurities, surfaces and other defects in metals," *Physical Review B*, vol. 29, no. 12, pp. 6443-6453, June 1984.

[67] Murray S. Daw, Stephen M. Foiles, and Michael I. Baskes, "The embedded-atom method: a review of theory and applications," *Materials Science Reports*, vol. 9, pp.

251-310, 1993.

[68] S. M. Foiles, M. I. Baskes, and M. S. Daw, "Embedded-atom-method function for the fcc metals Cu, Ag, Au, Ni, Pd, Pt, and their alloys," *Physical Review B*, vol. 33, no. 12, pp. 7983-7991, June 1986.

[69] Steven J. Plimpton and Bruce A. Hendrickson, "Parallel Molecular Dynamics with the Embedded Atom Method," in *Materials Theory and Modelling*, Pittsburgh, PA, 1993, p. 37.

[70] D. C. Rapaport, *The Art of Molecular Dynamics Simulation*, 2nd ed.: Cambridge University Press, 2007.

[71] Alexey K. Mazur, "Common Molecular Dynamics Algorithms Revisited: Accuracy and Optimal Time Steps of Stomer-Leapfrog Integrators," *Journal of Computational Physics*, vol. 136, pp. 354-365, April 1997.

[72] Marcos A. Villarreal, Oscar A. Oviedo, and Ezequiel P.M. Leiva, "A Straightforward Approach for the Determination of the Maximum Time Step for the Simulation of Nanometric Metallic Systems," *Journal of Chemical Theory and Computation*, vol. 8, pp. 1744-1749, March 2012.

[73] R. L. Jackson, "The Effect of Scale-Dependent Hardness on Elasto-Plastic Asperity Contact between Rough Surfaces," *Tribology Transactions*, vol. 49, no. 2, pp. 135-150, 2006.

[74] P. J. Blau, "Scale Effects in Steady-State Friction," *Tribology Transactions*, vol. 34, no. 3, pp. 335-342, 1991.

[75] J. Zhong, J. B. Adams, and L. G. Hector, "Molecular dynamics simulations of asperity shear in aluminum," *Journal of Applied Physics*, vol. 94, no. 7, pp. 4306-4314, October 2003.

[76] H. Eid et al., "A Combined Molecular Dynamics and Finite Element Analysis of

Contact and Adhesion of a Rough Sphere and a Flat Surface," *Tribology Transactions*, vol. 54, pp. 920-928, 2011.

[77] J. Barriga, B. Fernandez-Diaz, A. Juarros, S. I.-U. Ahmed, and J. L. Arana, "Microtribological analysis of gold and copper contacts," *Tribology Internation*, vol. 40, pp. 1526-1530, 2007.

[78] G. Liu et al., "Investigation of the mending effect and mechanicsm of copper nanoparticles on a tribologically stressed surface," *Tribology Letters*, vol. 17, no. 4, pp. 961-966, November 2004.

[79] Hao Luo, Xu Zhu, Hasnain Lakdawala, L. Richard Carley, and Gary K. Fedder, "A copper CMOS-MEMS Z-axis gyroscope," in *Micro Electro Mechanical Systems*, Las Vegas, 2002, pp. 631-634.

[80] T. C. Hu, Y. T. Wang, F. C. Hsu, P. K. Sun, and M. T. Lin, "Cyclic creep and fatigue testing of nanocrystalline copper thin films," *Surface and Coatings Technology*, vol. 215, pp. 393-399, January 2013.

[81] Olivier Perroud, Renaud Vayrette, Christian Rivero, Olivier Thomas, and Jean-Sebastien Micha, "X-ray microbeam strain investigation on Cu-MEMS structures," *Microelectronic Engineering*, vol. 87, pp. 394-397, 2010.

[82] Hsiang-Chen Hsu, Jih-Hsin Chien, and Shen-Li Fu, "A study on nano-mechanical properties and nano-tribology for ultra-thin Pt coated 4N copper wire," in *International Microsystems, Packaging, Assembly and Circuits Technology Conference*, pp. 488-491.

[83] W. Osterle, C. Prietzel, H. Kloss, and A. I. Dmitriev, "On the role of copper in brake friction materials," *Tribology International*, vol. 43, pp. 2317-2326, 2010.

[84] S. Tarasov, A. Kolubaev, S. Belyaev, M. Lerner, and F. Tepper, "Study of friction reduction by nanocopper additives to motor oil," *Wear*, vol. 252, pp. 63-69, 2002.

[85] Y. Choi et al., "Tribological behavior of copper nanoparticles as additives in oil," *Current Applied Physics*, vol. 9, pp. e124-e127, 2009.

[86] L. C. Zhang, K. L. Johnson, and W. C. D. Cheong, "A molecular dynamics study of scale effects on the friction of single-asperity contacts," *Tribology Letters*, vol. 10, no. 1-2, pp. 23-28, 2001.

[87] P. Zhu, Y. Hu, T. Ma, and H. Wang, "Molecular Dynamics Study on Friction Due to Ploughing and Adhesion in nanometric Scratching Process," *Tribology Letters*, vol. 41, pp. 41-46, 2011.

[88] Q. X. Pei, C. Lu, and H. P. Lee, "Large scale molecular dynamics study of nanometric machining of copper," *Computational Materials Science*, vol. 41, pp. 177-185, 2007.

[89] Bharat Bhushan, "Nanotribology and nanomechanics of MEMS/NEMS and BioMEMS/BioNEMS materials and devices," *Microelectronic Engineering*, vol. 84, pp. 387-412, 2007.

[90] J. Lin, T. Fang, C. Wu, and K. Houng, "Contact and frictional behavior of rough surfaces using molecular dynamics combined with fractal theory," *Computational Materials Science*, vol. 40, pp. 480-484, October 2007.

[91] H. M. Pen et al., "Multiscale simulation of nanometric cutting of single crystal copper and its experimental validation," *Computational Materials Science*, vol. 50, pp. 3431-3441, 2011.

[92] Kun Sun, Liang Fang, Zhiyang Yan, and Jiapeng Sun, "Atomistic scale tribological behaviors in nano grained and single crystal copper systems," *Wear*, vol. 303, pp. 191-201, 2013.

[93] Maneesh Mishra, Philip Egberts, Roland Bennewitz, and Izabela Szlufarska, "Friction model for single asperity elastic-plastic contacts," *Physical Review B*, vol.

86, pp. 1-9, July 2012.

[94] Buckley, D. H.; Lewis Research Center, Ohio, "Effect of Recrystallization on Friction Properties of Some Metals in Single-Crystal and Polycrystalline Form," National Aeronautics and Space Administration, Technical Note 1967.

[95] S. Ray and S. K. Roy Chowdhury, "An Analysis of Surface Temperature Rise at the Contact between Sliding Bodies with Small-Scale Surface Roughness," *Tribology Transactions*, vol. 53, pp. 491-501, 2010.

[96] S. P. Yuan and P. X. Jiang, "Thermal Conductivity of Small Nickel Particles," *International Journal of Thermophysics*, vol. 27, no. 2, pp. 581-595, March 2006.

[97] Bo Feng, Zhixin Li, and Xing Zhang, "Role of phonon in the thermal and electrical transport in metallic nanofilms," *Journal of Applied Physics*, vol. 105, pp. 1-7, May 2009.

[98] Till Junge and Jean-Francois Molinari, "Molecular dynamics nano-scratching of aluminum: a novel quantitative energy-based analysis method," *Procedia IUTAM*, vol. 3, pp. 192-204, Mar. 2012.

[99] A. A. Dadali, I. P. Lastenko, V. D. Blank, and V. A. Danilov, "Energetics of Plastic Flow under High Pressure and Shear Deformation," *Journal of Solid State Chemistry*, vol. 98, pp. 337-342, 1992.

[100] Robert L. Jackson and Itzhak Green, "A statistical model of elasto-plastic asperity contact between rough surfaces," *Tribology International*, vol. 39, pp. 906-914, 2006.

[101] W. R. Chang, I. Etsion, and D. B. Bogy, "Static Friction Coefficient Model for Metallic Rough Surfaces," *Journal of Tribology*, vol. 110, pp. 57-63, January 1988.

Appendix

LAMMPS uses an input script (as one of the methods) to run a simulation. The input script is in the form of a text file, which consists of a list of commands that are executed in a sequential order. Each line begins with a command followed by the corresponding arguments. The comment lines begin with a '#' sign and are ignored by LAMMPS during execution. At the end of the input script, the simulation is terminated [59]. A sample of the input script used to run all the simulations performed in this work is given below. The command arguments for certain commands are different for every case considered in this work. These commands are marked with '*' (not part of the actual input script) and the command arguments corresponding to every case simulated are listed for those particular commands. Detailed information on the commands and their arguments can be found in the LAMMPS manual.

Input Script

```
# 3D Friction Simulation of Sliding Cu-Cu Asperities

units           metal
dimension       3
boundary        p s p

atom_style      atomic
neighbor        2.0 bin
neigh_modify    delay 5

# Create geometry

lattice*        fcc 3.615
region*         box block -150 450 0 152.5 -75 75 units box
create_box      3 box
mass            * 63.546

# Regions

region*         lo-fixed block 75 225 0 5 -75 75 units box
region*         above-lo block INF INF INF 5 INF INF side out units box
region*         hi-fixed block -150 0 147.5 152.5 -75 75 units box
region*         below-hi block INF INF 147.5 INF INF INF side out units box
region*         slab1 block 75 225 5 20 -75 75 units box
region*         slab2 block 75 225 20 35 -75 75 units box
region*         slab3 block 75 225 35 50 -75 75 units box
region*         slab4 block 75 225 50 65 -75 75 units box
region*         slab5 block 75 225 65 80 -75 75 units box
region*         slab6 block -150 0 72.5 87.5 -75 75 units box
region*         slab7 block -150 0 87.5 102.5 -75 75 units box
region*         slab8 block -150 0 102.5 117.5 -75 75 units box
region*         slab9 block -150 0 117.5 132.5 -75 75 units box
region*         slab10 block -150 0 132.5 147.5 -75 75 units box
region*         lo-asperity sphere 150 5 0 75 units box
region*         hi-asperity sphere -75 147.5 0 75 units box
region          lo-half-sphere intersect 2 lo-asperity above-lo
```

```
region          hi-half-sphere intersect 2 hi-asperity below-hi
region          sensor1 intersect 2 lo-half-sphere slab1
region          sensor2 intersect 2 lo-half-sphere slab2
region          sensor3 intersect 2 lo-half-sphere slab3
region          sensor4 intersect 2 lo-half-sphere slab4
region          sensor5 intersect 2 lo-half-sphere slab5
region          sensor6 intersect 2 hi-half-sphere slab6
region          sensor7 intersect 2 hi-half-sphere slab7
region          sensor8 intersect 2 hi-half-sphere slab8
region          sensor9 intersect 2 hi-half-sphere slab9
region          sensor10 intersect 2 hi-half-sphere slab10

# Create atoms

create_atoms    1 region lo-half-sphere
create_atoms    2 region hi-half-sphere
create_atoms    3 region lo-fixed
create_atoms    3 region hi-fixed

# Potentials

pair_style      eam
pair_coeff      * * Cu_u3.eam

# Groups

group           lo-fixed region lo-fixed
group           hi-fixed region hi-fixed
group           lo-half-sphere region lo-half-sphere
group           hi-half-sphere region hi-half-sphere
group           sensor1 region sensor1
group           sensor2 region sensor2
group           sensor3 region sensor3
group           sensor4 region sensor4
group           sensor5 region sensor5
group           sensor6 region sensor6
group           sensor7 region sensor7
group           sensor8 region sensor8
```

```
group           sensor9 region sensor9
group           sensor10 region sensor10
group           boundary union lo-fixed hi-fixed
group           mobile subtract all boundary
group           driven union mobile lo-fixed

# Initial velocities

compute         asp mobile temp/partial 0 1 1
velocity*       mobile create 600 482748 temp asp
compute         1 sensor1 temp
compute         2 sensor2 temp
compute         3 sensor3 temp
compute         4 sensor4 temp
compute         5 sensor5 temp
compute         6 sensor6 temp/partial 0 1 1
compute         7 sensor7 temp/partial 0 1 1
compute         8 sensor8 temp/partial 0 1 1
compute         9 sensor9 temp/partial 0 1 1
compute         10 sensor10 temp/partial 0 1 1
compute         lo_asp lo-half-sphere temp
compute         hi_asp hi-half-sphere temp/partial 0 1 1

# Fixes

fix             1 driven nve
fix             2 lo-fixed setforce 0.0 0.0 0.0
fix             3 hi-fixed setforce 0.0 0.0 0.0
#fix            4 sensor1 temp/rescale 100 300 300 0.1 1
#fix            5 sensor10 temp/rescale 100 300 300 0.1 1
#fix_modify     5 temp 10

# Run

timestep*       0.002
thermo          100
```

thermo_style	custom step temp c_lo_asp c_1 c_2 c_3 c_4 c_5 c_6 c_7 c_8 c_9 c_10 c_hi_asp pe ke etotal vol f_2[1] f_2[2] f_2[3] f_3[1] f_3[2] f_3[3]
thermo_modify	format 1 %07d format 2 %7.3f format 3 %7.3f format 4 %7.3f format 5 %7.3f format 6 %7.3f format 7 %7.3f format 8 %7.3f format 9 %7.3f format 10 %7.3f format 11 %7.3f format 12 %7.3f format 13 %7.3f format 14 %7.3f format 15 %10.3f format 16 %10.3f format 17 %10.3f format 18 %10.3f format 19 %011.6f format 20 %011.6f format 21 %011.6f format 22 %011.6f format 23 %011.6f format 24 %011.6f
run	5000
variable*	VXequal(exp(step/30000)-exp(-step/30000))/(exp(step/30000)+exp(-step/30000))
fix*	4 hi-fixed move variable NULL NULL NULL v_VX NULL NULL
#fix*	4 hi-fixed move linear 0.1 0.0 0.0 units box
dump	1 all atom 3000 dump.cu75dR10
dump	2 all dcd 1000 dcd.cu75dR10
dump	3 hi-fixed custom 3000 vel75dR10.txt id vx vy vz
run*	246000

Normalized Interference Multiplier

δ/R	m
0.10	0
0.08	0.02
0.06	0.04
0.04	0.06
0.02	0.08
0.00	0.10
-0.04	0.14

Asperity Size, R (for $v = 10$ m/ s)

$R = 50 \;\; A$	region	box block 0 250 0 105 -50 50 units box
	region	lo-fixed block 50 150 0 5 -50 50 units box
	region	above-lo block INF INF INF 5 INF INF side out units box
	region	hi-fixed block 0 100 100+mR 105+mR -50 50 units box
	region	below-hi block INF INF 100+mR INF INF INF side out units box
	region	slab1 block 50 150 5 15 -50 50 units box
	region	slab2 block 50 150 15 25 -50 50 units box
	region	slab3 block 50 150 25 35 -50 50 units box
	region	slab4 block 50 150 35 45 -50 50 units box
	region	slab5 block 50 150 45 55 -50 50 units box
	region	slab6 block 0 100 50+mR 60+mR -50 50 units box
	region	slab7 block 0 100 60+mR 70+mR -50 50 units box
	region	slab8 block 0 100 70+mR 80+mR -50 50 units box
	region	slab9 block 0 100 80+mR 90+mR -50 50 units box
	region	slab10 block 0 100 90+mR 100+mR -50 50 units box
	region	lo-asperity sphere 100 5 0 50 units box
	region	hi-asperity sphere 50 100+mR 0 50 units box
	fix	4 hi-fixed move linear 0.1 0.0 0.0 units box
	run	1250000
$R = 75 \;\; A$	region	box block -150 450 0 152.5 -75 75 units box
	region	lo-fixed block 75 225 0 5 -75 75 units box
	region	above-lo block INF INF INF 5 INF INF side out units box
	region	hi-fixed block -150 0 147.5+mR 152.5+mR -75 75 units box
	region	below-hi block INF INF 147.5+mR INF INF INF side out units box
	region	slab1 block 75 225 5 20 -75 75 units box
	region	slab2 block 75 225 20 35 -75 75 units box
	region	slab3 block 75 225 35 50 -75 75 units box
	region	slab4 block 75 225 50 65 -75 75 units box
	region	slab5 block 75 225 65 80 -75 75 units box
	region	slab6 block -150 0 72.5+mR 87.5+mR -75 75 units box

	region	slab7 block -150 0 87.5+mR 102.5+mR -75 75 units box
	region	slab8 block -150 0 102.5+mR 117.5+mR -75 75 units box
	region	slab9 block -150 0 117.5+mR 132.5+mR -75 75 units box
	region	slab10 block -150 0 132.5+mR 147.5+mR -75 75 units box
	region	lo-asperity sphere 150 5 0 75 units box
	region	hi-asperity sphere -75 147.5+mR 0 75 units box
	fix	4 hi-fixed move linear 0.1 0.0 0.0 units box
	run	1875000
$R = 100$ A	region	box block 0 500 0 200 -100 100 units box
	region	lo-fixed block 100 300 0 5 -100 100 units box
	region	above-lo block INF INF INF 5 INF INF side out units box
	region	hi-fixed block 0 200 195+mR 200+mR -100 100 units box
	region	below-hi block INF INF 195+mR INF INF INF side out units box
	region	slab1 block 100 300 5 25 -100 100 units box
	region	slab2 block 100 300 25 45 -100 100 units box
	region	slab3 block 100 300 45 65 -100 100 units box
	region	slab4 block 100 300 65 85 -100 100 units box
	region	slab5 block 100 300 85 105 -100 100 units box
	region	slab6 block 0 200 95+mR 115+mR -100 100 units box
	region	slab7 block 0 200 115+mR 135+mR -100 100 units box
	region	slab8 block 0 200 135+mR 155+mR -100 100 units box
	region	slab9 block 0 200 155+mR 175+mR -100 100 units box
	region	slab10 block 0 200 175+mR 195+mR -100 100 units box
	region	lo-asperity sphere 200 5 0 100 units box
	region	hi-asperity sphere 100 195+mR 0 100 units box
	fix	4 hi-fixed move linear 0.1 0.0 0.0 units box
	run	3000000

Asperity Size, R (for $v = 100$ m/ s)

$R = 50$ A	region	box block -240 300 0 105 -50 50 units box
	region	lo-fixed block 70 170 0 5 -50 50 units box
	region	above-lo block INF INF INF 5 INF INF side out units box
	region	hi-fixed block -230 -130 100+mR 105+mR -50 50 units box
	region	below-hi block INF INF 100+mR INF INF INF side out units box
	region	slab1 block 70 170 5 15 -50 50 units box
	region	slab2 block 70 170 15 25 -50 50 units box
	region	slab3 block 70 170 25 35 -50 50 units box
	region	slab4 block 70 170 35 45 -50 50 units box
	region	slab5 block 70 170 45 55 -50 50 units box
	region	slab6 block -230 -130 50+mR 60+mR -50 50 units box
	region	slab7 block -230 -130 60+mR 70+mR -50 50 units box
	region	slab8 block -230 -130 70+mR 80+mR -50 50 units box
	region	slab9 block -230 -130 80+mR 90+mR -50 50 units box
	region	slab10 block -230 -130 90+mR 100+mR -50 50 units box
	region	lo-asperity sphere 120 5 0 50 units box
	region	hi-asperity sphere -180 100+mR 0 50 units box
	variable	VX equal (exp(step/45000)-exp(-step/45000))/(exp(step/45000)+exp(-step/45000))
	fix	4 hi-fixed move variable NULL NULL NULL v_VX NULL NULL
	run	242000
$R = 75$ A	region	box block -150 450 0 152.5 -75 75 units box
	region	lo-fixed block 75 225 0 5 -75 75 units box
	region	above-lo block INF INF INF 5 INF INF side out units box
	region	hi-fixed block -150 0 147.5+mR 152.5+mR -75 75 units box
	region	below-hi block INF INF 147.5+mR INF INF INF side out units box
	region	slab1 block 75 225 5 20 -75 75 units box
	region	slab2 block 75 225 20 35 -75 75 units box
	region	slab3 block 75 225 35 50 -75 75 units box
	region	slab4 block 75 225 50 65 -75 75 units box

	region	slab5 block 75 225 65 80 -75 75 units box
	region	slab6 block -150 0 72.5+mR 87.5+mR -75 75 units box
	region	slab7 block -150 0 87.5+mR 102.5+mR -75 75 units box
	region	slab8 block -150 0 102.5+mR 117.5+mR -75 75 units box
	region	slab9 block -150 0 117.5+mR 132.5+mR -75 75 units box
	region	slab10 block -150 0 132.5+mR 147.5+mR -75 75 units box
	region	lo-asperity sphere 150 5 0 75 units box
	region	hi-asperity sphere -75 147.5+mR 0 75 units box
	variable	VX equal (exp(step/30000)-exp(-step/30000))/(exp(step/30000)+exp(-step/30000))
	fix	4 hi-fixed move variable NULL NULL NULL v_VX NULL NULL
	run	246000
$R = 100 \;\; A$	region	box block -200 600 0 200 -100 100 units box
	region	lo-fixed block 100 300 0 5 -100 100 units box
	region	above-lo block INF INF INF 5 INF INF side out units box
	region	hi-fixed block -200 0 195+mR 200+mR -100 100 units box
	region	below-hi block INF INF 195+mR INF INF INF side out units box
	region	slab1 block 100 300 5 25 -100 100 units box
	region	slab2 block 100 300 25 45 -100 100 units box
	region	slab3 block 100 300 45 65 -100 100 units box
	region	slab4 block 100 300 65 85 -100 100 units box
	region	slab5 block 100 300 85 105 -100 100 units box
	region	slab6 block -200 0 95+mR 115+mR -100 100 units box
	region	slab7 block -200 0 115+mR 135+mR -100 100 units box
	region	slab8 block -200 0 135+mR 155+mR -100 100 units box
	region	slab9 block -200 0 155+mR 175+mR -100 100 units box
	region	slab10 block -200 0 175+mR 195+mR -100 100 units box
	region	lo-asperity sphere 200 5 0 100 units box
	region	hi-asperity sphere -100 195+mR 0 100 units box
	variable	VX equal (exp(step/30000)-exp(-step/30000))/(exp(step/30000)+exp(-step/30000))
	fix	4 hi-fixed move variable NULL NULL NULL v_VX NULL NULL

	run	320000

Lattice Orientation, $\boldsymbol{\theta}$

$\theta = 0°$	lattice	fcc 3.615
$\theta = 14°$	lattice	fcc 3.615 orient x 1 4 0 orient y -4 1 0
$\theta = 18°$	lattice	fcc 3.615 orient x 1 3 0 orient y -3 1 0
$\theta = 27°$	lattice	fcc 3.615 orient x 1 2 0 orient y -2 1 0
$\theta = 34°$	lattice	fcc 3.615 orient x 2 3 0 orient y -3 2 0
$\theta = 45°$	lattice	fcc 3.615 orient x 1 1 0 orient y -1 1 0

Time-step, $\boldsymbol{\Delta t}$

$\Delta t = 0.002\ ps$	timestep	0.002
$\Delta t = 0.005\ ps$	timestep	0.005

Thermostat, 300 $\boldsymbol{K}$

Off	#fix	4 sensor1 temp/rescale 100 300 300 0.1 1
	#fix	5 sensor10 temp/rescale 100 300 300 0.1 1
	#fix_modify	5 temp 10
	run (1)	5000
	run (2)	1875000
On	fix	4 sensor1 temp/rescale 100 300 300 0.1 1
	fix	5 sensor10 temp/rescale 100 300 300 0.1 1
	fix_modify	5 temp 10
	run (1)	10000
	run (2)	1875000